RUPRECHT-KARLS-UNIVERSITÄT HEIDELBERG

Dominik Enders

Surface Enhanced Infrared Absorption on Au Nanoparticle Films for Optical Biosensing

Dissertation

HD-KIP-05-59

KIRCHHOFF-INSTITUT FÜR PHYSIK

Dissertation
submitted to the
Combined Faculties for Natural Sciences and for Mathematics
of the Ruperto-Carola University of Heidelberg, Germany
for the degree of

Doctor of Natural Sciences

presented by

Diplom-Physiker Dominik Enders

born in Baden-Baden

Oral examination: December 14$^{\text{th}}$ 2005

Surface Enhanced Infrared Absorption on Au Nanoparticle Films for Optical Biosensing

Referees: Prof. Dr. Annemarie Pucci
Prof. Dr. Reinhard Neumann

Oberflächenverstärkte Infrarotabsorption auf Au-Nanopartikelfilmen für die optische Biosensorik:

Schwerpunkt dieser Arbeit ist die Untersuchung der oberflächenverstärkten Infrarotabsorption (SEIRA) von Adsorbaten auf naßchemisch hergestellten Au-Nanopartikel(AuNP)filmen. Die optischen Eigenschaften von AuNP-Filmen wurden mit VIS-Spektroskopie untersucht; es wurde gezeigt, daß sich diese Eigenschaften durch Effektiv-Medien-Theorien beschreiben lassen. Die SEIRA-Aktivität wurde mit FTIR-Spektroskopie von Adsorbaten auf AuNP-Filmen untersucht. Ein Vergleich der Spektren mit denen vom gleichen Adsorbat auf einem glatten SEIRA-inaktiven Au-Film ergab SEIRA-Faktoren von 26 im Falle von einzelnen kugelförmigen AuNP, bis hin zu drei Größenordnungen im Falle von gewachsenen AuNP-Filmen. Die Morphologie der AuNP-Filme wurde mit Rasterkraftmikroskopie und Rasterelektronenmikroskopie untersucht. Ferner wurden SEIRA-aktive AuNP-Filme als optische Sensoren für die Ex-situ-Messung von spezifischer Antikörper/Antigen-Kopplung sowie für die In-situ-Messung von Adsorbaten (Octadecanthiol, DNA) während des Adsorptionsprozesses eingesetzt.

Surface Enhanced Infrared Absorption on Au Nanoparticle Films for Optical Biosensing:

This work is focussed on the investigation of surface enhanced infrared absorption (SEIRA) of adsorbates on wet chemically prepared Au nanoparticle (AuNP) films. Optical properties of AuNP films were investigated with VIS spectroscopy; it was shown, that it is possible to describe these properties with effective media theories. The SEIRA activity was analysed by FTIR spectroscopy of adsorbates on AuNP films and comparison of the spectra with other FTIR spectra of the same adsorbate on a smooth SEIRA inactive Au film. A SEIRA factor of 26 was found for a film of discrete spherical AuNP, while in case of grown AuNP films a SEIRA enhancement of up to three orders of magnitude was achieved. The AuNP film morphology was characterized with scanning force microscopy and scanning electron microscopy. SEIRA active AuNP films were used as optical sensors for the ex-situ measurement of specific antibody-antigen coupling and the in-situ measurement of adsorbates (octadecanethiol, DNA) during the adsorption process.

Contents

1. Introduction

The effect of surface enhanced infrared absorption (SEIRA) was discovered in 1980 by Hartstein and coworkers [1]. They observed, that the infrared absorption of molecules can be enhanced by up to three orders of magnitude, if the molecules are adsorbed on thin Au or Ag surfaces; this effect is the analogon of surface enhanced Raman scattering (SERS) [2]. The strength of enhancement depends on adsorbate, substrate, metal type, and, because of the relation to the excitation spectrum of surface plasmon polaritons in the IR range, strongly on the metal film morphology and therefore on the preparation method [3, 4, 5]. Strong SEIRA enhancement is obtained, if the metal film consists of densely packed, but yet separate islands [6, 7, 8]. The origin of SEIRA are—similar to SERS—chemical effects and electromagnetic effects, as shown in theoretical [9, 10] and experimental [11, 12, 13] works. The origin of the electromagnetic effect are morphology-induced local enhancements of the electromagnetic field; this mainly occurs in the space between narrow metal islands, where the electromagnetic field may be enhanced by several orders of magnitude [3, 14], and can be described on the base of effective media theories [10, 15]. The chemical effect is known to be effective for adsorbate molecules of the first layer (first layer effect) [6]. This effect consists of a static charge transfer [16], as well as a dynamic interaction between adsorbate vibrations and the electron-hole continuum of the substrate [17, 18]. However, the quantitative contribution of these mechanisms to the enhancement and to the usually occurring asymmetry of the absorption lines (Fano lines) remain non-comprehended [6, 19].

SEIRA has not only been observed in ATR (attenuated total reflection) geometry, as done by Hartstein [1] or in [20], but also in reflection [21] and transmission geometry [22, 23]. In the last years SEIRA has become an increasingly meaningful factor in biospectroscopy: In ex-situ IRRAS (infrared reflection absorption spectroscopy) geometry, the coupling of salmonella antigens to antibodies against salmonella, that had been immobilized onto a SEIRA active Au film, was investigated [24]. Ex-situ IRRAS was also used to measure SEIRA of DNA of cancerous rats (some of them were treated with cancer medication) immobilized on Au [25]. In the same work human RNA, extracted from brain tumors of different stage of progress, was investigated. Ataka and Heberle [26, 27] monitored the adsorption kinetics of the protein Cytochrome c on a

Au/liquid interface using ATR geometry. In this experiment the Au film worked as an electrode making it possible to impress a voltage on the solid/liquid interface and electrochemically induce oxidation and reduction processes of the protein.

However, a routinely application of SEIRA spectroscopy in biology and medicine is still foreclosed by too many uncertainties: the SEIRA active metal film must be stable when exposed to mechanical stress, the preparation method must be easy and reproducible. In the past, SEIRA films were mainly produced by physical vapor deposition onto dielectric substrates [3, 6, 7, 28, 29, 30, 31, 32, 33, 34, 35]. Au is known to be a metal with very high SEIRA activity and chemical stability; however, when preparing Au films on Si—a very convenient and commercially established substrate for IR spectroscopy—problems appear because of the very poor adhesive properties of Au on the natural SiO_2 layer. Au peels off from the SiO_2/Si even at very low mechanical impact. Therefore in thin-film technique, usually a very thin layer of Ti or Cr is used as an adhesive layer between the Au and the SiO_2. On the other hand, this layer causes the Au to grow more flat; this is an effect that is usually wanted in thin-film technique, but it decreases the SEIRA activity of the film [36]. To escape from this dilemma, recently the use of wet chemically prepared Au films has become more common in SEIRA spectroscopy [27, 37, 38, 39, 40]. However, it seems that—especially in the field of biospectroscopy—the SEIRA active wet chemically prepared metal films are used as a tool, while the quantitative extent of the enhancement is not in focus. Therefore in most works nothing is mentioned about the enhancement factor, that could be estimated by comparison with measurements of adsorbates on non-SEIRA active films. The exact influence of the wet chemical preparation on the SEIRA enhancement has not yet been investigated.

Several methods exist for wet chemical preparation of Au films. To get the desired SEIRA active morphology of densely packed but yet separate islands, a method of preparation was applied, consisting of a phase of Au nanoparticle (AuNP) deposition onto the substrate, and a growing phase, in which the size of the AuNP was strongly increased, and the distance between the particles became smaller. The methods of AuNP preparation, deposition on the Si substrate, and the growing of the deposited AuNP are well established in the literature, however this thesis is—to the knowledge of the author—the first work, that applies this preparation method for SEIRA spectroscopy, and that investigates the factor of the SEIRA enhancement.

The chapters of this thesis are arranged in the following way: In chapter 2, fundamentals like FTIR spectroscopy, Drude theory, effective medium theories and basics about SEIRA are shortly introduced. Also the preparation methods of AuNP films are shown, and the investigated adsorbate molecules are briefly discussed. Chapter 3 gives an overview about the used equipment. Because this thesis consists of work

that was done at the Kirchhoff Institute for Physics at the University of Heidelberg, and work that was done during a two month guest stay at the National Institute for Materials Science (NIMS) in Tsukuba, Japan, some instruments (e. g. FTIR spectrometer, Scanning electron microscope) appear in two different versions. The experimental results are presented and discussed in chapters 4 and 5; chapter 4 is focused on the measurements in the visible range, while chapter 5 is dedicated to the results of the IR measurements, the main part of this thesis.

All spectra presented in this thesis have an x-axis showing the wavenumber $\tilde{\nu} = \frac{E}{hc}$ in cm^{-1}. In the spectra of the visible range, the wavelength $\lambda[\text{nm}] = \frac{10^7}{\tilde{\nu}[\text{cm}^{-1}]}$ is shown in addition.

2. Fundamentals

2.1. Fourier Transform IR Spectroscopy (FTIR)

Already in the 1950s the first interferometric IR spectrometers came up, and the advantages over dispersive spectrometers had been realized [41]:

- Multiplex advantage (also: Fellget advantage)
  Contrary to dispersive spectroscopy, light of every frequency of the analysed spectrum reaches the detector at any time. This leads to a significant increase of the signal-to-noise ratio.
- Throughput advantage (also: Jaquinot advantage)
  The circular aperture enables a throughput of radiation, that is increased at least by a factor of six compared to the linear slit of a dispersive instrument.
- Connes advantage
  By means of a He-Ne laser, that is coupled into the spectrometer's interferometer, it is possible to determine the position of the movable mirror with an error smaller than 5 nm. Hence follows the high accuracy in the determination of the wavenumber, which is better than 0.01 cm^{-1}.

However, it took until the 1980s for IR spectroscopy to manage the break through, mainly because of the weak computer performance in earlier years.

The central element of an FTIR spectrometer is the interferometer, which is usually a Michelson interferometer (Fig. 2.1). The source Q emits light containing IR radiation. One exemplarily chosen plain electromagnetic wave with the angular frequency ω can be described by

$$E(\omega, t, z) = E_0 e^{i\omega\left(t-\frac{z}{c}\right)} \quad . \tag{2.1}$$

E_0 : complex amplitude
z : way along the optical path
c : speed of light in vacuum

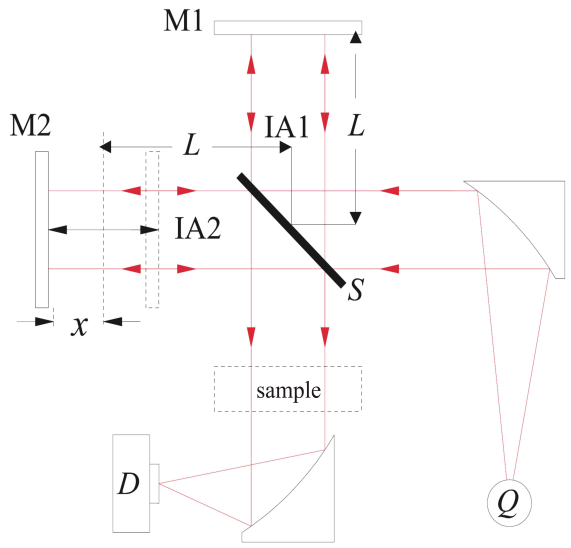

Figure 2.1: Optical path of a Fourier transform spectrometer with Michelson interferometer in transmission geometry, (Q) light source, (D) detector, (S) beamsplitter, (M1) stationary plane mirror, (M2) movable plane mirror, (x) mirror offset.

The time mean intensity of this wave is

$$p = 2c\epsilon_0 E_0 E_0^* \quad . \tag{2.2}$$

When this wave hits the beam splitter S, one part of the beam is reflected, while the other part gets through. In the case of an ideal beam splitter, the reflected and the transmitted part of the beam have the same intensity, and the amplitude of each is $\frac{E_0}{\sqrt{2}}$. Both parts of the beam are reflected by mirrors M1 and M2. While mirror M1 is stationary, M2 can be moved to both directions to the distance x from position L. Therefore, both parts of the beam have an optical retardation of $\gamma = 2x$ and a phase difference of $\delta\phi = \frac{\omega\gamma}{c}$. They fall back to the beam splitter, where each of them gets splitted again and two recombined beams are formed: one of them falls back to the light source and is lost. The other one shines through the sample and is finally focused on the detector D.

In case of a monochromatic light source, there is constructive interference, when the optical retardation is an integer multiple of the wavelength

$$\gamma = n\lambda, \quad (n = 0, 1, 2, ...) \quad , \tag{2.3}$$

the condition for destructive interference is

$$\gamma = \left(n + \frac{1}{2}\right)\lambda, \quad (n = 0, 1, 2, ...) \quad . \tag{2.4}$$

When mirror M1 is moved with constant velocity, the signal intensity at the detector shows sinusoidal behavior.

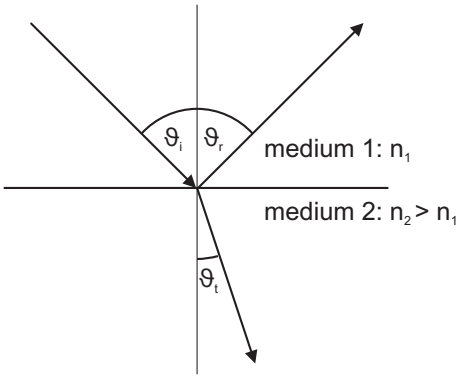

Figure 2.2: Reflection and refraction of light at the interface between two media having the refracting indices n_1 and n_2.

A broad band light source emits light of different frequencies, which have constructive interference (destructive, respectively) at different optical retardation. In the case of an ideal interferometer, light of every wavelength will interfere constructively, when the optical retardation is zero (zero path difference). This is the point of highest intensity at the detector (center burst). The relation between intensity and optical retardation—the interferogram—is given by

$$I(\gamma) = \int_{-\infty}^{+\infty} \frac{1}{2} p(\lambda) \left[1 + \cos\left(2\pi \frac{\gamma}{\lambda}\right)\right] d\lambda \ . \tag{2.5}$$

$p(\lambda)$: intensity of the light source

In this expression, the spectral information is carried by the alternating term, therefore the constant term is filtered out. Since the interferogram is the Fourier transformed of the spectrum, the spectrum is obtained by Fourier retransformation of the interferogram

$$S(\tilde{\nu}) = \int_{-\infty}^{+\infty} I(\gamma) \exp(-i2\pi\tilde{\nu}\gamma)\, d\gamma \ . \tag{2.6}$$

The spectrum is not only influenced by the sample, but also e. g. by the spectral characteristic of the light source, the beam splitter, and the detector. Therefore a reference spectrum (background spectrum) is usually taken without sample, then the quotient between the single channel sample spectrum and the single channel reference spectrum forms the relative spectrum of the sample.

2.2. Transmission and reflection of light at interfaces

If electromagnetic radiation hits an interface between two translucent non absorbing media having refraction indices n_1 and n_2 ($n_{12} = \frac{n_1}{n_2} < 1$), one part of the beam is

reflected and the other part is refracted (Fig. 2.2). While the angle of the reflected beam ϑ_r equals the angle of the incoming beam ϑ_i, the angle of the refracted transmitted beam ϑ_t yields Snellius' law

$$\sin\vartheta_\mathrm{t} = n_{12}\sin\vartheta_\mathrm{i} \quad . \tag{2.7}$$

Reflection and transmission coefficients for p- and s-polarization[1] can be calculated with the Fresnel formula [42]

$$r_\mathrm{p} = \frac{E_\mathrm{r,p}}{E_\mathrm{i,p}} = -\frac{n_2\cos\vartheta_\mathrm{i} - n_1\cos\vartheta_\mathrm{t}}{n_2\cos\vartheta_\mathrm{i} + n_1\cos\vartheta_\mathrm{t}} \quad , \tag{2.8}$$

$$t_\mathrm{p} = \frac{E_\mathrm{t,p}}{E_\mathrm{i,p}} = -\frac{2n_1\cos\vartheta_\mathrm{i}}{n_2\cos\vartheta_\mathrm{i} + n_1\cos\vartheta_\mathrm{t}} \quad , \tag{2.9}$$

$$r_\mathrm{s} = \frac{E_\mathrm{r,s}}{E_\mathrm{i,s}} = -\frac{n_1\cos\vartheta_\mathrm{i} - n_2\cos\vartheta_\mathrm{t}}{n_1\cos\vartheta_\mathrm{i} + n_2\cos\vartheta_\mathrm{t}} \quad , \tag{2.10}$$

$$t_\mathrm{s} = \frac{E_\mathrm{t,s}}{E_\mathrm{i,s}} = -\frac{2n_1\cos\vartheta_\mathrm{i}}{n_1\cos\vartheta_\mathrm{i} + n_2\cos\vartheta_\mathrm{t}} \quad , \tag{2.11}$$

where $E_{i,j}$ mean the p- or s-component of the $\overrightarrow{E}$-vector of the incoming (i), reflected (r) or transmitted (t) beam. The reflectivity R and the transmittance T are, if no absorption takes place

$$R_\mathrm{p,s} = |r_\mathrm{p,s}|^2 \quad , \tag{2.12}$$

$$T_\mathrm{p,s} = \frac{n_2\cos\vartheta_\mathrm{t}}{n_1\cos\vartheta_\mathrm{i}}\,|t_\mathrm{p,s}|^2 = 1 - R_\mathrm{p,s} \quad . \tag{2.13}$$

If the the angle of incidence is perpendicular to the interface, the expressions for the reflection coefficients simplify to

$$r_\mathrm{p} = r_\mathrm{s} = \frac{1-n_{12}}{1+n_{12}} \quad , \tag{2.14}$$

and the reflectivity becomes

$$R = \left(\frac{1-n_{12}}{1+n_{12}}\right)^2 \quad . \tag{2.15}$$

Absorbing materials can be described with a complex refraction index

$$n_i = n_i' + i\kappa_i \quad , \tag{2.16}$$

[1] p-polarization means, that the $\overrightarrow{E}$-vector is parallel to the plane of incidence, while it is perpendicular to the plane of incidence in case of s-polarization.

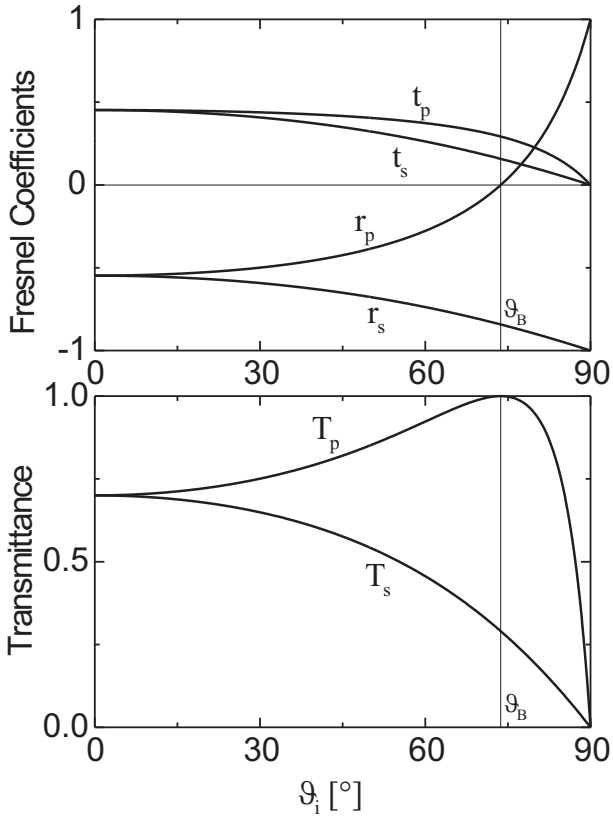

Figure 2.3: Fresnel coefficients (top) and transmittance (bottom) at the vacuum/Si interface ($n_2 = 3.4$) for p- and s-polarized light with $\tilde{\nu} = 2000\,\mathrm{cm}^{-1}$ and $A = 0$. ϑ_B marks the Brewster angle.

where n_i' is the real refraction index and κ_i the absorption coefficient. If absorption takes place, this leads to complex reflection and transmission coefficients in (2.8-2.11) and (2.12) and (2.13) must be modified:

$$R_\mathrm{p,s} = r_\mathrm{p,s} r_\mathrm{p,s}^* \ , \tag{2.17}$$

$$T_\mathrm{p,s} = \frac{n_2 \cos\vartheta_\mathrm{t}}{n_1 \cos\vartheta_\mathrm{i}} t_\mathrm{p,s} t_\mathrm{p,s}^* = 1 - R_\mathrm{p,s} - A_\mathrm{p,s} \ . \tag{2.18}$$

Fig. 2.3 shows the transmission and reflection coefficients as well as the transmittance of a vacuum/Si interface ($n_{12} = \frac{n_1}{n_2} < 1$), assuming the case of no absorption. In case of perpendicular incidence, T_p and T_s are identical, because it is not possible to differ between p- and s-polarization. While T_s decreases monotonically with increasing ϑ_i, T_p reaches a maximum before both become zero at $\vartheta_\mathrm{i} = 90$. At the maximum $T_\mathrm{p} = 1$; this is the case, if ϑ_i equals the Brewster angle ϑ_B, that is given by

$$\tan\vartheta_\mathrm{B} = \frac{1}{n_{12}} \ . \tag{2.19}$$

In this case, the transmitted and the reflected beam are perpendicular. Because the p-component of the beam is transmitted completely, the reflected beam is completely s-polarized.

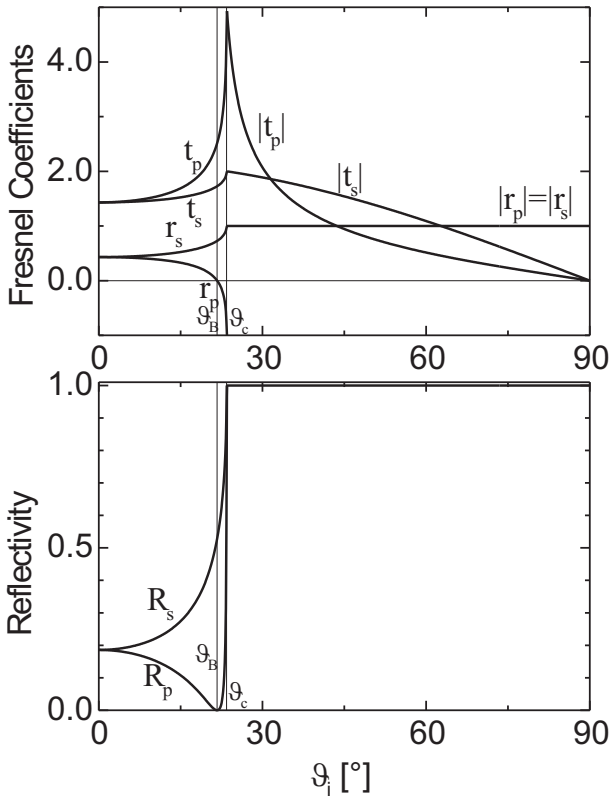

Figure 2.4: Fresnel coefficients (top) and reflectivity (bottom) at the Si/water interface ($n_1 = 3.4$, $n_2 = 1.4$) for p- and s-polarized light with $\tilde{\nu} = 2000\,\mathrm{cm}^{-1}$ and $A = 0$. The Brewster angle and the critical angle of total reflection are marked by ϑ_B and ϑ_c, respectively.

Fig. 2.4 shows the transmission and reflection coefficients as well as the reflectivity of an interface in case of $n_{12} = \frac{n_1}{n_2} > 1$, assuming the case of no absorption. If $\vartheta_\mathrm{i} \geq \vartheta_\mathrm{c}$ with

$$\sin\vartheta_\mathrm{c} = \frac{1}{n_{12}} \quad , \tag{2.20}$$

then the Fresnel coefficients are complex, and $R_\mathrm{p} = R_\mathrm{s} = 1$; the beam is totally reflected at the interface. The angle ϑ_c is called the critical angle of total reflection. Even though light is totally reflected at the interface for $\vartheta_\mathrm{i} \geq \vartheta_\mathrm{c}$, electromagnetic radiation does reach into the rarer medium, shown by the fact that the absolute values of the transmission coefficients are larger than zero. This effect, which is used in ATR spectroscopy is further discussed in chap. 2.4.3.

2.3. Thin film optics

When measuring IR spectra of thin films, reflection and transmission of light at several interfaces has to be considered. The case of a thin film on a semi-infinite substrate is shown in Fig. 2.5. If the coherence length of the light is larger than the thickness of the thin film, a coherent approach has to be made. A light beam hitting the interface

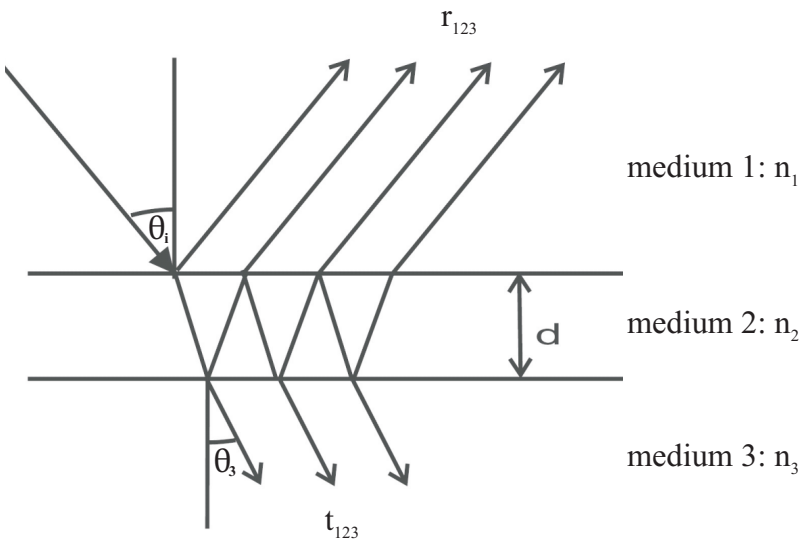

Figure 2.5.: Reflection and transmission at the interfaces of a thin film between two semi-infinite media.

between media 1 and 2 is considered. As mentioned in the previous section, one part of the beam is reflected at the interface (Fresnel coefficient r_{12}) and therefore contributes to the reflectivity, while the other part is transmitted, as any kind of absorption is neglected. This part of the beam hits the second interface, where again one part is transmitted and therefore contributes to the transmittance, while the other part is reflected and hits the first interface again. Here the beam is splitted again, and so on. This can be expressed with the Fresnel coefficients r_{123} and t_{123}, where the index "s" or "p" for the respective polarization is left out for simplicity [42]:

$$\begin{aligned} r_{123} &= r_{12} + t_{12}e^{i\beta}r_{23}^{i\beta}t_{21} + t_{12}e^{i\beta}r_{23}e^{i\beta}r_{21}e^{i\beta}r_{23}e^{i\beta} + ... \\ &= r_{12} + t_{12}r_{23}t_{21}e^{2i\beta}\left(1 + r_{21}r_{23}e^{2i\beta} + ...\right) \\ &= r_{12} + \frac{t_{12}r_{23}t_{21}e^{2i\beta}}{1 - r_{21}r_{23}e^{2i\beta}} \ , \end{aligned} \tag{2.21}$$

$$\begin{aligned} t_{123} &= t_{12}e^{i\beta}t_{23}\left[1 + r_{21}r_{23}e^{2i\beta} + \left(r_{21}r_{23}e^{2i\beta}\right)^2 + ...\right] \\ &= \frac{t_{12}t_{23}e^{i\beta}}{1 - r_{21}r_{23}e^{2i\beta}} \ . \end{aligned} \tag{2.22}$$

Here 2β accounts for the phase shift of a wave that went through the thin film and back once, compared to a wave that was directly reflected at the first interface. From geometric considerations follows

$$\beta = 2\pi\nu d\sqrt{n_2^2 - \sin^2\vartheta_\mathrm{i}} \ . \tag{2.23}$$

The transmittance and reflectivity are then obtained with

$$R = |r_{123}|^2 \ , \tag{2.24}$$

$$T = \frac{n_3\cos\vartheta_3}{n_1\cos\vartheta_\mathrm{i}}\,|t_{123}|^2 \ . \tag{2.25}$$

For non-absorbing layers this can be written as [42]

$$R = \frac{r_{12}^2 + r_{23}^2 + 2r_{12}r_{23}\cos 2\beta}{1 + r_{12}^2 r_{23}^2 + 2r_{12}r_{23}\cos 2\beta} \ , \tag{2.26}$$

$$T = \frac{\frac{n_3\cos\vartheta_3}{n_1\cos\vartheta_\mathrm{i}} t_{12}^2 t_{23}^2}{1 + r_{12}^2 r_{23}^2 + 2r_{12}r_{23}\cos 2\beta} \ . \tag{2.27}$$

It should be emphasized, that the assumption of a semi-infinite substrate is not met in reality, and a third interface—the backside of the substrate—has to be considered as well. In reality, the back side of the substrate often gives rise to multilayer interference, where the distance between a maximum and the neighboring minimum is [42]

$$|\nu_\mathrm{max} - \nu_\mathrm{min}| = \frac{1}{4d\sqrt{n_2^2 - \sin^2\vartheta_\mathrm{i}}} \ . \tag{2.28}$$

SCOUT

The calculations of IR and VIS spectra in chap. 4 were done with the software "SCOUT" [43]. This program calculates transmission, reflection, and ATR spectra of multilayer systems according to the matrix formalism, that is discussed in [42]. By defining and adapting layer stacks and the optical properties of the layers, spectra can be simulated quantitatively.

2.4. Measuring geometries

Several measuring geometries exist for the IR spectroscopical investigation of adsorbates on thin films. The choice of the measuring geometry usually depends on the

(a) External reflection (IRRAS)

(b) Attenuated total reflection (ATR)

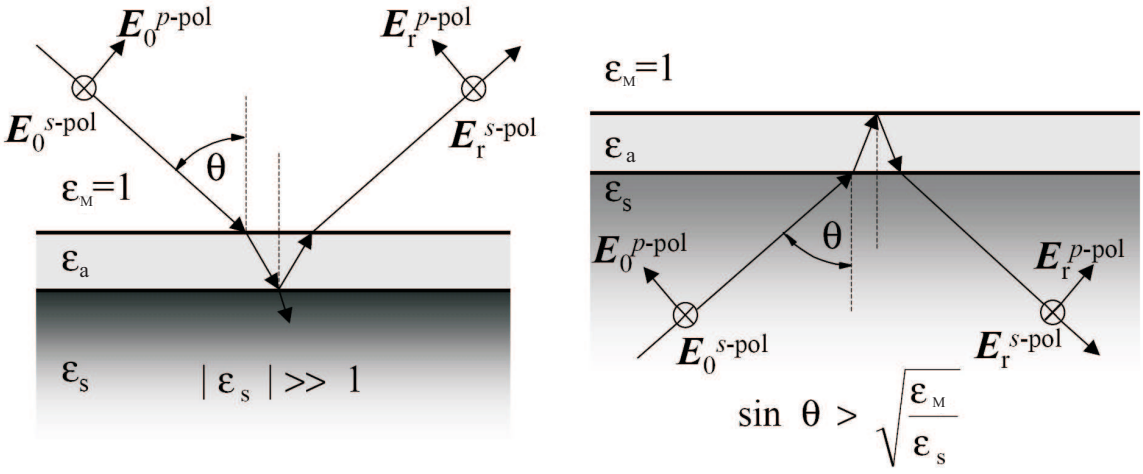

(c) Transmission

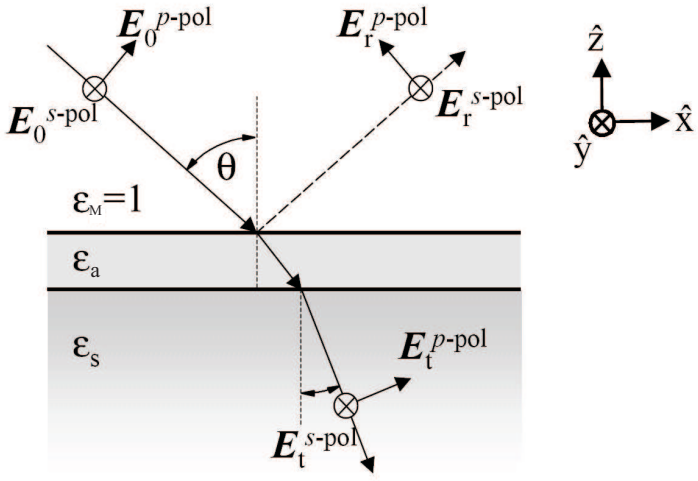

Figure 2.6.: Geometries for the measurement of an adsorbate layer on a substrate, (a) external reflection (IRRAS), (b) attenuated total reflection (ATR), (c) transmission, where ϵ_M is the dielectric function of the surrounding medium (here: vacuum), ϵ_s the dielectric function of the substrate, and ϵ_a is the dielectric function of the adsorbate layer. Taken from [44].

properties of the investigated system, e. g. the substrate being transparent or absorbing, the adsorbate layer being isotropic or anisotropic (dipole orientation normal or parallel to surface), the surrounding medium being vacuum or liquid, etc. The aim is, to maximize the light intensity at the position of the investigated system (to get a large absorption signal), and to maximize the light intensity at the detector (to have a good signal-to-noise ratio).

2.4.1. IR transmission spectroscopy

IR transmission geometry (Fig. 2.6c) is well suited to investigate adsorbates on substrates that show no or only low absorption of infrared radiation, e. g. ionic crystals in the mid IR. In many cases the angle of incidence is perpendicular to the surface, or it equals the Brewster angle. In case of perpendicular transmission, only the dielectric function $\epsilon_{a\parallel}$ of the adsorbate layer can be measured. In case of angular incidence, both, $\epsilon_{a\parallel}$ and $\epsilon_{a\perp}$ influence the transmission spectrum, however, if s-polarized radiation is used, only $\epsilon_{a\parallel}$ is measured.

The normal transmission of an adsorbate layer on a thin transmitting film is approximately given by [3, 45]

$$\frac{T}{T_0} \approx 1 - \frac{2\omega}{c(n_s + 1)} d_a \operatorname{Im} \epsilon_{a\parallel} \quad . \tag{2.29}$$

n_s : refraction index of substrate
d_a : adsorbate layer thickness
ϵ_a : dielectric function of adsorbate layer

2.4.2. IR reflection absorption spectroscopy (IRRAS)

The IR reflection absorption spectroscopy (abbreviated IRRAS or IRAS, and also known as external reflection spectroscopy) is well suited for investigation of adsorbates on substrates, that have a high reflectivity of IR radiation, e. g. metals (Fig. 2.6a). For thick non-transparent metal films, this is the only method to perform IR spectroscopy. The electrons of an ideal metal surface screen the component of the electric field parallel to the surface [46], and only the component perpendicular to the surface remains. As a result of this, only adsorbate vibrations perpendicular to the surface can be excited [47]. To maximize the p-component of the electric field, IRRAS measurements are usually performed with grazing incidence. The use of p-polarized radiation is very common, because the s-polarized part of the radiation does not contribute to the signal and therefore decreases the signal-to-noise ratio.

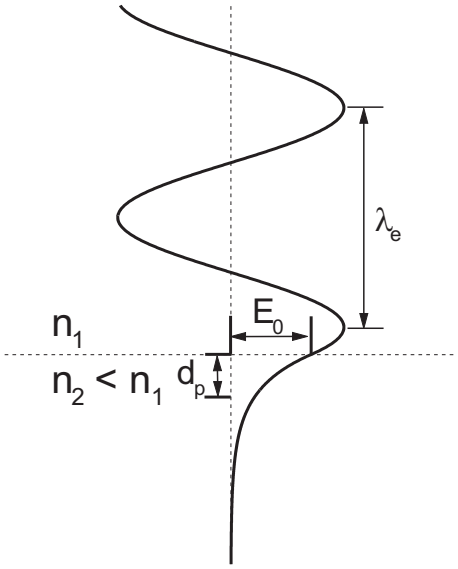

Figure 2.7: Evanescent electric field near the interface between two media at total reflection.

An estimation of the reflectance R of an adsorbate on an ideal metal substrate is given by [3, 48]

$$\frac{R}{R_o} \approx 1 - 4d_\mathrm{a}\frac{\omega}{c}\frac{\sin^2\vartheta_\mathrm{i}}{\cos\vartheta_\mathrm{i}}\,\mathrm{Im}\left(-\frac{1}{\epsilon_{\mathrm{a}\perp}}\right) \quad . \tag{2.30}$$

d_a : adsorbate layer thickness

ϵ_a : dielectric function of adsorbate layer

2.4.3. Attenuated total reflection (ATR) spectroscopy

This standard method for characterizing surfaces—also known as internal reflection spectroscopy (IRS)—was introduced by Harrick [49] and independently by Fahrenfort [50] (see Fig. 2.6b); it takes advantage of the effect of an occurring evanescent field, when an electromagnetic wave is totally reflected at the interface between an optically denser and a rarer medium. If there are absorbing molecules in the rarer medium, the total reflection will be attenuated, and the reflected light will carry the spectral information of the absorbing molecules.

The following considerations are based on the assumption, that no absorption takes place. It can be shown from Maxwell's equations, that inside the optically denser medium standing waves are established (see Fig. 2.7) due to the superposition of the incoming and the reflected beam [51]:

$$E = 2\cos\left(\frac{2\pi z}{\lambda_\mathrm{e}} + \varphi\right) \quad . \tag{2.31}$$

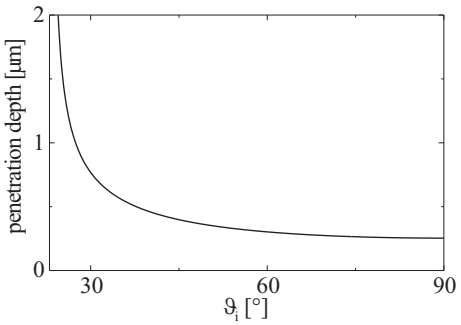

Figure 2.8: Depth of penetration of the electromagnetic field ($\tilde{\nu} = 2000\,\mathrm{cm}^{-1}$) at an interface between Si ($n_1 = 3.4$) and water ($n_2 = 1.4$)

These standing waves are perpendicular to the totally reflecting interface and have the wavelength

$$\lambda_\mathrm{e} = \frac{\lambda_1}{\cos\vartheta_\mathrm{i}} \ , \quad \lambda_1 = \frac{\lambda_0}{n_1} \ . \tag{2.32}$$

ϑ_i : angle of incidence
λ_0 : wavelength in vacuum

In the rarer medium, the standing wave is joined by an exponential decrease of the field (evanescent field):

$$E = E_0 \cdot e^{-\frac{z}{d_\mathrm{p}}} \tag{2.33}$$

d_p : depth of penetration

The depth of penetration d_p is the distance between the interface and the plane, where the intensity of the radiation has descended on $\frac{1}{e}$ of its original value E_0. It depends on the angle of incidence ϑ_i, the refracting indices of both media and the wavelength of the radiation [51]:

$$d_\mathrm{p} = \frac{\lambda_1}{2\pi\sqrt{\sin^2\vartheta_\mathrm{i} - n_{12}^2}} \ . \tag{2.34}$$

Fig. 2.8 shows the ϑ_i-dependence of the depth of penetration of the electromagnetic field at an interface between Si and water. There is no energy flux going from the denser medium into the rarer, following by the fact, that the time average component of the Poynting vector normal to the interface is zero [52]. When dipoles are placed within the evanescent field into the rarer medium, they are able to absorb light and absorption bands occur in the IR spectrum[2].

[2]In case of absorption in the rarer medium, the Poynting vector is not zero any more, and an energy flux occurs from the denser medium to the dipoles.

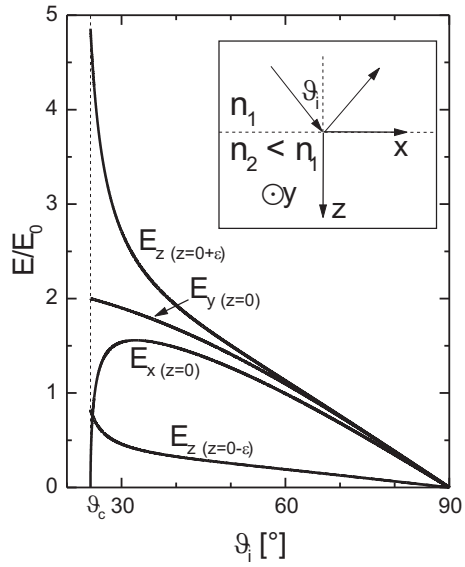

Figure 2.9.: Components of the electric field amplitude at the interface versus angle of incidence ϑ_i for a total internal reflection between Si ($n_1 = 3.4$) and water ($n_2 = 1.4$). The scale of the ordinate is normalized to the incident amplitude E_0. According to [51].

The electric field for total internal reflection at a non-absorbing interface was calculated in [53]. In the coordinate system shown in Fig. 2.9, the amplitudes of the electric field at the interface in the rarer medium 2 are [53]:

$$E_{y\,(z=0+\epsilon)} = \frac{2\cos\vartheta_\mathrm{i}}{\sqrt{1-n_{12}^2}} \ , \tag{2.35}$$

$$E_{x\,(z=0+\epsilon)} = \frac{2\sqrt{\sin^2\vartheta_\mathrm{i} - n_{12}^2}\cdot\cos\vartheta_\mathrm{i}}{\sqrt{1-n_{12}^2}\cdot\sqrt{(1+n_{12}^2)\sin^2\vartheta_\mathrm{i} - n_{12}^2}} \ , \tag{2.36}$$

$$E_{z\,(z=0+\epsilon)} = \frac{2\sin\vartheta_\mathrm{i}\cos\vartheta_\mathrm{i}}{\sqrt{1-n_{12}^2}\cdot\sqrt{(1+n_{12}^2)\sin^2\vartheta_\mathrm{i} - n_{12}^2}} \ . \tag{2.37}$$

In all of the three expressions above, a factor of 2 appears, because of the superposition of the incoming and the reflected beam. The total electric field amplitude is given by

$$E_{\perp\,(z=0+\epsilon)} = E_{y\,(z=0+\epsilon)} \ , \tag{2.38}$$

$$E_{\parallel\,(z=0+\epsilon)} = \sqrt{\left|E_{x\,(z=0+\epsilon)}\right|^2 + \left|E_{z\,(z=0+\epsilon)}\right|^2} \ . \tag{2.39}$$

Fig. 2.9 shows the ϑ_i-dependence of E_x, E_y and E_z at the Si/water interface. Because of boundary conditions, the tangential components of the electric fields are continuous

at the interface, therefore $E_{x\,(z=0+\epsilon)} = E_{x\,(z=0)}$ and $E_{y\,(z=0+\epsilon)} = E_{y\,(z=0)}$. However, the normal component E_z is discontinuous at the interface. In the denser medium, $E_{z\,(z=0-\epsilon)} = \frac{2}{n_{12}}$, and in the rarer medium $E_{z\,(z=0+\epsilon)} = 2n_{12}$. As can be seen in Fig. 2.9, the field amplitudes for both polarizations reach a maximum near the critical angle ϑ_c. At this angle $E_{y\,(z=0)} = 2$; this is a result of the superposition of the incoming and the reflected wave. Both, $E_\parallel$ and $E_\perp$ reach their maximum at the critical angle ϑ_c.

Unlike in normal transmission spectroscopy or IRRAS spectroscopy on nearly ideal metal surfaces, $\vec{E}$-fields exist in all spatial directions, therefore dipoles of all orientations will absorb radiation. However, because $E_{z\,(z=0+\epsilon)}$ is larger than $E_{x\,(z=0)}$ and $E_{y\,(z=0)}$, dipoles in the rarer medium will absorb stronger, when orientated perpendicularly to the interface.

Because the penetration depth of the evanescent field is typically in the same order of magnitude as the wavelength, ATR spectroscopy is well suited for the analysis of strongly absorbing samples. Also for the spectroscopy of adsorbate molecules on solid/liquid surfaces, ATR may be the only possible geometry, if the liquid absorbs IR radiation. Often multi reflection ATR crystals are used to increase the signal-to-noise ratio and therefore the detection sensitivity. A very detailed overview about ATR spectroscopy is given in the book by Harrick [51].

2.5. The Drude model

The description of optical properties of metals is often done with a model dating back to Paul Drude, who transferred the principals of kinetic gas theory to conduction electrons in metals. Drude considered the conduction electrons in metals as quasi-free, i. e. there is no significant interaction between electrons among each other, nor are there between electrons and the metal ion cores. After an average collision time τ the electrons perform collisions mainly with irregularities of the lattice, such as atomic defects and phonons; these collisions can be considered as frictional resistance. After every collision each direction of an electron has the same probability. The movement of an electron having the charge e and the effective mass m^* under influence of an external electric field $\vec{E}$ can be described with the differential equation

$$m^*\ddot{\vec{r}} + m^*\omega_\tau\dot{\vec{r}} = -e\vec{E} \ . \tag{2.40}$$

$\omega_\tau = \tau^{-1}$: rate of scattering

When considering a homogeneous isotropic medium under the influence of an external alternating electromagnetic field $\vec{E}(t) = \vec{E}_0 e^{-i\omega t}$, the dynamic conductivity is given by

$$\sigma_{\mathrm{dyn}} = \frac{n_{\mathrm{e}} e^2}{m^* \omega_\tau} \cdot \frac{1}{1 - i\omega/\omega_\tau} = \frac{\sigma_0}{1 - i\omega/\omega_\tau} \ , \tag{2.41}$$

where

$$\sigma_0 = \frac{n_{\mathrm{e}} e^2}{m^* \omega_\tau} \tag{2.42}$$

is the static conductivity, and n_{e} the charge carrier density. Finally, using the plasma frequency

$$\omega_p = \sqrt{\frac{ne^2}{\epsilon_0 m^*}} \ , \tag{2.43}$$

the dynamic conductivity can be written as

$$\sigma_{\mathrm{dyn}}(\omega) = \frac{\epsilon_0 \omega_{\mathrm{p}}^2(\omega)}{\omega_\tau(\omega) - i\omega} \quad . \tag{2.44}$$

From this follows, using the Maxwell equation

$$\mathrm{rot} H = \dot{\vec{D}} + \vec{j} \tag{2.45}$$

and the material equation

$$\vec{D} = \epsilon \epsilon_0 \vec{E} \quad , \tag{2.46}$$

the relation for the dielectric function

$$\epsilon(\omega) = \epsilon_1(\omega) + i\epsilon_2(\omega) = \epsilon_\infty + \chi^{\mathrm{D}}(\omega) = \epsilon_\infty + i\frac{\sigma_{\mathrm{dyn}}(\omega)}{\epsilon_0 \omega} \ , \tag{2.47}$$

where ϵ_∞ is the background polarization and $\chi^D(\omega)$ the polarization of free electrons according to Drude. The correlation between the dielectric function $\epsilon(\omega)$ and the complex index of refraction $\tilde{n}(\omega)$ is given by

$$\tilde{n}(\omega) = n(\omega) + i\kappa(\omega) = \sqrt{\epsilon_1(\omega) + i\epsilon_2(\omega)} \ . \tag{2.48}$$

$n(\omega)$: real index of refraction
$\kappa(\omega)$: absorption coefficient

Finally, using (2.44) and (2.48), the following relations are obtained for the rate of scattering ω_τ and the plasma frequency ω_{p}:

$$\omega_\tau(\omega) = \frac{\omega \epsilon_2}{\epsilon_\infty - \epsilon_1} \ , \tag{2.49}$$

$$\omega_p(\omega) = \sqrt{(\epsilon_\infty - \epsilon_1) \cdot (\omega^2 + \omega_\tau^2)} \ . \tag{2.50}$$

The equations for the real and imaginary part of the dielectric function are then:

$$\epsilon_1(\omega) = \epsilon_\infty - \frac{\omega_\mathrm{p}^2}{\omega^2 + \omega_\tau^2} \ , \tag{2.51}$$

$$\epsilon_2(\omega) = \frac{\omega_\mathrm{p}^2 \omega_\tau}{\omega^3 + \omega\omega_\tau^2} \ . \tag{2.52}$$

While these considerations are valid for the IR range, interband transitions must be considered, when describing the optical properties in the visible range. This is done by substituting $\epsilon_\infty = \text{const.}$ in eq. (2.47) by a term accounting for interband transitions, as shown in the next section.

2.6. Optical properties of Au nanoparticles

Optical properties of bulk Au

The complex dielectric function including all optical properties of a real metal in the visible range is given by [54],

$$\epsilon(\omega) = 1 + \chi^{\mathrm{IB}}(\omega) + \chi^{\mathrm{D}}(\omega) \ , \tag{2.53}$$

where $\chi^{\mathrm{D}}(\omega)$ is the polarization of free electrons according to Drude, and $\chi^{\mathrm{IB}}(\omega)$ is a contribution due to interband transitions (excitations of d-electrons). Compared to eq. (2.47) this corresponds to a substitution of the constant ϵ_∞ by the term $1 + \chi^{\mathrm{IB}}(\omega)$. Fig. 2.10 shows the dielectric function of bulk Au. Like the other metals the dielectric function of Au in the IR is characterized by a negative ϵ_1 and a positive ϵ_2, both with decreasing absolute values on the near IR side. In the visible range ϵ_1 becomes zero at the frequency ω_0 and it is positive for $\omega > \omega_0$. On the other hand, ϵ_2 increases strongly in the VIS, because in this range it is dominated by interband transitions. As can be seen in Fig. 2.10, $\omega_0 \approx 44100\,\mathrm{cm}^{-1}$ ($\lambda_0 \approx 227\,\mathrm{nm}$). In the region $\omega \ll \omega_0$, light is almost completely unable to penetrate the metal and is reflected to a very high grade. In this region metals have the typical high reflectivity due to the large number of free charge carriers, which is of the order of $10^{22} \frac{1}{\mathrm{cm}^3}$ [55]. The threshold energy for interband transitions in Au was found to be at $19190\,\mathrm{cm}^{-1}$ ($521\,\mathrm{nm}$) [56] and at $19760\,\mathrm{cm}^{-1}$ ($506\,\mathrm{nm}$) [55], respectively. For $\omega > \omega_0$, ϵ_1 is approximating to unity. Interband transitions give contributions, but cannot significantly influence ϵ_1

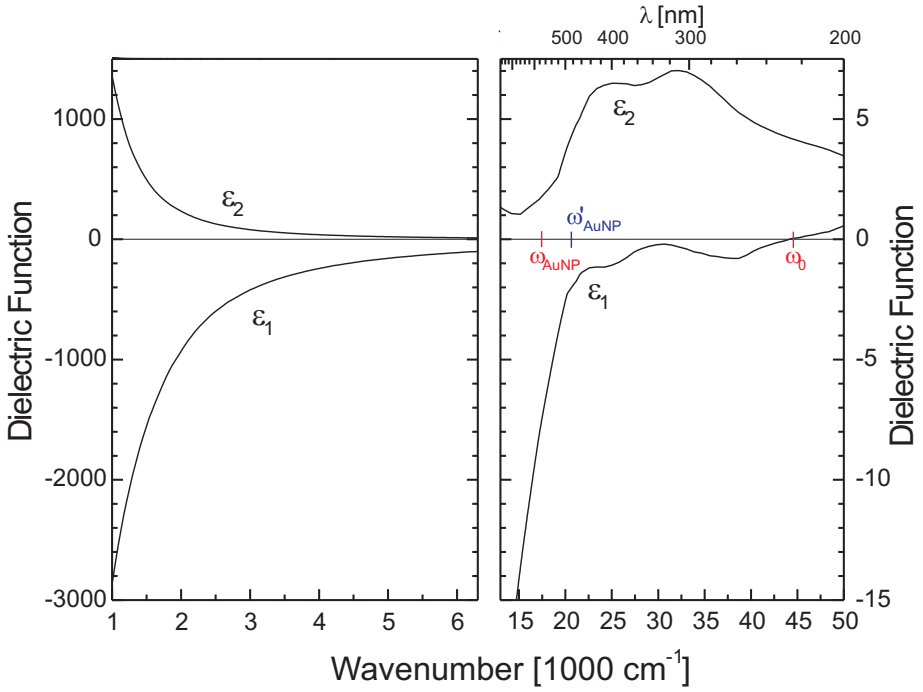

Figure 2.10.: Dielectric function of bulk Au in the mid IR (left) and the UV/VIS range (right, different scale). The data are a composition of the data published in [58] and [59] and obtained through the SCOUT database [43].

[57]. With $\epsilon_1 \rightarrow 1$, the reflectivity becomes zero and the metal is transparent (UV transparency of metals). The increase of absorption due to interband transitions and the decreasing reflection in the violet range are the reason for the typical yellow shine of bulk Au.

The optical properties of metal nanoparticles have already been investigated more than 100 years ago by Faraday [60] and Mie [61], however, several thousands of years before they had already been used for medical applications and to color glass. A very famous example is the Roman Lycurgus Cup, which dates back to the fourth century B. C. This cup looks green in reflected light and red in transmitted light. The reason for this is the presence of AuNP and their optical properties, that are very different from the ones of bulk Au with its typical yellow metallic shine.

Optical properties of metal nanoparticles are dominated by a surface plasmon polariton resonance of the conduction electrons. When excited by an external electromagnetic field, the formation of a dipole in the nanoparticle is induced. A compensating restoring force in the nanoparticle causes the conduction electrons to perform collective oscillations. Because of the presence of free conduction electrons, these properties are mainly observed in Au, Ag, and Cu [62]. The resonance frequency depends on factors such as

size and shape of the nanoparticles as well as the properties of the surrounding medium [63].

Metal spheres

The general solution of the diffraction problem of a single sphere of arbitrary material surrounded by an embedding medium was first given by Mie in 1908 [61]. He applied Maxwell's equations with appropriate boundary conditions in spherical coordinates using multipole expansions of the incoming electric and magnetic fields; input parameters were the particle size and the optical functions of both, particle material and the surrounding medium. The total Mie extinction consists of multipolar contributions (dipolar, quadrupolar, octupol, etc.). Each multipole contributes by electric and magnetic modes, i. e. plasmons and eddy currents, which each consist of absorption and scattering losses [54].

Small metal spheres and nanoparticles

For metal clusters in the quasi-static regime ($R \ll \lambda$), phase retardation and higher multipoles (extrinsic size effects) become negligible, and dipolar absorption is the dominating effect of extinction [54]. At even smaller size of the particles (e. g. $R < 25\,\mathrm{nm}$ to $30\,\mathrm{nm}$ for AuNP [64]), intrinsic size effects occur, as the mean free path of the conduction electrons is now influenced by surface scattering. This leads to a size dependence of the dielectric function of the particles and can be written as an additive correction term in the dielectric function of the bulk metal:

$$\epsilon_{\mathrm{part}} = \epsilon_{\mathrm{bulk}} + \Delta\epsilon(R) \quad . \tag{2.54}$$

This is taken into account by adding a correction term to the Drude scattering rate (2.49) [64]:

$$\omega_\tau = \omega_{\tau\,\mathrm{bulk}} + \alpha\frac{\nu_\mathrm{F}}{R} \quad , \tag{2.55}$$

where ν_F is the Fermi velocity of the electrons in the metal. The factor α describes elastic electron scattering from the surface of the particle and interface damping, that is caused by adsorbate induced resonant states, if the particle is covered by adsorbate or an embedding medium [64],

$$\alpha = \alpha_{\mathrm{surface}} + \alpha_{\mathrm{adsorbate}} \quad . \tag{2.56}$$

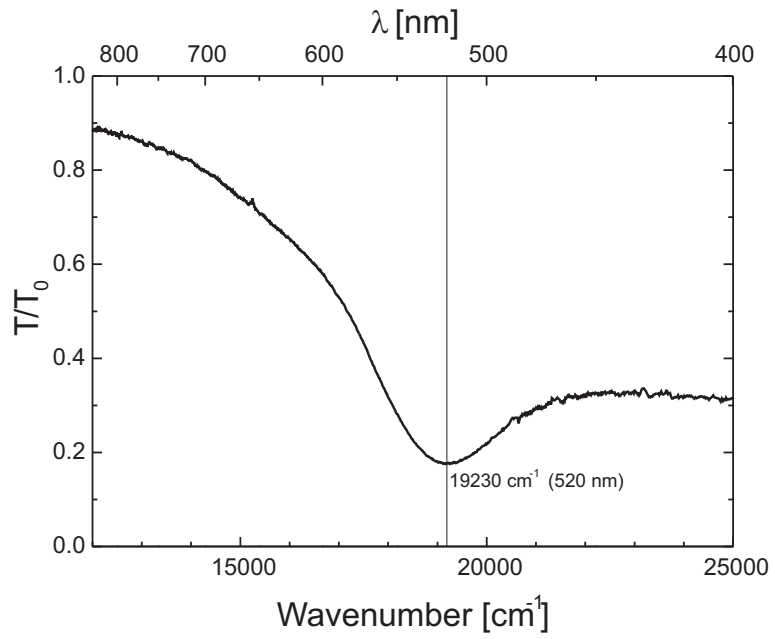

Figure 2.11.: VIS transmission spectrum of AuNP ($2R \approx 13\,\mathrm{nm}$, $c \approx 7.5 \times 10^{12}\,\frac{\mathrm{particles}}{\mathrm{ml}}$) in colloidal suspension, layer thickness 4 mm.

Width and Shape of the resonance peak

According to Mie's theory, the resonance frequency of spherical particles in the quasi-static limit should fulfill the condition $\epsilon_1 = -2$, and the line shape should—in the vicinity of the resonance—be described by a Lorentzian [54]. As can be seen in Fig. 2.10, $\epsilon_1 = 2$ is given for $\omega'_{\mathrm{AuNP}} \approx 20700\,\mathrm{cm}^{-1}$ ($\lambda'_{\mathrm{AuNP}} \approx 483\,\mathrm{nm}$). An experimental value—approximated by the position of the peak minimum—is given by $\omega_{\mathrm{AuNP}} \approx 19230\,\mathrm{cm}^{-1}$ ($\lambda_{\mathrm{AuNP}} \approx 520\,\mathrm{nm}$), as shown in Fig. 2.11. In addition to this discrepancy, also the shape of the measured resonance curve does not fit quantitatively to Mie's theory. The reasons for that are on the one hand idealizing assumptions of the theory, e. g. monodisperse spherical particles, or Maxwellian boundary conditions, that are not met in reality. On the other hand, the size effects, that are mentioned above, were not considered by Mie. Finally and most important, the contribution of interband transitions, that also were not considered by Mie, must be taken into account, i. e. the constant ϵ_∞ must be substituted by $1 + \chi^{\mathrm{IB}}$, because the excitation of electrons from the energetically deeper d-band into the conduction s-band is often crucial for the optical properties of metallic nanoparticles [54, 64].

In [64] a theory developed by Persson [65], neglecting interband transitions, is extended to realistic metals in an embedding medium by taking into account these effects. For nanoparticles in vacuum, this was done before by Zaremba and Persson [66]. In [67]

for AuNP in colloidal suspension, an empiric calibration curve for the mean particle size ($2R_\mathrm{m}$) dependence of the spectral position of the absorption peak λ_abs as a result of intrinsic size effects is given:

$$2R_\mathrm{m}[\mathrm{nm}] = \sum_{n=0}^{3} A_n \left(\lambda_\mathrm{abs} - 500\right)^n \quad . \tag{2.57}$$

$$\begin{aligned} A_0 &: \quad 12.558 \\ A_1 &: \quad -2.593 \\ A_2 &: \quad 0.1921 \\ A_3 &: \quad -0.00253 \end{aligned}$$

2.6.1. Effective medium theories

Optical properties of AuNP films deposited on a surface can—similar to metal films produced by physical vapor deposition—be well described by the use of effective media theories. These theories consider the properties of both, the metallic particles and the surrounding medium.

Maxwell-Garnett model

The Maxwell-Garnett model was the first effective medium theory, which allows the determination of effective optical constants of such layers [68]. A derivation can be found in [69]. The effective medium theory of Maxwell-Garnett considers an ensemble of small metal particles embedded in a surrounding medium. The individual polarizabilities of the particles are summarized, and the local-field effects of the particles are taken into account. The external electromagnetic field polarizes the particles and therefore influences the electromagnetic near-field around them. The polarization $\vec{P}$ of a single sphere in a constant and uniform external electric field is uniform, and it's polarizability is given by

$$\alpha = 4\pi r^3 \frac{\epsilon_\mathrm{part} - \epsilon_\mathrm{M}}{\epsilon_\mathrm{part} + 2\epsilon_\mathrm{M}} \quad . \tag{2.58}$$

ϵ_part : dielectric constant of metal particles
ϵ_M : dielectric constant of embedding matrix
r : sphere radius

A sphere of this kind will have a resonance, if (2.58) has a minimum, i. e. if

$$|\epsilon_{\text{part}}(\omega) + 2\epsilon_{\text{M}}| = \min \ . \tag{2.59}$$

The frequencies fulfilling condition 2.59 are called "Fröhlich frequencies" ω_{F} [70]. If $\text{Im}\,\epsilon_{\text{part}}(\omega) = 0$, condition (2.59) is reduced to the Mie condition [61]:

$$\epsilon_{\text{part}}(\omega) = -2\epsilon_{\text{M}} \ . \tag{2.60}$$

The correlation between dielectric function and polarizability is given by the Clausius-Mossotti relation:

$$\alpha = \frac{3}{N}\frac{\epsilon_{\text{eff}} - 1}{\epsilon_{\text{eff}} + 2} \ . \tag{2.61}$$

ϵ_{eff} : effective dielectric constant of metal particles and embedding medium
N : number of particles per volume unit

From (2.58) and (2.61) follows the relation for the effective dielectric function, depending on the optical constants of the metal particles and the embedding medium as well as of the filling fraction [71]:

$$\frac{\epsilon_{\text{eff}} - \epsilon_{\text{M}}}{\epsilon_{\text{eff}} + 2\epsilon_{\text{M}}} = f\frac{\epsilon_{\text{part}} - \epsilon_{\text{M}}}{\epsilon_{\text{part}} + 2\epsilon_{\text{M}}} \ . \tag{2.62}$$

ϵ_{part} : dielectric constant of metal particles
ϵ_{M} : dielectric constant of embedding matrix
f : filling factor of metal particles

This is known as the Maxwell-Garnett effective medium expression [68], which is valid for a low filling fraction ($f \ll 1$) and for the effective dimension[3] $D = 3$. It is shown in chap. 4.1, that this model is able to describe the optical properties of the prepared AuNP suspension in a qualitative way.

[3] An effective dimension of $D = 3$ means, that the extension of the particles parallel to the surface and normal to the surface are equal, while $D = 2$ is used, if the extension parallel to the surface is much larger than normal to the surface.

Extended Maxwell-Garnett models

There are several extensions of the Maxwell-Garnett model, taking into account several effects like a particle size dependence of the effective medium, or an effective relative magnetic permeability of the medium, as discussed in [72]. One extended Maxwell-Garnett model, that is based on a calculation of size corrections to the depolarization factor is given by [72]

$$\epsilon_{\text{eff}} = \epsilon_{\text{M}} \frac{\epsilon_{\text{part}}(1+2f) + 2\epsilon_{\text{M}}(1-f) + (\epsilon_{\text{M}} - \epsilon_{\text{part}})(1-f)\Delta}{\epsilon_{\text{part}}(1-f) + \epsilon_{\text{M}}(2+f) + (\epsilon_{\text{M}} - \epsilon_{\text{part}})(1-f)\Delta} \quad , \tag{2.63}$$

where $\Delta = x^2 + \frac{2}{3}ix^3$, x being a sphere size parameter introduced in [72].

Bruggeman model

In case of AuNP being deposited on a substrate the condition $f \ll 1$ is not fulfilled any more, and the Maxwell-Garnett model cannot be used. Dipole-dipole interaction between the particles occurs, and the frequency of the particles are influenced by oscillating dipoles of the neighboring particles. An effective medium model for such systems is the one of Bruggeman, where the the effective dielectric constant follows from

$$(1-f)\frac{\epsilon_{\text{M}} - \epsilon_{\text{eff}}}{\epsilon_{\text{M}} + (D-1)\epsilon_{\text{eff}}} = f\frac{\epsilon_{\text{part}} - \epsilon_{\text{eff}}}{\epsilon_{\text{part}} + (D-1)\epsilon_{\text{eff}}} \quad , \tag{2.64}$$

where D is the effective dimension of the film. Eq. (2.64) is known as the Bruggeman formula [73]. In chap. 4.2, this model with $D = 3$ is used to describe the optical properties of AuNP films on glass substrate.

For percolated Au films ($f > \frac{1}{3}$ for $D = 3$, $f > \frac{1}{2}$ for $D = 2$) the Bruggeman model becomes increasingly incorrect, as the assumption of the particles being small compared to the wavelength of light is not suitable any more.

Other effective medium models

In the literature a lot of different effective medium models can be found, several of them are discussed in [71] and [74]. Usually, each model is based on different assumptions about the shape, orientation and number of basic unit cells and assumes different kinds of interaction; therefore each model has its own range of applicability. For example, Yamaguchi et al. [75] introduced an effective medium model, that was optimized for the description of a thin metal film consisting of ellipsoidal particles:

$$\epsilon_{\text{eff}} = 1 + f\frac{\epsilon_{\text{part}} - \epsilon_{\text{M}}}{1 + q\frac{\epsilon_{\text{part}} - \epsilon_{\text{M}}}{\epsilon_{\text{M}}}} \quad . \tag{2.65}$$

Here, q is a depolarization factor, that considers the non spherical shape of the particles [74].

A very recent model, that was optimized especially for describing extinction spectra of colloidal dispersion of AuNP in the visible range is shown in [76], where the dielectric function of Au is described as an extended Drude model with an additional Lorentzian term. The authors show, that this leads to good fit of the experimental values of the dielectric function obtained by Johnson and Christy [58].

2.7. The SEIRA effect

If a metal surface is not flat on a mesoscopic scale, but rather consists of metal islands, there can be an enhancement of the electromagnetic field between the particles by several orders of magnitude [77]. This enhancement is particularly high, if the metal film consists of densely packed, but yet separate islands [6, 7, 8]. The IR transmission spectra of adsorbates on such SEIRA active metal films may then show vibration lines, that are extraordinary strong and also asymmetric (Fano lines), because of near field interaction with plasmonic excitations of the metal islands. Due to the asymmetric shape of the vibration lines, the transmission minima are shifted to frequencies slightly below the vibration frequency. The maximum of SEIRA enhancement should be found between the metal particles at their smallest distance, according to the near field enhancement [3]. This is supported by the fact, that SEIRA spectra show mainly vibrations, that are orientated perpendicular to the sidewalls of the particles, as could be shown e. g. by the dipole-dipole interaction based shift of the CO-stretching frequency on iron films [78].

Mid-IR spectra of SEIRA active ultrathin metal films can be understood in terms of local optics and effective media models. One model that is known for a good approximation for similarly shaped metal nanoparticles in a random monolayer arrangement is the Bruggeman model, eq. (2.64), where ϵ_{M} is denoted by $\epsilon_{\mathrm{ads}\perp}$, if the space between the metal particles is completely filled by adsorbate, while f is the filling factor of the metal film. If the metal particles are covered by just one monolayer of adsorbate molecules, the oscillator strength in $\epsilon_{\mathrm{ads}\perp}$ is to reduced by the corresponding ratio. The description of the same system without adsorbate (reference system before adsorbate exposure) is done by substituting $\epsilon_{\mathrm{ads}\perp}$ by "1" for vacuum, giving the effective dielectric function $\epsilon_{\mathrm{eff},\,0}$. If the film is in contact with a different medium like e. g. a solvent, the corresponding value for ϵ has to be taken into account.

The transmittance T of a film covered with an adsorbate relative to that of a non-

exposed film is approximated by [3]

$$\frac{T}{T_0} \approx \frac{(1+n_\mathrm{s}) + 2\frac{\omega}{c} d_\mathrm{eff} \operatorname{Im} \epsilon_{\mathrm{eff},\,0}}{(1+n_\mathrm{s}) + 2\frac{\omega}{c} d_\mathrm{eff} \operatorname{Im} \epsilon_\mathrm{eff}} \quad , \tag{2.66}$$

where only the first order term of the film thickness d_eff is taken into account, which is valid for a film transmittance of about 90% to almost 100%.

Because ϵ_part is a complex frequency dependent function, the vibration lines of the adsorbate, that are originally Lorentzian-shaped become strongly asymmetric, because now both, $\operatorname{Re} \epsilon_{\mathrm{ads}\perp}$ and $\operatorname{Im} \epsilon_{\mathrm{ads}\perp}$ contribute to the IR spectra [3]. At the percolation threshold[4] this asymmetry is maximal [8].

2.8. Wet chemical preparation of Au nanoparticles and Au nanoparticle films

Many recipes can be found in the literature about wet chemical preparation of metal nanoparticles [79, 80]. Probably the most famous method was introduced by Turkevitch in 1951 [81] and further improved by Frens in 1973 [82]. Since this method leeds to monodisperse spherical AuNP with a tunable size, and also since this is a very established and rather simple method, it was used in this thesis.

2.8.1. Preparation of Au nanoparticles

Monodisperse spherical AuNP were prepared using the method of citrate reduction of $AuCl_4$ according to Turkevitch [81] and Frens [82]. Frens showed, that by changing the ratio of $AuCl_4$ and tri-sodium citrate, it is possible to tune the size of the monodisperse spherical AuNP in a range $10\,\mathrm{nm} \leq 2R \leq 150\,\mathrm{nm}$. The reaction taking place can simplified be written as

$$\mathrm{Au^{3+}Cl_4^-} + \mathrm{C_6H_5Na_3O_7} \longrightarrow \mathrm{Au^0_{NP}} + 4\mathrm{Cl^-} + 3\mathrm{Na^+} + \mathrm{C_6H_5O_7^{3-}}.$$

The tri-sodium citrate works as a reducing agent, which removes the Cl^- ions from the Au^{3+} ions, and then reduces the Au^{3+} ions to metallic Au, growing to monodisperse spherical particles. While the remaining Cl^- and Na^+ ions remain in the colloidal dispersion, the citrate molecules act as a negatively charged coating of the AuNP.

[4] The percolation threshold marks the crossover from an isolating discrete metal island morphology to a connected island network, that is conductive.

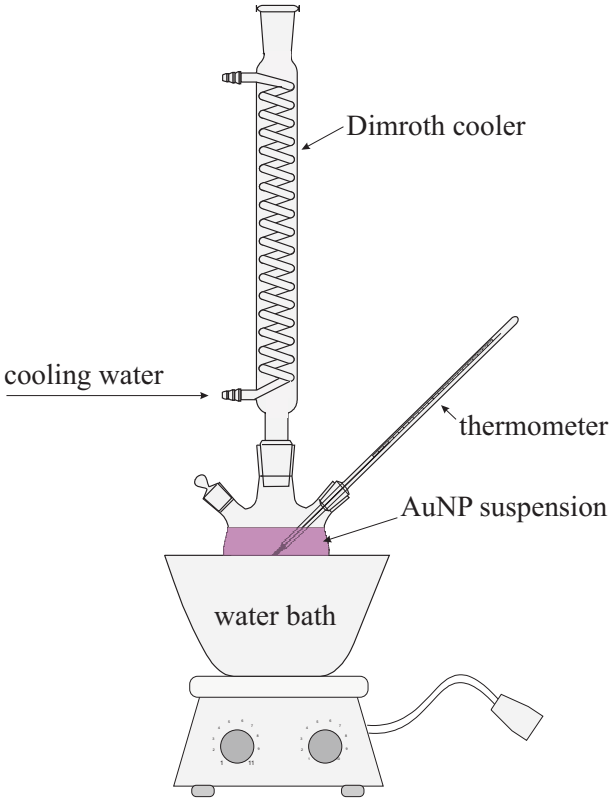

Figure 2.12: Setup for the preparation of Au nanoparticles according to Frens.

The resulting repulsive forces between the AuNP stabilize the suspension and keep the particles from settling down. Stored in the refrigerator, this suspension is stable for several months.

In this thesis, the amounts of $AuCl_4$ and tri-sodium citrate were used as published in [83] and [84], leading to a AuNP size of $2R \approx 13\,\text{nm} \pm 2\,\text{nm}$ (standard deviation). In detail, 100 ml of 1 mM aqueous solution of $AuCl_4$ are heated in a three neck flask (see Fig. 2.12). This is done under refluxing conditions, i. e. water vapor is condensed inside the Dimroth cooler and then fed back into the flask, in order to keep the concentrations at a constant level. During the complete process of preparation, the mixture inside the flask is stirred using a teflon covered magnetic stir bar. After the solution inside the flask has started boiling, 10 ml of 38.8 mM aqueous solution of tri-sodium citrate at room temperature are added. The following reduction process is indicated by characteristic color changes: After addition of the colorless tri-sodium citrate solution the originally yellow $AuCl_4$ solution turns clear, as the Cl^- ions are removed from the Au^{3+} ions. With increasing size of the AuNP, the color of the mixture changes from clear to dark blue to wine-red, according to the optical properties of the particles (see chap. 2.6). When the mixture has reached its final state after about two minutes, it is kept at boiling temperature for another 15 min and then let cool down to room temperature while still being stirred.

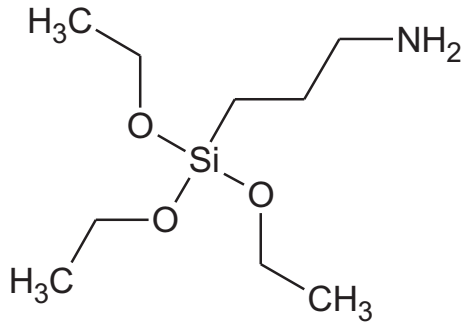

Figure 2.13: Chemical structure of the APTES molecule.

Materials $HAuCl_4$ (99.999% purity) was purchased from Aldrich. Tri-sodium citrate ($C_6H_5Na_3O_7$) was purchased at Merck in p. a. purity. Purified water (specific resistance $\approx 18\,\mathrm{M\Omega\,cm}$) was used.

2.8.2. Preparation of Au nanoparticle films

AuNP were immobilized onto SiO_2/Si substrates and onto glass substrates using the same recipe: First, the Si wafer (glass slides, respectively) are ultrasonically cleaned with methanol for 15 min. Then they are put into 10% solution of (amino-propyl)triethoxysilane (APTES, see Fig. 2.13) for one hour. This treatment replaces the OH groups adsorbed on the naturally grown SiO_2 layer with APTES molecules forming a monolayer, whereas their amino groups are orientated away from the substrate [85]. After taking the samples out, they are thoroughly rinsed with methanol, ultrasonically cleaned with methanol to remove any excess amount of APTES, rinsed with methanol again, and let dry in air. The samples are then annealed at 100°C for one hour to complete the Si-O bond formation [85]. After cooling down to room temperature, the samples are put into water for 10 min and then put into AuNP suspension. During this time, AuNP from dispersion are immobilized onto the substrate because of the affinity of the positively charged APTES amino group to the negatively charged citrate layer of the AuNP. Because of the repulsive forces between the AuNP, the deposition rate decreases with increasing coverage, resulting in a final state of a AuNP submonolayer on the substrate as shown in Fig. 5.3 on page 61. After one to three hours of exposition, the samples are taken out, rinsed with water and let dry in air.

Materials APTES and methanol were purchased in p. a. purity at Merck and J. Baker, respectively.

2.8.3. Growth of Au nanoparticles

In nanotechnology, a well known technique for the enlarging of AuNP is hydroxylamine growth of AuNP [79, 86, 87, 88, 89]. Thermodynamically, hydroxylamine (NH_2OH) is able to reduce Au^{3+} ions to metallic Au, however, this reaction is highly accelerated by the presence of Au surfaces [86]. For example, when AuNP—in solution or immobilized on a surface—are exposed to aqueous solution of $AuCl_4$ and hydroxylamine, the Au^{3+} ions get reduced by the hydroxylamine and the resulting metallic Au goes into growth of the existing nanoparticles completely. Nucleation of new particles in solution does not take place. Applying this technique to AuNP films on a substrate (e. g. prepared as described in chap. 2.8.2) will result in larger AuNP and therefore smaller distances between the particles. Finally the film will percolate and become conductive. In this thesis, two different recipes for hydroxylamine growth of AuNP were used, both of which can be found in the literature [79, 86, 87, 88, 89]:

Single step method

In this growth method, 50% solution of hydroxylamine in water is used. During the growth process, vigorous stirring is necessary to prevent particle nucleation in the solution. In detail, $AuNP/SiO_2/Si$ samples are exposed to aqueous solution of 0.3 mM $AuCl_4$ and 0.4 mM hydroxylamine while vigorously stirring. After a defined time, the process is terminated by taking out the samples, rinsing with water and letting dry in air.

Multi step method

This growth method requires the use of hydroxylamine hydrochloride. No stirring is needed during the growth process. In detail, $AuNP/SiO_2/Si$ samples are exposed to aqueous solution of 0.3 mM $AuCl_4$ and 0.4 mM hydroxylamine. This initiates a growth process of the AuNP lasting for about 1 min. After 2 min, the initial amount of $AuCl_4$ is added again to the solution; this process is repeated n times. After $2n$ min the process is terminated by taking out the samples, rinsing with water and letting dry in air.

Materials Aqueous solution of hydroxylamine (50%) was purchased at Merck, hydroxylamine hydrochloride was purchased at p. a. grade from Acros Organics.

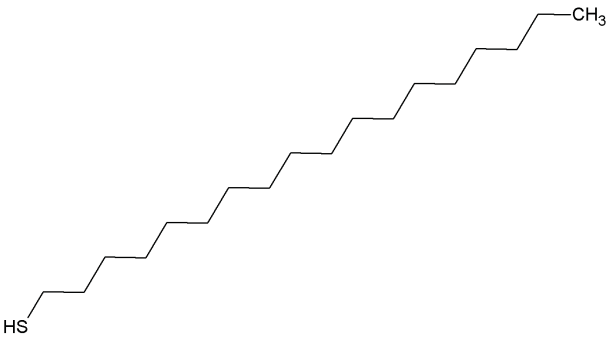

Figure 2.14: Structure of the octadecanethiol molecule.

2.9. Adsorbate molecules

The characterization of the AuNP films regarding SEIRA activity was done with adsorbate experiments using alkanethiol molecules, that have been widely investigated in the past [90, 91, 92, 93]. In following experiments biomolecules like antibodies and DNA have been investigated.

2.9.1. Alkanethiols

Alkanethiols—formerly known as mercaptans—are organic compounds containing one or more SH (thiol) groups as functional groups. Compared to alcohols, the oxygen atom is replaced by sulfur. The names of the alkanethiols are derived from the corresponding alkane and the ending "-thiol" (methanethiol, ethanethiol, etc.). Linear long chain alkanethiols like hexadecanethiol ($C_{16}H_{33}SH$) or octadecanethiol ($C_{18}H_{37}SH$, see Fig. 2.14) are commonly used for the preparation of self assembling monolayers (SAM). This is possible, because of the strong bond between the SH group and the Au surface. During the adsorption process of a SAM, the molecules are placed parallel next to each other on the surface (striped phase), as long as the coverage is low; with increasing coverage, the van der Waals interaction between the alkyl chains increases, leading to a standing up geometry, with the molecules being tilted with respect to the surface normal [91, 92]. Because the adsorbate-adsorbate interaction increases with rising length of the chains, long chained alkanethiols are usually preferred when preparing SAMs. The surface of a SAM is very inert preventing multilayer adsorption; however, by replacing the terminating methyl group with a different group, the chemical and physical properties of the surface can be modified. Typical applications of SAMs are protective coatings against corrosion, resist in lithography, modification of wetting and gliding properties of a surface, and surface modification for biosensing [91].

	Vibration	band position [cm^{-1}]	Strength
CH_3:	antisym. stretch	2952-2972	vs
	sym. stretch	2862-2882	vs
	antisym. bending	1440-1470	ms
	sym. bend.: -C(CH_3)	1370-1380	m
CH_2:	antisym. stretch	2916-2936	vs
	sym. stretch	2843-2863	vs
	scissor	1445-1475	ms
skeletal:	-$(CH_2)_n$- in phase, twist	1295-1305	-
	-$(CH_2)_n$- in phase, rock	720-726	m
	C-C skel. stretch	1120-1180	(doublet)
S-H stretch:	R-SH (liquid)	2560-2590	w
C-S stretch	R-SH	650-660	w

(a)

	Vibration	band position [cm^{-1}]
CD_3	sym. stretch	2073
CD_2	sym. stretch	2103
CD_2	antisym. stretch	2200
CD_3	antisym. stretch	2220

(b)

Table 2.1.: (a) IR characteristic frequencies of *n*-alkanethiols, according to [94] (vs: very strong, ms: medium strong, m: medium, w: weak), (b) frequencies of the CD stretching modes, according to [95].

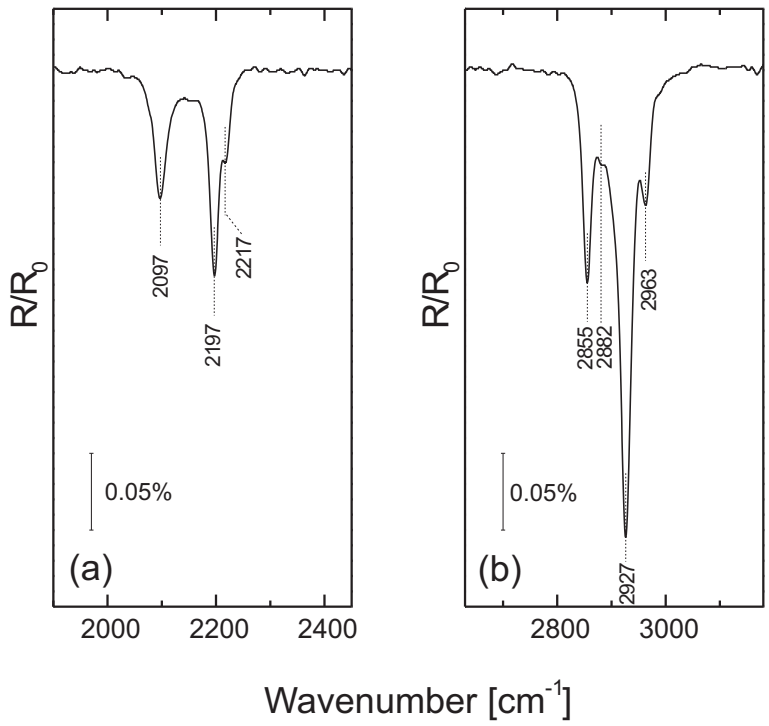

Figure 2.15.: IRRAS spectra ($\vartheta_i = 83°$, p-pol.) of (a) d-ODT monolayer, (b) ODT monolayer on 40 nm Au/1 nm Cr/Si. The reference of (a) was the sample of (b) and vice versa.

Vibrational modes of alkanethiols

Due to the structure of n-alkanethiols, their IR spectra are similar to the IR spectra of n-alkanes. A summary of vibrational modes is given in Tab. 2.1. In this thesis, the long-chained octadecanethiol (ODT, $C_{18}H_{37}SH$) was used as adsorbate molecule. Besides the advantage of an easy preparation of SAMs, the long chain also ensures a strong IR signal because of the high quantity of CH_2 groups. In several experiments of this thesis the use of deuterated ODT (d-ODT, $C_{18}D_{37}SH$) was preferred: because of the higher mass of the D atoms, the CD-stretching vibrations can be found at a lower wavenumber in a range between 2050 cm^{-1} and 2250 cm^{-1}, while there is no absorption in the range of the CH-stretching vibration. This makes d-ODT SAMs on Au a well suitable reference system for ODT SAMs on Au. In case of in-situ ATR-IR measurements, the use of d-ODT was preferred in order to separate the CD-stretching vibration peaks of the adsorbate from the CH-stretching vibration peaks from the surrounding solvent (ethanol). Fig. 2.15 shows IRRAS spectra of ODT and d-ODT in the range of the CH-stretch vibrations and CD-stretch vibrations, respectively.

2.9.2. Antibodies

Antibodies (also: immunoglobulin, Ig) are proteins, that are produced by an animal or human as a reaction to the presence of an external substance (antigen). Their function

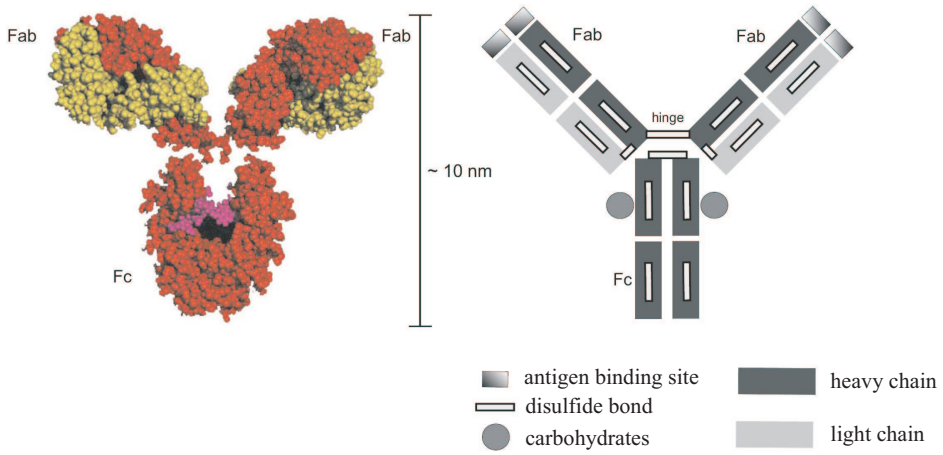

Figure 2.16.: Chemical structure of an antibody molecule according to [96] (left), and schematic composition (right). The antibody consists of two identical light and heavy polypeptide chains connected with disulfide bonds. The binding sites for antigens are at the end of the Fab fragments. Taken from [97].

band	vibration	band position [cm^{-1}]
amide I	C=O-stretch	1630-1680
amide II	CN-stretch, NH-bend	1515-1650
amide III	CN-bend, NH-bend	1200-1390
amide A	NH-stretch	3300

Table 2.2.: Selection of some IR characteristic frequencies of proteins [41, 99, 100]. There is no agreement about the exact origin of the amide III band in the literature.

is to disarm antigens and thus to protect the animal or human against infections and diseases. The basic structure of an antibody molecule is Y-shaped (Fig. 2.16) consisting of two identical heavy chains and two identical light chains connected by disulfide bonds. Antibodies have a specific high affinity for the antigen, that has caused their synthesis; the antigen is identified by a special group, the antigenic determinant (epitope). This group couples with a binding site of the antibodies according to the key-lock principle. The basic structure of an antibody has two binding sites, therefore two identical epitopes can be bound. If these two epitopes belong to different antigens, they are crosslinked [98]. Polysaccharides, nucleic acids and proteins (and therefore antibodies themselves) can act as antigens.

Extraction of antibodies Antibodies are attained by injecting a host animal A with antigens from a different animal B. As this procedure is repeated several times, the host animal develops specific antibodies against this antigen (A vs. B antibodies). After a certain time, these antibodies can be extracted from the serum of the host animal. Because most antigens have several different epitopes, antibodies extracted from the host animal are heterogeneous mixtures of antibodies, each being specific to one epitope. Such a mixture of antibodies is called polyclonal. Monoclonal antibodies on the other hand are specific to one epitope only; their synthesis is more complicated. The antibodies used in this theses were polyclonal antibodies. More information about the biological properties of antibodies can be found e. g. in [98].

Vibrational modes of proteins

The band positions of the most important IR active vibrations of proteins are shown in Tab. 2.2. In addition to these vibrational bands, the CH-stretching vibrations at $2840\,cm^{-1} - 2980\,cm^{-1}$ and the CH-bending vibrations at $1370\,cm^{-1} - 1470\,cm^{-1}$ can be detected in the spectra (see Tab. 2.1). [27, 99, 100]. It must be emphasized, that the

amide bands consist of several vibrational modes; only the most contributing are listed in Tab. 2.1. The shape and exact position of the bands depend on several factors such as the state of aggregation, concentration, sample preparation, and the type of amide (primary, secondary, tertiary) [41].

2.9.3. DNA

DNA (deoxyribonucleic acid) is a macromolecule containing the genetic information of all cellular forms of life. It is a linear polymer consisting of a backbone of sugar-phosphate units, to which different substituents are attached. The sugar units are deoxyribose, each connected with one of four possible bases: adenine (A), cytosine (B), guanine (G), thymine (T). The chemical structure of a DNA molecule containing the four different bases is shown in Fig. 2.17. The bases attached to the backbone form a sequence, which describes the genetic information and therefore the instruction for the reproduction of proteins.

While adenine has a tendency to couple with thymine, guanine couples with cytosine due to hydrogen bonds. Therefore, two complementary single DNA strands will combine, and the well known double helix structure is formed (Fig. 2.18). In this structure the backbones of each strand are on the outside of the helix running into opposite direction, while the base pairs are in the middle. The base pairs are coupled by weak

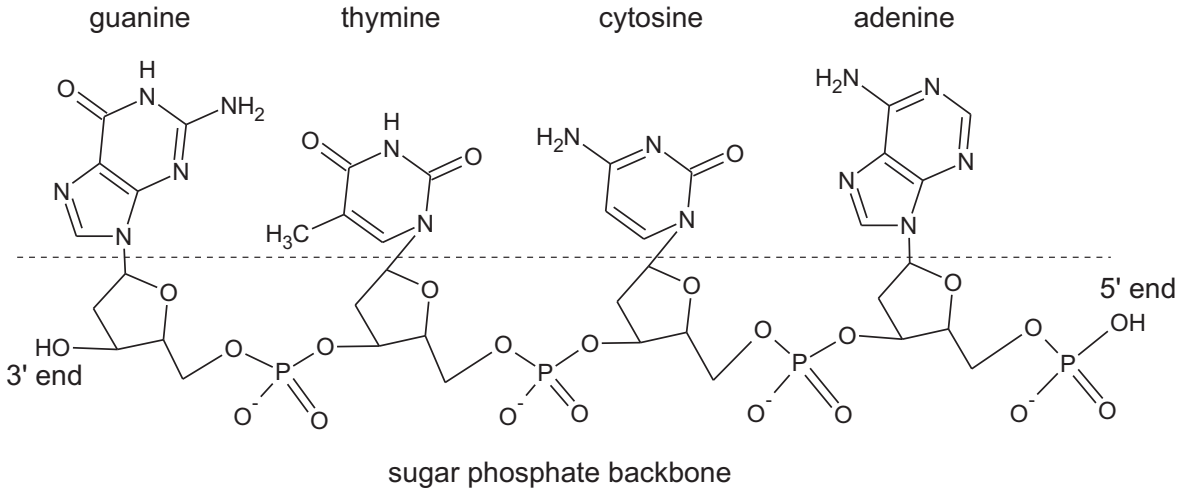

Figure 2.17.: Chemical structure of a DNA molecule with its four bases adenine, cytosine, guanine, and thymine.

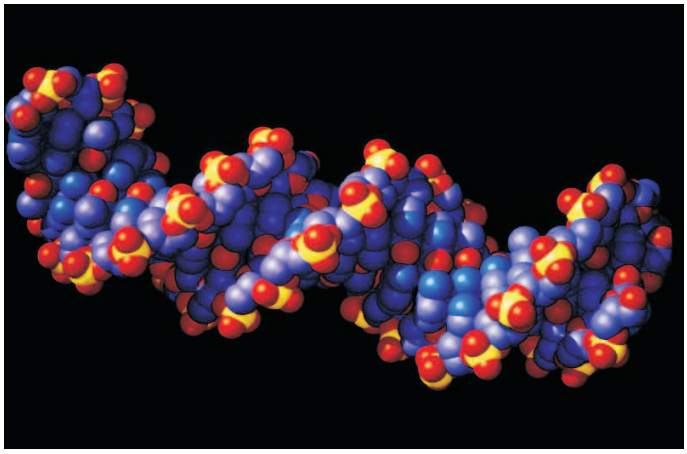

Figure 2.18: The double helix structure of DNA. Taken from [101].

hydrogen bonds, that can be released as a result of biochemical processes or external impact like e. g. temperature. For more information regarding to the biological functions of DNA, see e. g. [98].

Vibrational modes of DNA

Fig. 2.19 shows FTIR spectra of the nucleic acids adenine, cytosine, guanine, and thymine. Due to the complexity of the DNA structure the spectra consist of a large variety of absorption peaks, not only in the so-called fingerprint area below 1450 cm^{-1}, where e. g. vibrations of single bound C, N, and O atoms of organic molecules can be found, but also up to 1700 cm^{-1}, as well as in the range of CH-stretch, OH-stretch, and NH_2-stretch vibrations (2800 cm^{-1} −3300 cm^{-1}). More information about IR spectroscopy of nucleic acids and other biomolecules can be found e. g. in [99, 103, 104]. A detailed overview about IR bands of nucleic acids in solution is given in [105].

2.10. Adsorption kinetics – the Langmuir model

Random adsorption processes of molecules resulting in a monolayer have been found to be well described by a model, that was introduced by Langmuir [106]. This model assumes a maximum coverage of a monolayer, where each atom or molecule contacting the surface adsorbs, and no desorption takes place. According to Langmuir, such an adsorption process is characterized by [93]

$$\frac{d\Theta}{dt} \propto 1 - \Theta \ , \tag{2.67}$$

and has a time time dependent coverage

$$\Theta(t) = 1 - e^{-ck_{\mathrm{L}}t^a} \ , \tag{2.68}$$

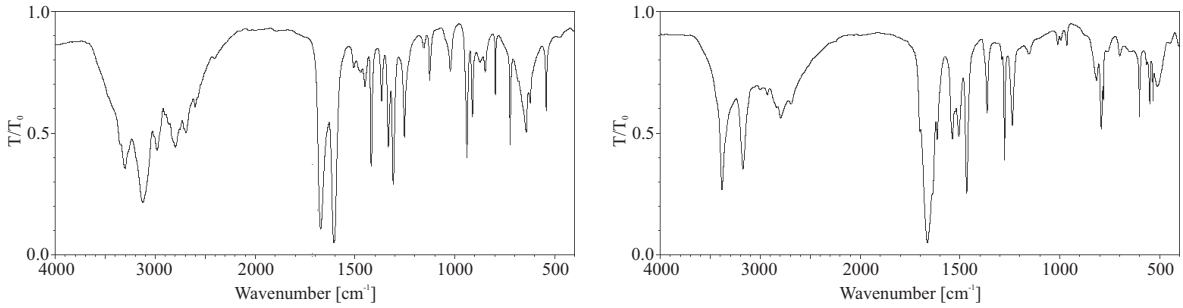

(a) adenine

(b) cytosine

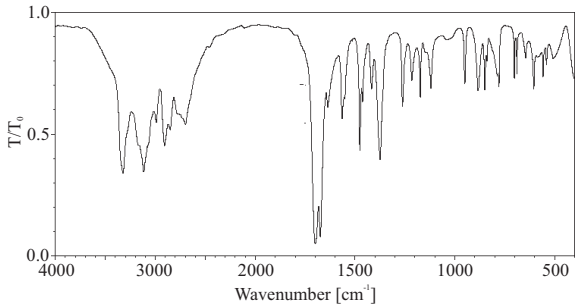

(c) guanine

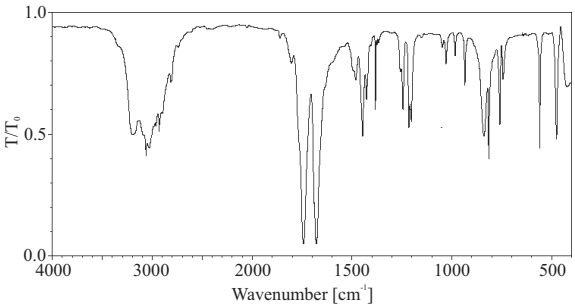

(d) thymine

Figure 2.19.: FTIR spectra of adenine, cytosine, guanine, and thymine, taken from [102].

where $a = 1$, c is the concentration in $\mathrm{mol\,l^{-1}}$, and k_L a rate constant in $\mathrm{l\,mol^{-1}\,s^{-1}}$. This model is known as the first-order Langmuir model. In the literature [93], it was shown, that the adsorption process of n-alkanethiols can principally be described by eq. (2.68) with $a = 1$. Adsorption processes that are controlled by diffusion have been found to be well described by eq. (2.68) with $a = \frac{1}{2}$ [107]. In [108] it is shown, that this diffusion limited first-order Langmuir model fits to the time dependent coverage of antibody-antigen coupling.

A second-order model for non-diffusion-limited adsorption processes is shown in [107], and given by

$$\frac{d\Theta}{dt} = k_\mathrm{so}[1-\Theta]^2 \ , \tag{2.69}$$

$$\Theta(t) = \Theta_0 \left[1 - \frac{1}{1+k_\mathrm{so}t}\right] \ . \tag{2.70}$$

Many models for adsorption kinetics exist; all being based on different assumptions, e. g. monolayer or multilayer growth, strength of binding energy, consideration of diffusion on the surface or desorption. Several models suited for monolayer adsorption are discussed in [93]; a model for multilayer growth was introduced in 1938 by Brunauer, Emmett and Teller (B. E. T. theory, [109, 110]).

When monitoring adsorption processes with in-situ IR spectroscopy, this is usually done by analyzing the time dependent peak area $A(t)$ of an absorption structure, or—if the peak shape does not change with increasing size—the time dependent peak height $h(t)$. The correlation between peak area (height, respectively) and surface coverage is assumed to be proportional

$$A(t) \propto \Theta(t) \ , \quad h(t) \propto \Theta(t) \ . \tag{2.71}$$

which is reasonable in the regime of monolayer coverage.

3. Equipment

3.1. The FTIR spectrometers

Bruker IFS 66v/S This evacuable FTIR spectrometer, which was used for the measurements at KIP in Heidelberg, is equipped with a set of transmission units and reflection units. It is controlled by the software "OPUS" [111]. All measurements were made using an MCT (mercury cadmium telluride) detector, which works at LN_2 temperature on the base of the internal photoelectric effect. MCT detectors do not work linearly, i. e. the sensitivity depends on the incoming radiant power. This non-linearity however is compensated by "OPUS". Measurements [112] have shown, that after cooling the detector and waiting for a stabilization period of about two hours, this detector works stable for about six hours. However, even during this time an approximately linear decrease of sensitivity may occur due to warming.

Thermo Nicolet Nexus 670 FT-IR This FTIR spectrometer was used for the experiments performed at NIMS in Tsukuba, Japan. The arrangement inside is very similar to the one of the Bruker IFS 66v/S; however, this spectrometer, that is controlled by the software "OMNIC" [113], is not evacuable, instead it is purged with a constant N_2 flow during the measurements. Because of the extraordinary high sensibility for concentration changes of polar gases, absorption bands of gaseous water and gaseous CO_2 can sometimes be seen in the spectra. The measurements on this spectrometer were also performed with an MCT detector.

3.1.1. Transmission- and reflection units

Multi sample transmission unit (for IFS 66v/S) This transmission unit—a self-construction of the group—allows the measurement of several samples without disrupting the vacuum of the spectrometer. The samples are moved by a manipulator, that can be operated from outside the spectrometer. It is possible to cool the samples with LN_2 during the measurement.

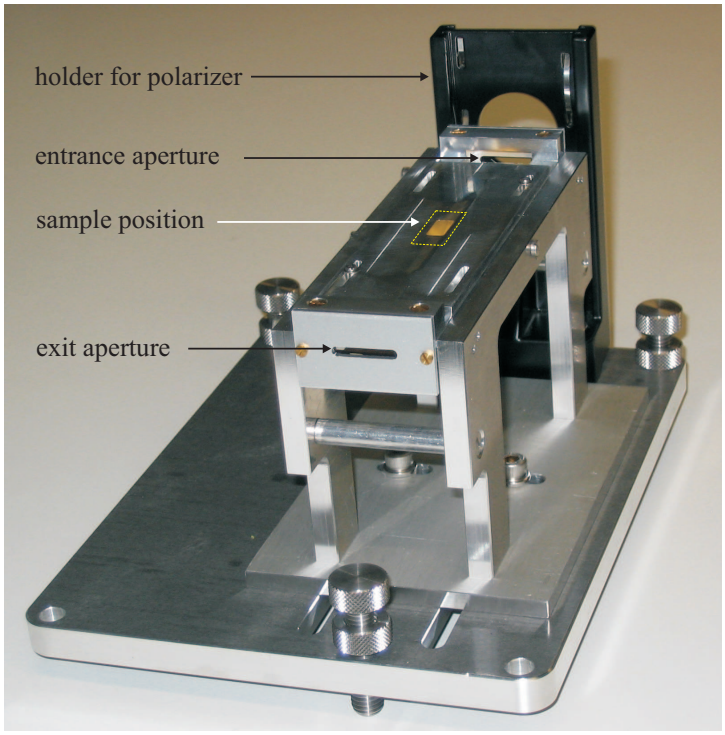

Figure 3.1.: IRRAS unit with a fixed angle of incidence $\vartheta_i = 83°$. After going through the entrance aperture, light hits a Au mirror, that reflects the beam onto the plane of the sample position. The sample reflects the light onto a second Au mirror, and the light leaves the IRRAS unit through the exit aperture to finally proceed to the detector. For more information, see text.

Reflection unit Bruker A 513 (for IFS 66v/S) This commercially available reflection unit allows the variation of the angle of incidence within a range $15° \leq \vartheta_i \leq 85°$. The angle of reflection can be changed by software control, i. e. no opening of the spectrometer and therefore disruption of the vacuum state is necessary. By a system of eight mirrors, the IR beam is deflected in a way, that it is focused on the sample position, and the reflected part finally hits the detector. To obtain a well defined polarization of the IR beam, it is possible to insert a polarizer. Both, focusing on the sample and polarization of the beam, are not influenced by changing the angle of reflection.

IRRAS unit (for IFS 66v/S) This reflection unit with a fixed angle of incidence $\vartheta_i = 83°$ (Fig. 3.1) has been constructed in the context of this thesis. The aim was to have a reflection unit, that is specially designed for measurements with grazing incidence. When using Bruker's A513 for measurements with grazing incidence, two disadvantages occur: (i) with increasing ϑ_i it becomes more difficult to align the mirrors properly; at

the same time, small alignment errors can have a fatal impact on the measured spectra. (ii) Also with increasing ϑ_i , the light spot at the reflecting plane becomes larger due to an increasing distortion. It becomes possible, that the dimensions of the spot are larger than the size of the sample; in this case, changing the samples between reference and sample measurement usually causes a strong effect on the baseline because of small differences between the reference and sample size.

These disadvantages have been eliminated in the construction of this IRRAS unit: (i) The IR beam is deflected slightly by just two plain Au mirrors. The mirrors are in a fixed position in the reflection unit, only the position of the complete IRRAS unit on the tripod baseplate is to be aligned. (ii) The samples are laid on the opening of the sample holder, with the side to be analysed facing down; the samples are required to cover the opening completely, therefore no alignment of the sample is necessary, and the lighted area of each sample is always the same. The IRRAS unit is constructed in a way, that IR radiation reflected by any other part besides the sample does not reach the detector; the intensity of scattered radiation at the detector is very small compared to the intensity of the radiation reflected by the sample.

Harrick Seagull (for Nexus 670 FT-IR) This commercially available reflection unit can be operated at different angles within a range $5^\circ \leq \vartheta_\mathrm{i} \leq 85^\circ$ without misaligning, defocusing or changing the polarization of the incident radiation.

3.1.2. ATR units

ATR flow cell (for Bruker 66v/S) This ATR unit (Fig. 3.2), which was constructed in the context of the preceded diploma thesis [40], is optimized for the ATR measurement of molecules on solid/liquid interfaces. It fits to Bruker's A513 and allows a variation of ϑ_i in the range $25^\circ \leq \vartheta_\mathrm{i} \leq 80^\circ$. The flow cell is connected to the outside of the spectrometer via air tight feed throughs, so its interior can be manipulated from outside without disrupting the vacuum state. The flow cell as well as the coating of the O-ring and the connectors are made out of teflon and therefore are very inert. The tube made out of PP is disposed after every experiment. To exclude any chance of contamination by the syringe or the valve, the syringe is mounted at the outflow of the cell and used to draw the liquid into the cell. The ATR crystal is a 25 mm diameter Si hemisphere (purchased at Mateck, Jülich) covered with a naturally grown oxide layer. Compared to differently shaped ATR crystals, a hemisphere has the advantage, that for all ϑ_i every light beam pointing to the center of the reflecting plane hits the spherical surface of the ATR crystal with normal incidence, and no refraction must be considered.

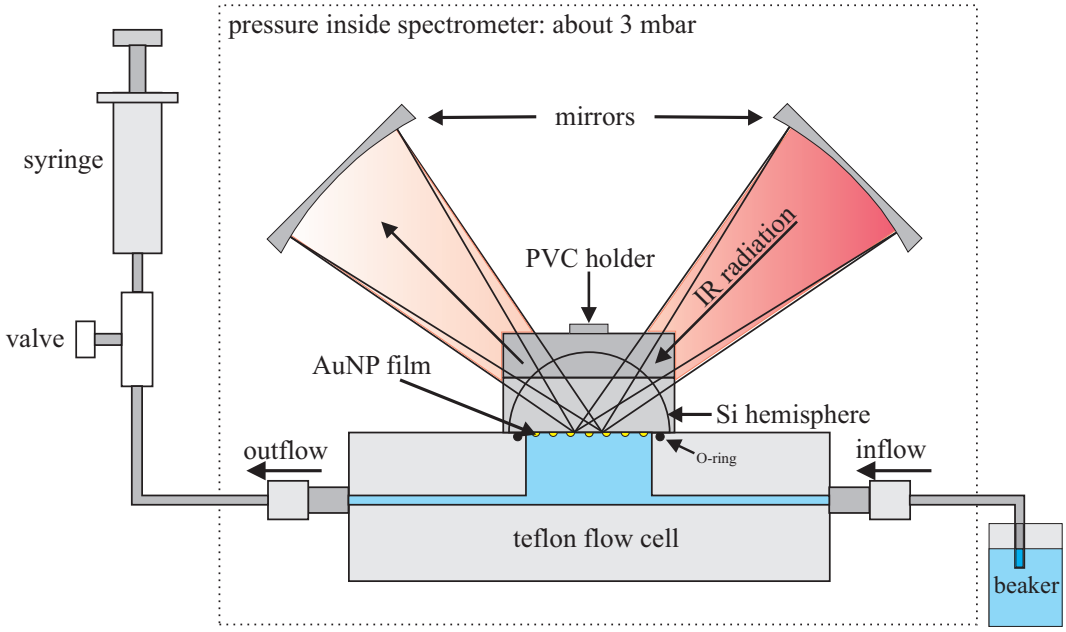

(a)

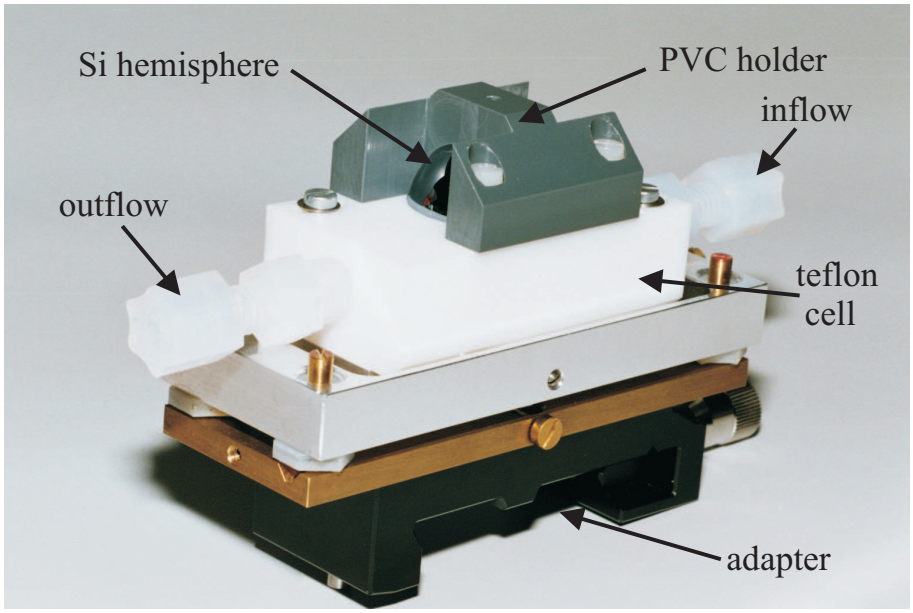

(b)

Figure 3.2.: Scheme (a) and photo (b) of the ATR unit.

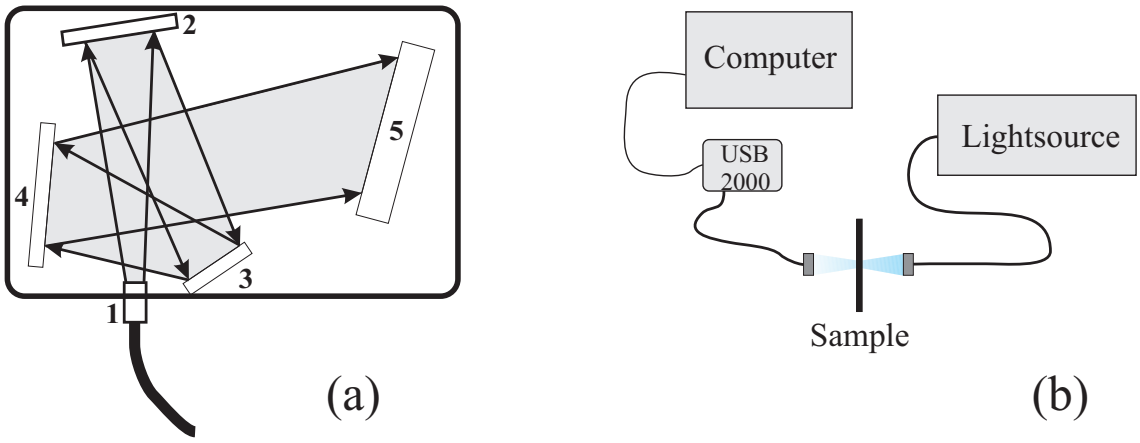

Figure 3.3.: (a) Scheme of the UV/VIS spectrometer "USB 2000": Light from the input fiber enters the optical bench through the connector (1), it then hits the collimating mirror (2), where it is focused onto the grating (3). The grating diffracts light from the collimating mirror and directs the diffracted light onto the focusing mirror (4), that finally focuses the light onto the CCD detector (5) [114].
(b) Scheme of the setup for UV/VIS transmission measurements: Light coming from a deuterium-halogen light source is directed to the sample through an optical fiber. Another fiber guides the transmitted light to the spectrometer, that is connected with a computer.

Seagull ATR kit (for Nexus 670 FT-IR) This ATR kit was purchased by Harrick as optional accessory of the Harrick Seagull reflection unit. Together with the provided flow cell it allows the measurement of molecules on solid/liquid interfaces with different ϑ_i. Like in case of the self designed ATR unit, the interior of the flow cell can be manipulated from outside using a disposable PP tube, that is air tightly fed into the spectrometer. The flow cell is made out of stainless steel, the material of the O-ring is Kalrez. The used ATR crystal was the same as used for the experiments with the self designed ATR flow cell.

3.2. The UV/VIS spectrometer

Ocean Optics USB 2000 The USB 2000 is a 190 g light pocket size dispersive UV/VIS spectrometer (Fig. 3.3a). The detector is a 2048-element linear Si CCD array ranging from $\lambda = 1100\,\text{nm} - 200\,\text{nm}$ ($\tilde{\nu} = 9000\,\text{cm}^{-1} - 50000\,\text{cm}^{-1}$) with a spectral resolution of 2 nm [114].

Fig. 3.3b shows a typical setup for UV/VIS measurements. The light source is a halogen deuterium lamp, that works on the shine through principle, i. e. the light coming from the halogen source is focused on a small diameter aperture in the deuterium bulb. This

source has a continuous spectrum in the requested range, which is overlaid by sharp lines at 656 nm (Balmer-α) and 486 nm (Balmer-β). Because the intensity of these lines usually saturates the CCD detector when measuring UV/VIS spectra, they may cause large artefacts in the relative spectra.

3.3. Scanning probe microscopes

3.3.1. Scanning force microscope (SFM)

The SFM images presented in this thesis were obtained using the multi mode instrument "MMAFM-2" by Digital Instruments. All measurements were performed ex-situ in air and at room temperature in tapping mode. The probes (Veeco, MPP-11100) were made of Si (P-doped) with a tip radius $r \approx 10\,\text{nm}$ and a resonance frequency $f_0 \approx 300\text{kHz}$. The basic principles about scanning force microscopy, that is also known as atomic force microscopy (AFM), can be found in [115, 116].

3.3.2. Scanning electron microscope (SEM)

Most SEM images presented in this thesis were measured at the Institute of Physical Chemistry of the University of Heidelberg using a Leo Gemini. They were performed ex-situ at room temperature at a pressure lower than $1 \cdot 10^{-5}\,\text{mbar}$. The electron beam was accelerated with a current of 10 kV. A good material contrast was obtained using the secondary electron detector. The SEM image shown in Fig. 5.3 was measured at NIMS in Tsukuba, Japan with a Hitachi S-4800. An introduction about SEM is given in [117].

4. VIS spectroscopy of Au nanoparticles – experiments and discussion

The optical properties of the wet chemically prepared AuNP were investigated with VIS spectroscopy. In addition to the measurements, VIS spectra were calculated assuming an effective medium model according to Maxwell Garnet and Bruggeman. This was done with AuNP dispersion for different concentrations (chap. 4.1) and for AuNP of different size, immobilized on glass substrates (chap. 4.2). In the latter case, the AuNP were hydroxylamine grown, therefore with increasing size the spherical shape of the particles was lost, as detected with SFM (see on page 55).

4.1. VIS spectroscopy of Au nanoparticles in suspension at different concentrations

The VIS transmission of spherical AuNP suspension was investigated. First, a reference spectrum with water in the plastic cuvette was obtained. The water was then replaced by as-prepared AuNP suspension of the concentration $c \approx 7.5 \cdot 10^{12} \frac{\text{nanoparticles}}{\text{ml}}$. After recording a spectrum, the concentration was stepwise reduced by replacing $\frac{1}{3}$ of the suspension with water; after each reduction step, one spectrum was recorded. Fig. 4.1 shows the obtained spectra; for concentrations greater than zero, they all have a minimum of transmission at 520 nm, however, as the concentration of AuNP in the suspension decreases, the transmission increases. As mentioned in chap. 2.6, the minimum of transmission is originated by a surface plasmon polariton resonance of the spherical AuNP. For filling fractions $f \ll 1$, the frequency of the absorption maximum should not depend on the concentration, since dipole-dipole interaction between particles do not occur. In accordance with this, the wavelength of minimal transmission does not change with the concentration.

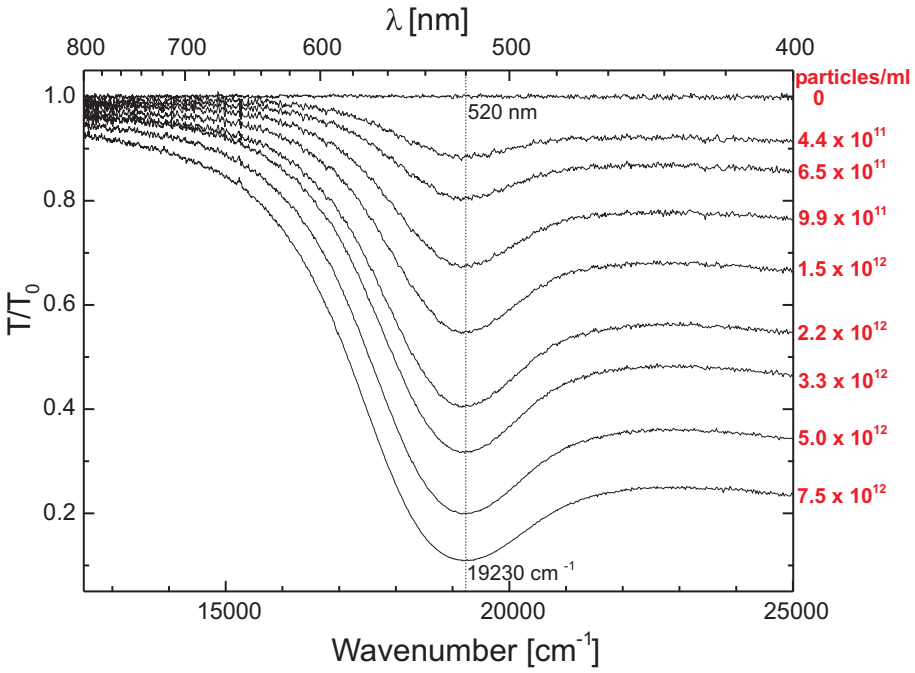

sample layer stack:	reference layer stack:
plastic cuvette	plastic cuvette
AuNP dispersion	water
plastic cuvette	plastic cuvette

Figure 4.1.: VIS transmission spectra (normal incidence) of suspension of spherical AuNP ($2R \approx 13\,\text{nm} \pm 2\,\text{nm}$, layer thickness $d = 4\,\text{mm}$). The reference spectrum was taken with water in the cuvette. The concentration of the suspension was stepwise reduced from $7.5 \times 10^{12} \frac{\text{particles}}{\text{ml}}$ to $4.4 \times 10^{11} \frac{\text{particles}}{\text{ml}}$.

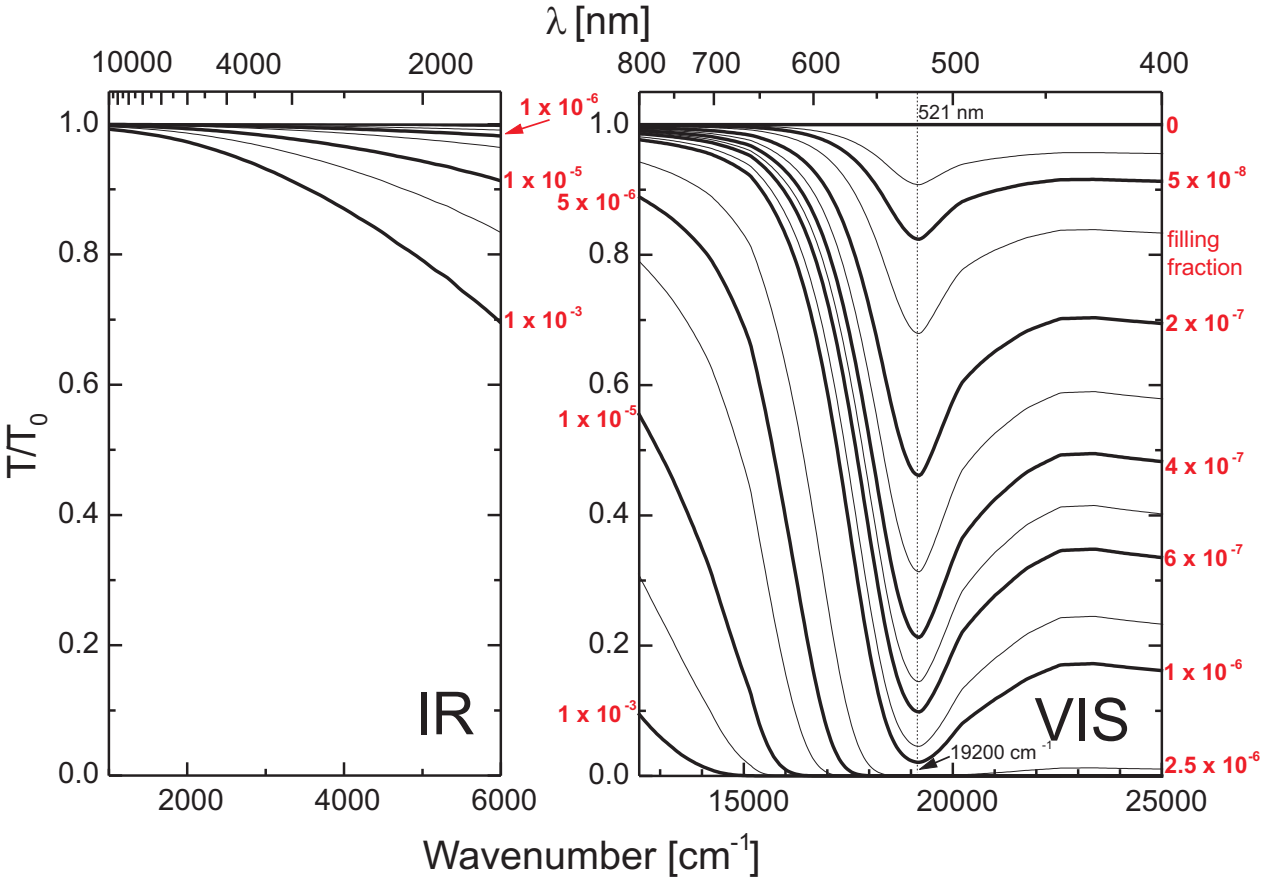

Figure 4.2.: Calculated transmission (normal incidence) of an 4 mm thick Maxwell-Garnett effective medium of AuNP surrounded by water with respect to the transmission of water. The spectra are calculated for the mid IR region (left) and for the visible region (right). The dielectric function of the AuNP is that of bulk gold (Fig. 2.10 on page 21), the dielectric function of the water was assumed to be constant with $\epsilon_1 = 1.8$, $\epsilon_2 = 0$, neglecting the vibrational modes of water in the IR. The red numbers show the volume fractions corresponding to the calculated spectra. The layer thickness of the sample and the reference is $d = 4\,\text{mm}$, surrounded by two half spaces of vacuum.

Comparison with calculation

The optical properties of AuNP suspension were simulated qualitatively using the effective medium model by J. C. Maxwell Garnett [68]. As mentioned in chap. 2.6.1, this model is valid for low filling fractions of metal particles in a surrounding matrix. The

calculation of the spectra, which are shown in Fig. 4.2, was done with the software "SCOUT" (see chap. 2.3) [43]. Spectra were calculated for the visible range as well as for the mid IR range. Qualitatively, the calculated spectra fit well to the measured ones in the visible range. All spectra show a strong absorption peak at 521 nm. With increasing volume fraction, the position of this peak does not change, however, the strength increases. For volume fractions $f > 1 \times 10^{-6}$ the absorption peak increasingly affects the blue range of the spectra, and finally completely absorbs radiation in the range below 550 nm for $f \geq 2.5 \times 10^{-6}$. When looking to the calculated IR spectra one finds a relative transmission close to unity for the same filling fraction. For a remarkable loss of transmission in the IR range, the filling fraction must be higher by at least one order of magnitude.

4.2. VIS spectroscopy of Au nanoparticles of different size

AuNP of different size, deposited on glass substrate were investigated with VIS spectroscopy in transmission and reflection geometry. The sample preparation was done as described in chap. 2.8.1 to 2.8.3: After AuNP of the as-prepared colloidal suspension were deposited onto the glass substrate, their size was increased by exposition to hydroxylamine/$AuCl_4$ aqueous solution. For the AuNP growth, the multi step method (see on page 31) was used. The number of growth cycles—each of them taking 2 min—was varied from 0 to 7. According to the preparation method, the samples had the following layer stack:

sample layer stack:	reference layer stack:
AuNP film	
APTES	
glass	glass
APTES	
AuNP film	

Transmission spectra of hydroxylamine grown AuNP

The relative transmission spectra are shown in Fig. 4.3 (top). The reference spectrum was measured with glass only. As can be seen, the relative transmission of the film of non-grown AuNP is qualitatively similar to the relative transmission of AuNP suspension, shown in Fig. 4.1: Red light is transmitted to a higher grade than blue light,

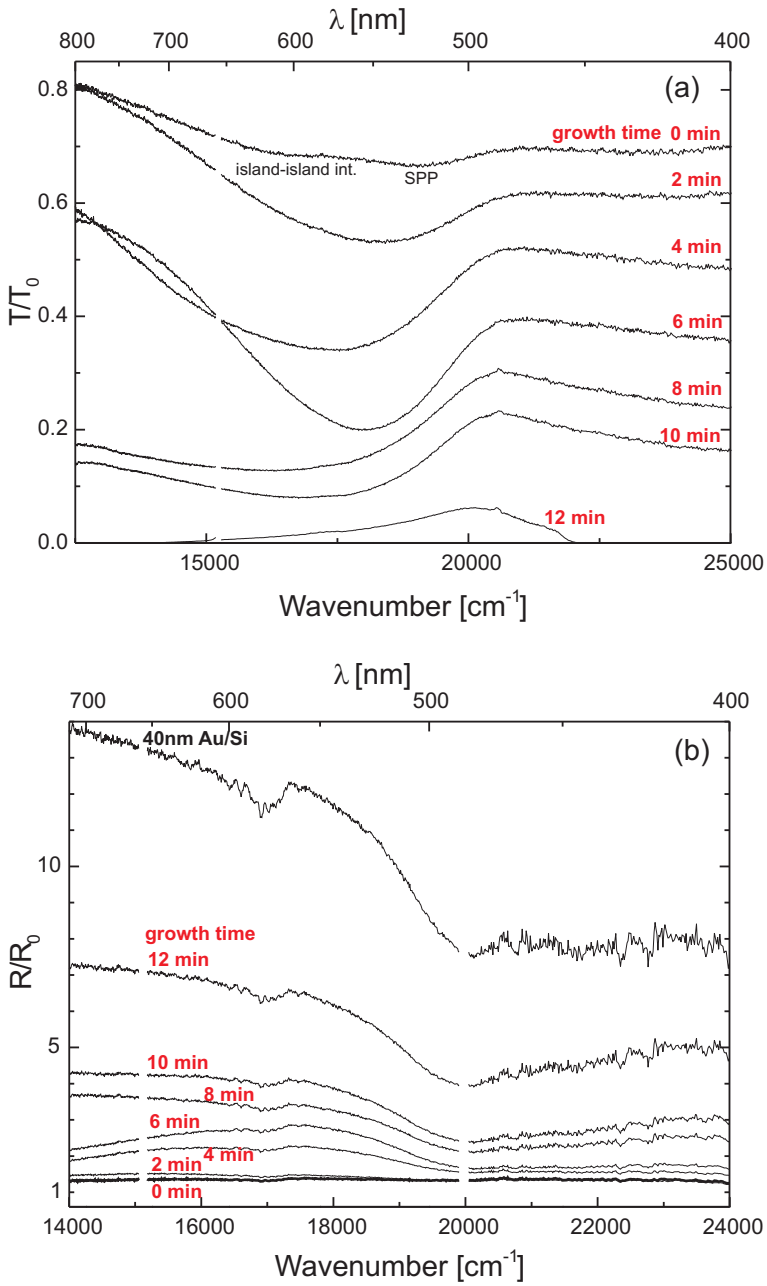

Figure 4.3.: (a) transmission spectra and (b) 45°-reflection spectra of enlarged AuNP on APTES modified glass. In addition, the reflection spectrum of a smooth 40 nm Au film is shown. The reference spectrum is taken from the transmission (reflection, respectively) of glass. The red numbers show the time of hydroxylamine growth, where 0 min means, that particles were not enlarged at all. Due to the large difference in intensities between reference and sample spectra in reflection, spectral features of the light source appear. The largest of those features—the Balmer α- and β-line at 656 nm and 486 nm—are eliminated.

and there is a surface plasmon polariton related minimum of transmission near 520 nm; the signal is too weak for a clear assignment to a wavelength. There is a second weak absorption signal near 600 nm, that can be assigned to interaction between particles, as for AuNP films deposited on a substrate dipole-dipole interactions between particles become non-negligible. As the AuNP become larger (and so does the filling fraction), the absorption structures overlap, become stronger and reach more and more into the near IR region. A maximum of transmission appears near 490 nm, however, the aggregate transmission decreases. Finally, the relative transmission of the film with a growth time of 12 min is very low.

Reflection spectra of hydroxylamine grown Au nanoparticles

The 45° relative reflection spectra are shown in Fig. 4.3 (bottom). The reference spectrum is the reflection of glass without AuNP. It can be seen, that the presence of non-enlarged AuNP on the glass surface causes a broadband increase of reflectivity by a factor of ≈ 1.3. If the particles are enlarged, the reflectivity is further increased. This is rather the case for light with $\lambda > 500$ nm, according to the optical properties of bulk Au, as discussed in chap. 2.6; with increasing particle size the typical yellow shine of bulk gold appears.

Comparison with calculation Using a 3D Bruggeman effective medium model (chap. 2.6.1) and the following layer stacks for sample and reference,

sample layer stack:	reference layer stack:
AuNP film (30 nm)	
glass (1 mm)	glass (1 mm)
AuNP film (30 nm)	

the relative transmission and reflection spectra of AuNP films in the mid IR and in the VIS range were calculated with the software "SCOUT" [43]. The change of AuNP size was considered by a variation of the filling fraction, ranging from 0.1 to 1. As can be seen in Fig. 4.4a and b, the calculated VIS spectra correspond to the measured ones (Fig. 4.3) in a qualitative way. The calculated IR spectra are shown in Fig. 4.4c and d.

It must be considered, that—as mentioned in chap. 2.6.1—the Bruggeman model becomes incorrect in the regime of high filling fractions, because for AuNP that are grown together the condition of a particles size small compared to the wavelength of light is

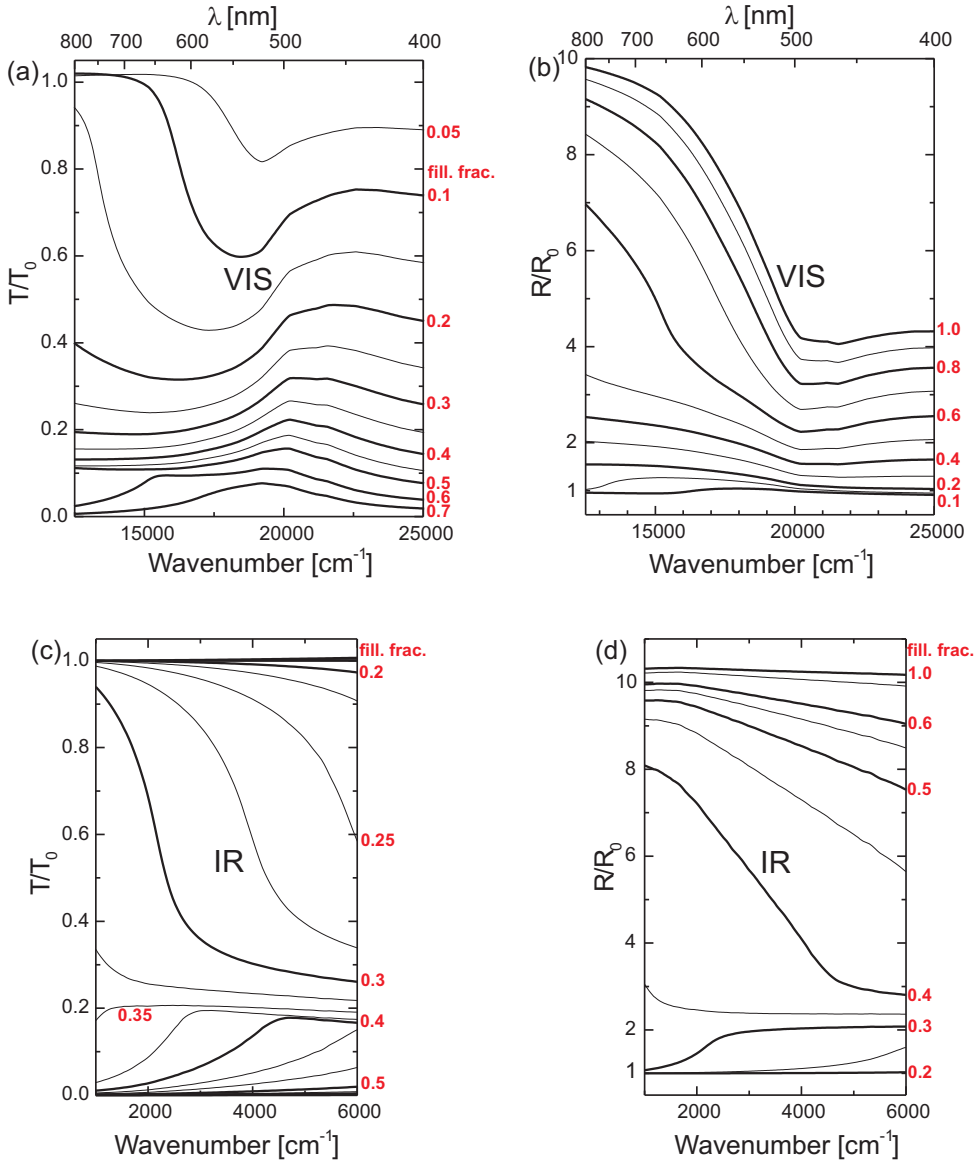

Figure 4.4.: Calculated normal incidence transmission spectra (a, c), and $\vartheta_i = 45°$ reflection spectra (b, d) of an effective medium according to the Bruggeman model with respect to the transmission/reflection of glass. The spectra are calculated for the visible region (top) and for the mid IR region (bottom). The dielectric function of the gold particles is described by that of bulk gold (Fig. 2.10 on page 21), the dielectric function of glass was assumed to be constant, $\epsilon_1 = 2.4$, $\epsilon_2 = 0$, neglecting any absorption bands in the IR. The red numbers show the volume fraction of each effective medium calculated.

not met any more. It is therefore not possible to describe the measured spectra quantitatively. One also has to keep in mind, that the calculations were done with the bulk Au dielectric function, as shown in Fig. 2.10, i. e. interband transitions are taken into account, but no intrinsic size effects. It was mentioned in chap. 2.6, that intrinsic size effects become important for AuNP having a size smaller than $R \leq 30\,\mathrm{nm}$ [64]. Therefore the neglect of intrinsic size effects may be another reason for discrepancies between measured spectra of small AuNP and the calculated spectra.

SFM analysis

The samples corresponding to the spectra shown in Fig. 4.3 were investigated with SFM; the images are shown in Fig. 4.5. One can see, that the particle size increases with the time of hydroxylamine growth. As the particle size becomes larger, particles seem to coagulate, loosing their spherical shape and their monodispersity. At the same time, a rearrangement of the AuNP takes place, leaving parts of the substrate uncovered. The biggest differences in morphology can be found for films (e) to (g): While the morphology of film (e) is still dominated by the shape of separate nanoparticles, in film (f) these are significantly larger and more coagulated. The area of bare substrate is significantly higher than in film (e). In film (g), the original shape of the nanoparticles cannot be seen any more; this film has obviously passed the percolation threshold. The film is conductive, but yet has trenches, that seem to reach down to the substrate.

In Tab. 4.1, quantitative data extracted from the images of films (e) to (g) are comprehended. The data are obtained using the SFM software "Nanoscope" [118]. In more detail, the software calculates the ratio of the surface above and beneath a manually entered threshold. For an adequate threshold (just above substrate height) from this follows the Au covered surface $\mathrm{A_{cov}}$. "Nanoscope" also calculates the total Au volume V_{Au} above the selected threshold, a 3D filling fraction ($\frac{V_{\mathrm{Au}}}{V_0}$), and the 3D surface of the sample (A_{surf}) by connecting neighboring points to triangles and adding up their areas. From these follow the values in Tab. 4.1, where A_0 is the scanned area and A_{Au}

film	$\frac{A_{\mathrm{cov}}}{A_0}$	$\frac{A_{\mathrm{surf}}}{A_0}$	$\frac{A_{\mathrm{Au}}}{A_0}$	$\frac{V_{\mathrm{Au}}}{V_0}$	d_{nom}[nm]
(e)	0.95	1.26	1.21	0.37	12
(f)	0.87	1.51	1.38	0.39	18
(g)	0.90	1.54	1.44	0.43	18

Table 4.1.: SFM analysis of the AuNP films shown in Fig. 4.5. The given quantities are A_{cov} : area covered by Au, A_0: scanned area, A_{surf}: total 3D surface area, A_{Au}: 3D surface area of the Au, V_{Au}: total volume of the Au, V_0: scanned area × maximum height of AuNP film, d_{nom}: nominal thickness of Au film. For more information, see text.

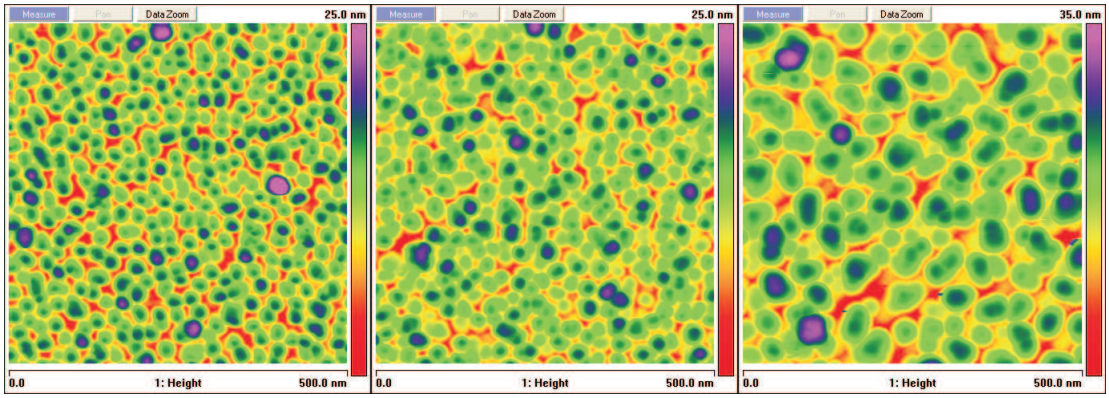

(a) 0 min. (b) 2 min. (c) 4 min.

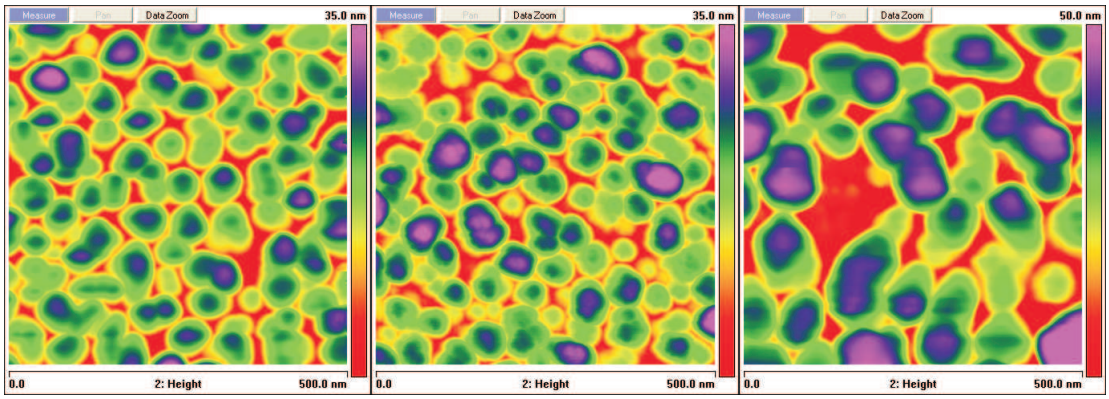

(d) 6 min. (e) 8 min. (f) 10 min.

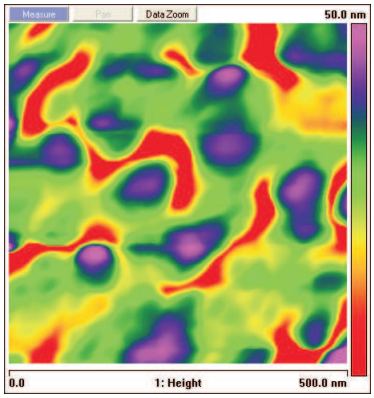

(g) 12 min.

Figure 4.5.: SFM images (500 nm ×500 nm) of hydroxylamine grown AuNP on the APTES treated glass surface. The time of hydroxylamine growing was varied in steps of 2 min from 0 min (a) to 12 min (g) and is given for each image. Please notice the different z-scale.

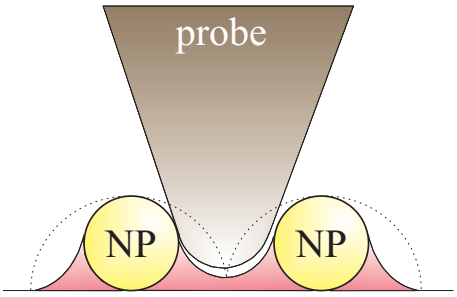

Figure 4.6: Simplified illustration of the effect of tip convolution in SFM measurements. The dashed line represents the measured height. The sperical particles are distorted in xy direction.

the 3D Au surface, i. e. A_{surf} minus the area of the bare substrate. The nominal film thickness (d_{nom})—i. e. the thickness of the AuNP film, if the particles were smeared over the substrate—is obtained by dividing the Au volume V_{Au} by the scanned area A_0.

Error consideration

Before discussing the values given in Tab. 4.1, some considerations about the errors should be made. There is an error occurring, when extracting the data out of the measured SFM images. This error is mainly influenced by manually determining the correct threshold level, and it affects all values in Tab. 4.1, since all are calculated on base of the threshold level. However, the most dominating error in this analysis occurs during the measurement of the SFM images: When analyzing structures like nanoparticles in the size regime of the SFM probe radius ($R \approx 10\,\mathrm{nm}$), the particle size in xy direction is strongly overestimated due to tip convolution. Fig. 4.6 illustrates the case of spherical particles in the same size regime as the tip. The resulting height profile is a convolution of the particle and the tip geometry. In the case shown in Fig. 4.6, the distance between the particles is too small for the probe to reach the substrate in between. The red space is out of reach for the SFM tip, therefore no information about this space can be obtained with this method, i. e. a sample consisting of the yellow spheres only and a different sample consisting of the yellow spheres and the red structures would give the exact same SFM image.

Because the discussed error, in Tab. 4.1 only films (e)-(g), that consist of larger structures, were taken into account; however, these values are still strongly affected by tip convolution and therefore must be considered as a rough estimation.

5. IR spectroscopy of adsorbates on Au nanoparticles – experiments and discussion

5.1. SEIRA on Au nanoparticles

Reversible adsorption of AuNP out of colloidal suspension on the APTES covered SiO_2/Si surface was investigated with in-situ ATR-IR spectroscopy. After a submonolayer of AuNP has formed on the surface, it was exposed to aqueous solution of aminoethanethiol (AET), causing a coverage of the AuNP by AET; this resulted in the desorption of the AuNP from the surface [119], as shown below in this chapter.

5.1.1. Adsorption of Au nanoparticles on SiO_2/Si surface monitored by in-situ ATR-IR spectroscopy

As mentioned in chap. 2.6, AuNP have a strong absorption band in the visible range due to surface plasmon polariton resonance; in the infrared no measurable plasmon polariton related signal is expected. Fig. 5.1 shows the spectral changes due to the exposition of the APTES coated SiO_2/Si surface to the AuNP suspension; the reference spectrum had been measured with water in the flow cell. The most dominant change is a broad increasing absorption signal at 3386 cm^{-1}, that can be assigned to the OH-stretching vibration of the surrounding water [120]: As the AuNP adsorb on the APTES coated SiO_2/Si surface, a film with a substantial degree of SEIRA activity is formed. This enhances the absorption signal from the water, resulting in the occurrence of this absorption peak directed towards lower relative reflection, because the absorption of the water is higher in the sample spectrum than in the reference spectrum.

Development of the vibrational spectra during adsorption process

The spectral changes in the range of the CH-stretching vibrations are shown in more detail in Fig. 5.1b. It can be seen, that three structures appear in the spectra during

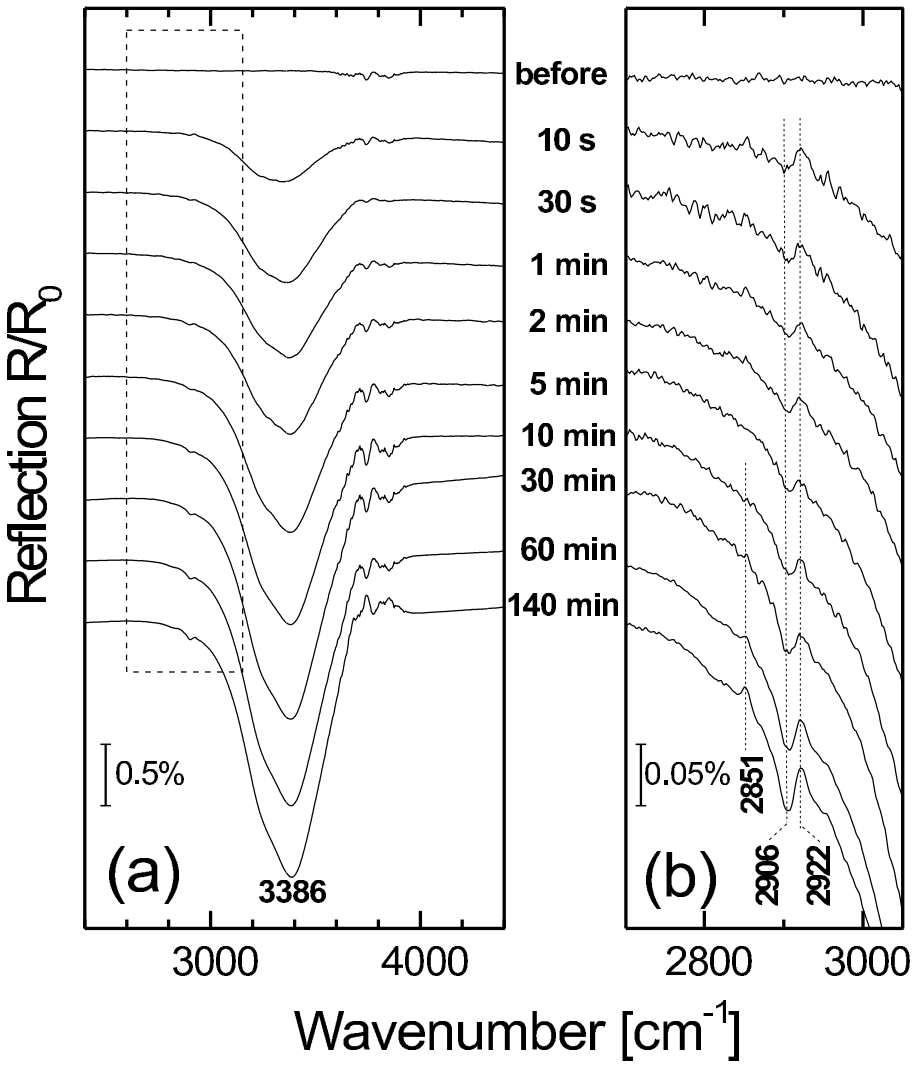

Figure 5.1.: In-situ ATR-IR spectra ($\vartheta_i = 45°$, p-pol.) of AuNP during adsorption on the APTES coated SiO_2/Si surface [119]. (a): overview, (b): magnification of the dashed frame shown in (a).
The reference spectrum was obtained with water in the flow cell contacting the SiO_2/Si surface. The spectra are vertically shifted against each other. For spectral explanations, see text.

the AuNP adsorption on the APTES coated SiO_2/Si (surface of the ATR crystal), the strongest being located at 2906 cm^{-1}. This signal can most possibly be assigned to the CH_2-stretching vibration of the sodium citrate that is covering the AuNP [121]. As more and more citrate covered AuNP adsorb on the SiO_2/Si surface, this vibration should become increasingly enhanced, synchronized with the enhancement of the OH peak of the water. However, the signal is too weak for a quantitative discussion. The two other peaks that are located at 2851 cm^{-1} and 2922 cm^{-1} are directed towards higher reflection and can presumably be assigned to a frequency shift of the $(CH_2)_3$ vibration of the APTES layer on the SiO_2/Si surface [121]. Although their exact interpretation remains open, their origin is likely due to changes of the environment of the APTES molecules since they interact with the sodium citrate layer covering the AuNP. Therefore, their peak heights are correlated to the AuNP coverage of the SiO_2/Si surface.

Adsorption kinetics of the AuNP

For monitoring the adsorption kinetics, the height h of the water's OH-stretching band at 3386 cm^{-1} was analysed, see Fig. 5.2. The coverage of the surface by AuNP was assumed to be linearly correlated to the height of the peak at 3386 cm^{-1} because of two reasons: (i) The shape of the peak does not change with increasing height, and (ii) the average distance between the AuNP (Fig. 5.3) is big enough to neglect dipole-dipole interaction between the particles, so that every additional AuNP contributes the same part in SEIRA enhancement. Fig. 5.2 shows the OH-stretching peak height vs. time, where $t = 0$ marks the time, when the exposure of the surface to AuNP suspension began. The relative peak height was calculated with

$$h = 100 \left[1 - \frac{(R/R_0)_{3386\,\mathrm{cm^{-1}}}}{(R/R_0)_{\mathrm{baseline}}} \right] \ , \tag{5.1}$$

where the baseline was interpolated linearly between 2600 cm^{-1} and 4000 cm^{-1}. The acquisition time of the spectra was adapted to better follow spectral changes, therefore the measured points are not equidistant on the time axis, and the size of the error bars changes according to the signal-to-noise ratio. According to the points calculated from the spectra, the main part of the adsorption process takes place within the first 20 min; saturation is obtained after about two hours.

The measured points were fitted with a first order Langmuir model (chap. 2.10), that describes a random adsorption process in the first monolayer. In this case, the time dependent coverage $\Theta(t)$ is given by eq. (2.68) and the peak height is

$$h(t) = b \cdot \Theta(t) - d \ , \tag{5.2}$$

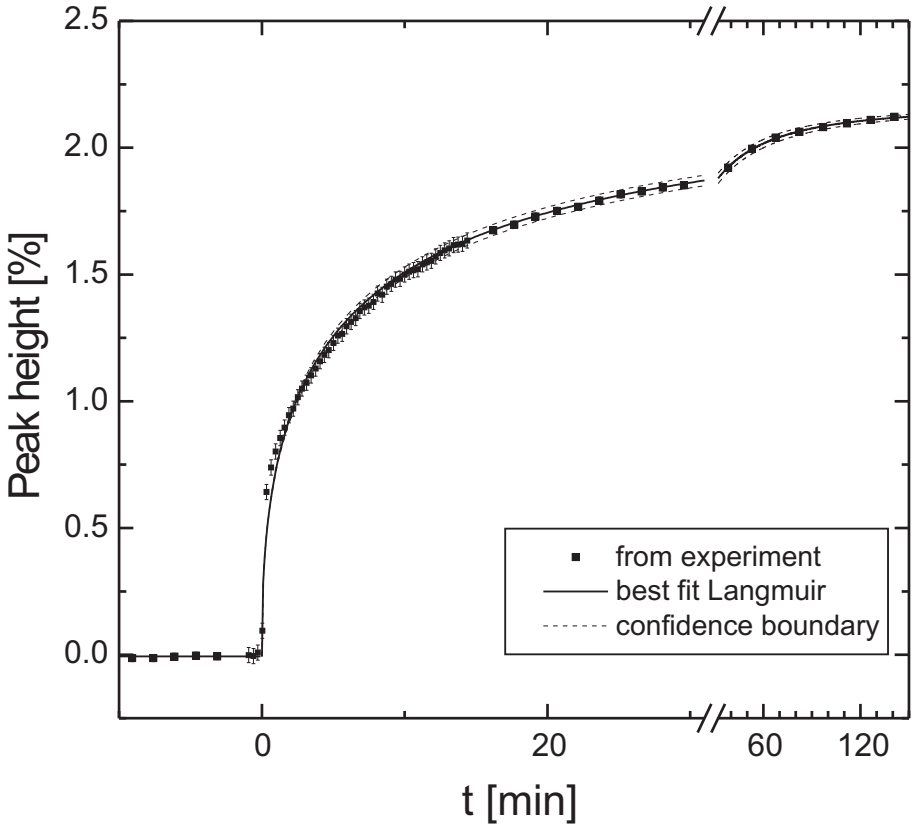

Figure 5.2.: Calculated height of the OH stretching vibration peak at 3386 cm^{-1} and first-order Langmuir fit of the peak size vs. time. The dashed lines are the confidence boundaries according to the standard deviations of the best fit parameters. The point of $t = 0$ marks the time, when AuNP entered the system. The kink in the curve is caused by the change of the time scale near $t = 30$ min. During the acquisition of the spectra the time resolution was adapted, causing a non-equidistance of the measured points on the time axis and a change of the size of the vertical error bars. For $t < -1$ min and $t > 18$ min the error bars are equal or smaller than the size of the points.

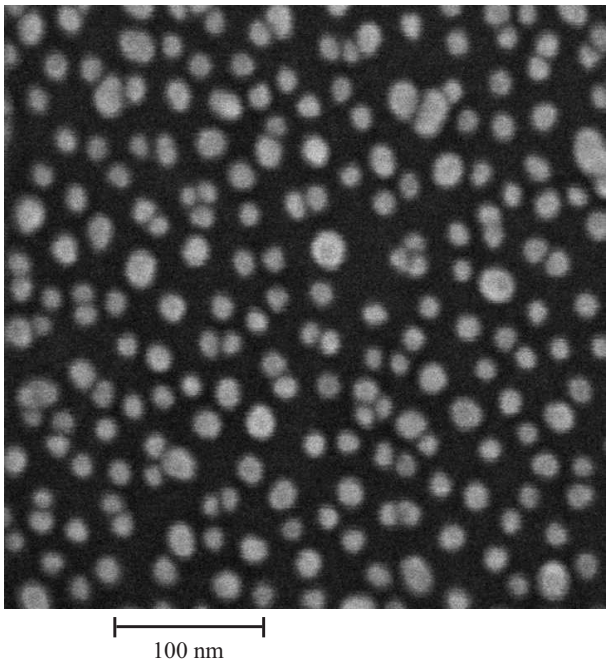

Figure 5.3: Ex-situ SEM image (400 nm × 400 nm) of AuNP on the APTES coated surface of a Si-ATR crystal after the AuNP adsorption has saturated [119].

where b is a scaling factor and d accounts for the baseline shifts including those due to possible instabilities during the measurement. When $d \ll b$, the fit parameter b is corresponding to the final peak height.

The time dependent peak height was fitted to eqs. (2.68) and (5.2) with b, ck_L, a, d being the fit parameters. In detail, the fit parameter d was obtained by averaging the measured points for $t < 0$, while the other fit parameters were obtained by fitting eqs. (2.68) and (5.2) to the measured points for $t > 0$. All points were weighed according to the number of scans of the corresponding spectrum. This procedure led to the following best fit parameters:

	best fit	σ
b	2.1613	0.0046
ck_L	$0.4186\,\mathrm{s}^{-1}$	$0.0048\,\mathrm{s}^{-1}$
a	0.4597	0.0052
d	6.41×10^{-3}	0.47×10^{-3}

The concentration was roughly estimated to be $c \approx 7.5 \times 10^{15} \frac{\text{particles}}{\text{l}}$. The fact, that the obtained fit parameter $a = 0.4597$ is close to $\frac{1}{2}$, suggests a diffusion limited adsorption process of the AuNP to the SiO_2/Si surface, where every particle, that makes contact to the surface, adsorbs [108]. A SEM image of AuNP on APTES treated Si-ATR crystal after the adsorption has saturated is shown in Fig. 5.3.

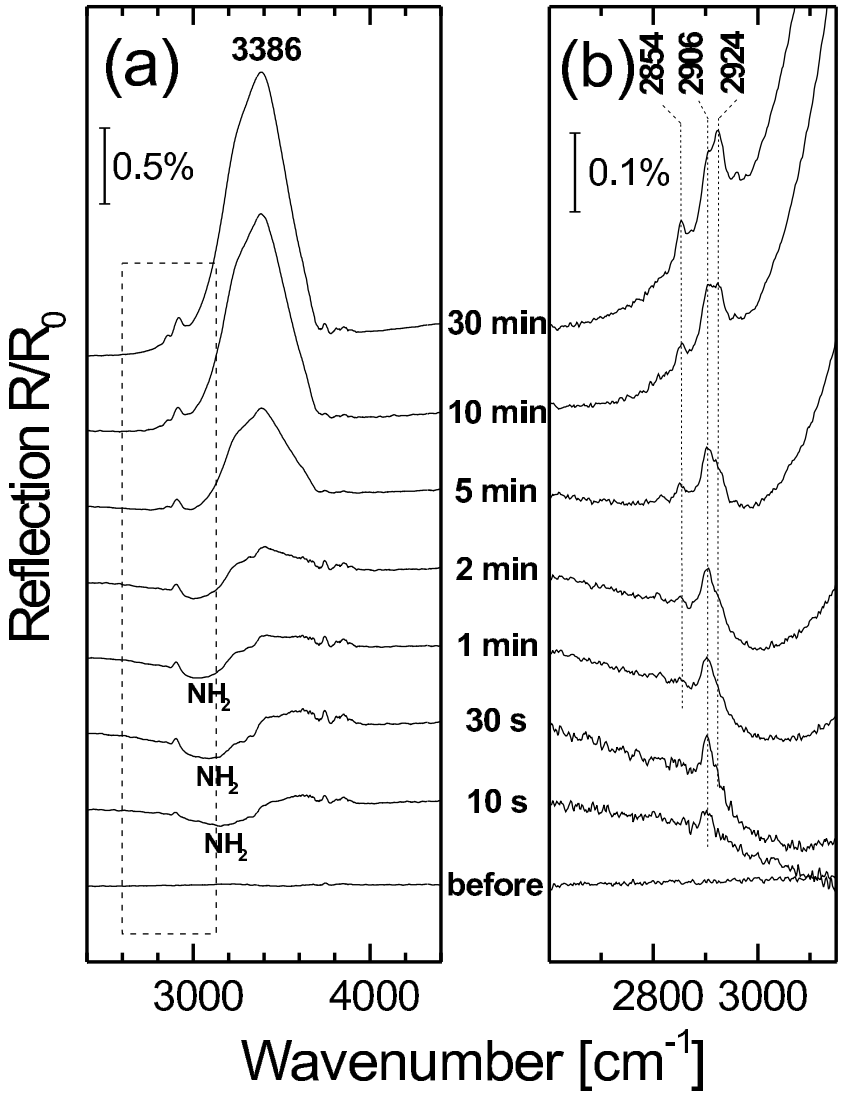

Figure 5.4.: In-situ ATR-IR spectra ($\vartheta_i = 45°$, p-pol.) of AET during adsorption on the AuNP on the APTES coated SiO_2/Si surface. The reference spectrum was taken with water in the flow cell contacting the AuNP submonolayer on the SiO_2/Si surface. The adsorption of the AET onto the AuNP causes the desorption of the AuNP from the surface. (a): overview, (b): magnification of the dashed frame shown in (a). The spectra are vertically shifted against each other. For spectral explanations, see text.

5.1.2. Adsorption of AET and desorption of Au nanoparticles monitored by in-situ ATR-IR spectroscopy

After the adsorption process described above was saturated, the flow cell was thoroughly purged with water in order to remove the AuNP suspension from the flow cell

and to ensure that only the surface bound AuNP remain. A new reference spectrum was taken of the remaining AuNP submonolayer on the ATR crystal with only water in the flow cell, then 20μM aqueous solution of AET (aminoethanethiol) were introduced into the flow cell while recording relative reflection spectra. As can be seen in Fig. 5.4a, soon after the AuNP submonolayer was exposed to AET solution, a broad band at 3386 cm^{-1} appeared, showing into direction of higher relative reflection. This means that with increasing time the absorption of radiation in this range is becoming smaller compared to the reference spectrum. In agreement with the AuNP adsorption experiment, the reason for that must be decreasing SEIRA activity of the surface, indicating a desorption process of the AuNP from the surface, as explained below.

Development of the vibrational spectra during desorption process

In Fig. 5.4a, the presence of the AET is indicated by the broad absorption of it's NH_2 group in the range between 3000 cm^{-1} and 3300 cm^{-1}. The appearance of this absorption signal is in good agreement with the behavior of the AET: In the early spectra just after the AET injection, the absorption peak appears very quickly, according to the fact, that AET adsorbs on the surface of the AuNP very quickly. With increasing time, the AuNP—now covered by AET—desorb from the surface, therefore the signal becomes weaker again. The exact position of the NH_2 peak of the AET is influenced by hydrogen bonding to the surrounding H_2O molecules. Fig. 5.4b depicts the spectral changes of the CH-stretching vibration during the AET adsorption and AuNP desorption. A closer view shows one structure at 2906 cm^{-1}, that appears very quickly after the start of the AET adsorption, and two structures at 2854 cm^{-1} and 2924 cm^{-1}, that appear relatively slowly. The quickly appearing signal at 2906 cm^{-1} can—with agreement to the spectra in Fig. 5.1b—be assigned to CH-stretching vibrations of the tri-sodium citrate. A signal showing towards higher relative reflection indicates the removal of absorbing matter between the measurements of the reference and the sample; therefore this signal strongly suggests the quick replacement of the citrate molecules by the AET molecules. This is due to the fact that the interaction between the positively charged APTES layer and the negatively charged citrate layer on the AuNP surface is only weak compared to the chemical bond formation of the thiol group to Au. The signals at 2854 cm^{-1} and at 2924 cm^{-1}, that occur slowly after the AET adsorption starts, can be assigned to CH-stretching vibration of the APTES layer [121]: They are directed towards higher relative reflection, because with desorption of the AuNP from the surface, the SEIRA activity becomes lower than it was in the reference system.

5.1.3. SEIRA of antibody-antigen coupling on Au nanoparticles in transmission spectroscopy

SEIRA active AuNP films were used for the ex-situ detection of specific antibody-antigen coupling by means of IR spectroscopy. The optical biosensor was a monolayer of goat vs. rabbit antibodies immobilized onto $2R \approx 13\,\mathrm{nm}$ AuNP/APTES/SiO_2/Si. The immobilization of the antibody monolayer was done according to a method that is introduced and explained in [97]. This method did not cause any significant change of the AuNP arrangement, as checked by SEM after the IR measurements. The non-specific antibody-antigen coupling was realized by exposing the samples to goat vs. mouse antibodies – where no coupling is expected in the ideal case. For specific antibody-antigen coupling, samples were exposed to rabbit vs. horse antibodies; in this case coupling of antibodies in solution to the immobilized antibody layer is expected to take place, and a second layer of antibodies is formed on top of the previously immobilized antibody layer. The exposition of the biosensor to antibody solution was realized by putting $25\,\mu$l of buffer solution onto the sensor film and then adding $25\,\mu$l of the as-purchased antibody solution. Finally, the drop was covered with an object slide, to realize the full coverage of the sensor film by antibody solution and also to prevent the liquid to dry off and leave an antibody multilayer. After the exposition time of one hour, the object slide was removed, and the sample was thoroughly rinsed with buffer solution to remove the excess amount of uncoupled antibodies. This preparation was done with SEIRA active AuNP films as well as with smooth films prepared by physical vapor deposition (40 nmAu/1 nmCr/SiO_2 /Si), that are known to be SEIRA inactive [40]. The set of the antibodies in this experiment is shown in Tab. 5.1.

Fig. 5.5a shows the IR transmission spectra (normal incidence) of antibody-antigen coupling on the SEIRA active AuNP film; the IRRAS spectra ($\vartheta_\mathrm{i} = 75°$, p-pol.) of antibody-antigen coupling on the SEIRA inactive 40 nm thick Au film are depicted in Fig. 5.5b. In both cases, the specific antibody-antigen coupling can clearly be detected by the appearance of characteristic absorption bands of proteins, the amide I band at $1645\,\mathrm{cm^{-1}} - 1661\,\mathrm{cm^{-1}}$, the amide II band at $1523\,\mathrm{cm^{-1}} - 1523\,\mathrm{cm^{-1}}$, the CH-stretching bands at $2850\,\mathrm{cm^{-1}} - 2963\,\mathrm{cm^{-1}}$ (clearly detected only in case of the SEIRA active AuNP film, Fig. 5.5a), and finally the broad amide A band near $3300\,\mathrm{cm^{-1}}$ (see Tab. 2.2). The

goat vs. rabbit	Dianova GmbH, #111-005-003
rabbit vs. horse	Dianova GmbH, #308-005-003
goat vs. mouse	Dianova GmbH, #115-005-003

Table 5.1.: Antibodies used for the detection of specific antibody-antigen coupling.

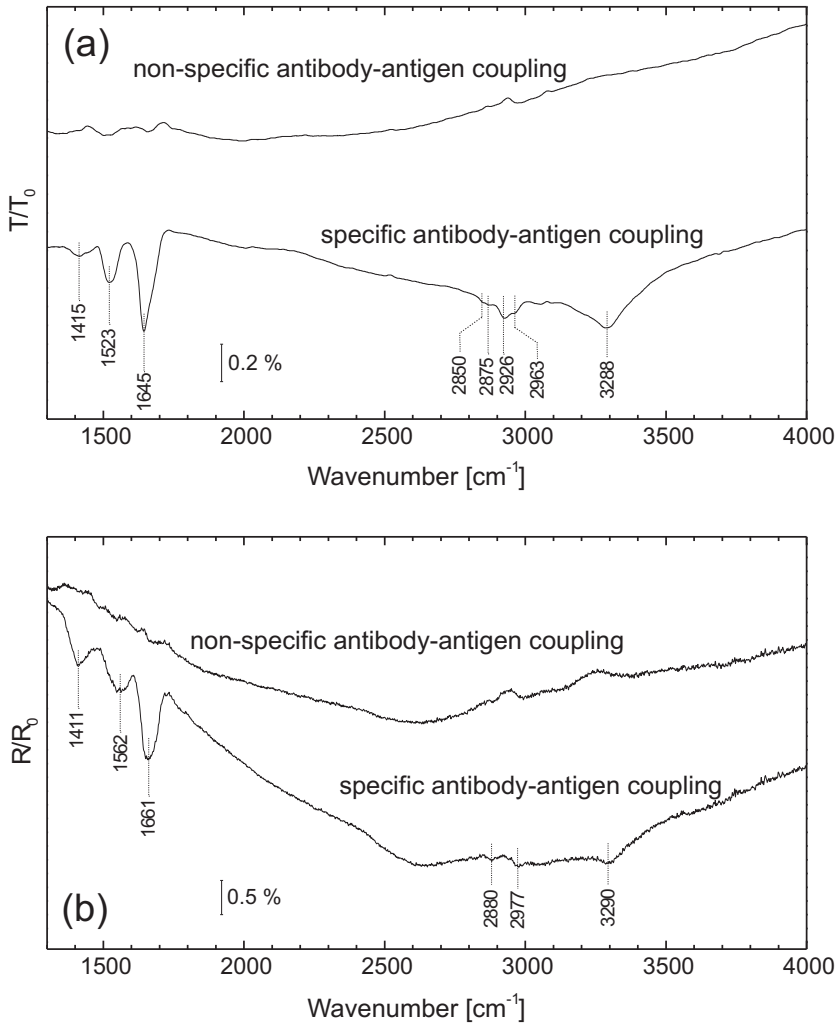

Figure 5.5.: (a) IR transmission spectra (normal incidence) of non-specific antibody-antigen coupling (top) and of specific antibody-antigen coupling (bottom). For both spectra, the reference system was a monolayer of goat vs. rabbit antibodies, immobilized on $2R \approx 13\,\mathrm{nm}$ AuNP/APTES/SiO_2/Si. The reference samples have then been exposed to non-specific antigens (goat vs. mouse antibodies), and with specific antigens (rabbit vs. horse antibodies), respectively.
(b) IRRAS spectra ($\vartheta_\mathrm{i} = 75°$, p-pol.) of non-specific antibody-antigen coupling (top) and of specific antibody-antigen coupling (bottom). For both spectra, the reference system was a monolayer of goat vs. rabbit antibodies, immobilized on 40nm Au/1nm Cr/SiO_2/Si. The Au film was prepared by physical vapor deposition and is considered as smooth and SEIRA inactive. The reference samples have then been exposed to non-specific antigens (goat vs. mouse antibodies), and with specific antigens (rabbit vs. horse antibodies), respectively.
For a scheme of the layer stacks, see Fig. 5.6. The spectra are vertically shifted. For spectral explanations, see text.

transmission (normal incidence):		IRRAS ($\vartheta_i = 75°$, p-pol.):	
sample:	reference:	sample:	reference:
spec. or non-spec. AB		spec. or non-spec. AB	
goat vs. rabbit AB	goat vs. rabbit AB	goat vs. rabbit AB	goat vs. rabbit AB
AuNP	AuNP	40 nm Au	40 nm Au
APTES	APTES	1 nm Cr	1 nm Cr
SiO_2/Si	SiO_2/Si	SiO_2/Si	SiO_2/Si

Figure 5.6.: Layer systems of the samples corresponding to the spectra shown in Fig. 5.5.

absorption band at 1411 cm^{-1}-1415 cm^{-1} can presumably be assigned to CH-bending vibrations of the CH_2 and CH_3 groups [27].

In case of non-specific antibody-antigen coupling, these characteristic bands do not occur, indicating that this kind of coupling does not take place in a significant quantity. However, there are small structures in the spectra at the relevant frequencies. To understand these structures, one has to keep in mind, that in these spectra the reference as well as the sample consisted of one monolayer of antibodies on the respective Au film (see Fig. 5.6); therefore in the single channel spectra (sample and reference), the characteristic absorption bands appear, and only in the ideal case they are canceled out completely in the relative spectra.

SEIRA enhancement factor of Au nanoparticles/APTES/SiO_2/Si film

The SEIRA enhancement factor of the AuNP/APTES/SiO_2/Si film is estimated by comparison of the spectra of specific antibody-antigen coupling shown in Fig. 5.5a and b. As an approximation, the height of the amide I band of both spectra is compared; it is $\frac{R}{R_0} \approx 1.2\%$ in case of the SEIRA non-active film, and $\frac{T}{T_0} \approx 0.5\%$ in case of the SEIRA active film. From eq. (2.29) follows for the approximate relative peak height of an adsorbate vibration on a transparent substrate in transmission geometry [3]

$$\frac{\Delta T}{T_0} \approx \frac{2\omega}{c(n_s + 1)} d_a \operatorname{Im} \epsilon_{a\parallel} \ , \tag{5.3}$$

where d_a is the layer thickness of the adsorbate and assuming a dielectric function of the adsorbate layer with negligibly small background polarization and weak oscillators, i. e. $\operatorname{Im} \epsilon_{a\perp,\parallel} \approx \operatorname{Im} -\frac{1}{\epsilon_{a\perp,\parallel}}$. With the same assumption, for an adsorbate layer on a

smooth metal surface in IRRAS geometry, the approximate relative peak height follows from eq. (2.30) and is given by [3]

$$\frac{\Delta R}{R_0} \approx 4d_\mathrm{a}\frac{\omega}{c}\cdot\frac{\sin^2\vartheta_\mathrm{i}}{\cos\vartheta_\mathrm{i}}\,\mathrm{Im}\,\epsilon_{\mathrm{a}\perp} \quad . \tag{5.4}$$

Finally it is assumed that $\epsilon_{\mathrm{a}\parallel}$ measured in transmission corresponds to $\epsilon_{\mathrm{a}\perp}$ measured in IRRAS, because the oscillating dipoles should have the same orientation relating to the Au surface; this Au surface is parallel to the substrate in IRRAS and mostly normal to the surface in SEIRA transmission, as most SEIRA enhancement comes from molecules on the sidewalls [3]. Therefore follows from eqs. (5.3) and (5.4) the ratio

$$\frac{\Delta R/R_0}{\Delta T/T_0} = 2(n_\mathrm{s}+1)\frac{\sin^2\vartheta_\mathrm{i}}{\cos\vartheta_\mathrm{i}} \tag{5.5}$$

between the IRRAS intensity and the one of a hypothetic relative transmission spectrum at normal incidence without metal islands, but with the adsorbate on the transparent substrate [3]. Taking into account

$$n_\mathrm{substr} = 3.4\,;\ \vartheta_\mathrm{i} = 75^\circ\,;\ \frac{\Delta R}{R_0} = 1.2\% \quad ,$$

and finally assuming a surface coverage ratio of $\frac{C_{\text{AuNP film}}}{C_{\text{smooth film}}} = 0.5$ (this is the result of considering the low coverage of the SiO_2/Si surface by AuNP, where the AuNP surface is estimated to consist of hemispheres, see Fig. 5.3 on page 61), one would expect to see an absorption peak in transmission as high as $\frac{\Delta T}{T_0} = 0.019\%$. In fact, the height of the absorption peak in transmission is $\frac{\Delta T}{T_0} = 0.5\%$; from that it follows a SEIRA factor of about 26 for this not yet SEIRA optimized morphology.

5.2. SEIRA on hydroxylamine grown Au nanoparticles

In the previous chapter SEIRA active Au films were prepared by deposition of AuNP on the APTES treated SiO_2/Si surface. As can be seen in Fig. 5.3, this leads to a submonolayer coverage of the surface by AuNP. However, it was mentioned before, that highest SEIRA activity is expected for densely packed but yet separate metal islands [6, 7, 8], therefore one would expect a significant increase of the SEIRA activity, if the size AuNP on the surface became enlarged and the average distance decreased. The method of hydroxylamine growth offers a possibility to increase the size of the AuNP;

in more detail, the presence of a Au surface enables hydroxylamine to reduce $AuCl_4$ to bulk Au, that grows on the surface; nucleation of new particles does not take place (see chap. 2.8.3). In the following chapters, hydroxylamine growth of AuNP was used to increase the SEIRA enhancement of the Au film.

5.2.1. SEIRA of ODT on Au nanoparticle films

SEIRA of an ODT monolayer on hydroxylamine grown AuNP films on SiO_2/Si substrate was investigated with ex-situ IRRAS ($\vartheta_i = 60°$, p-pol.) and IR transmission spectroscopy (normal incidence). For the growth of the AuNP, the single step method (chap. 2.8.3) was applied. After the growth process was completed, the samples were exposed to 1 mM solution of ODT in ethanol over night, where a self assembling monolayer was formed on the Au surface.

5.2.1.1. Variation of Au nanoparticle growth time

The AuNP films were prepared in the following way: (i) deposition of AuNP onto the APTES treated SiO_2/Si surface (deposition time: 3 h), (ii) hydroxylamine growth of the deposited AuNP using the single step method (see chap. 2.8.3). The time of hydroxylamine growth of the AuNP was varied for the different samples from 2:30 min to 5:00 min in steps of 30 s. First, the reflection spectra were taken, then the same set of samples was measured in transmission geometry. In case of the transmission spectra, the reference was the transmission of vacuum; for the reflection spectra, the reflection of a SiO_2/Si wafer was the reference. Fig. 5.7 shows the region of the CH-stretching vibrations between 2840 cm^{-1} and 2980 cm^{-1}, where the peaks can be assigned to the vibrations of the methyl and methylene groups the following way (see Tab. 2.1 on page 33):

2849 cm^{-1}	sym. CH_2
2870 cm^{-1}	sym. CH_3
2917 cm^{-1}	antisym. CH_2
2959 cm^{-1}	antisym. CH_3

While three of these vibrational modes can clearly be assigned to absorption peaks in the spectra, the peak of the symmetric CH_3-stretching vibration is only very weak. There seems to be no clear correlation between growth time and SEIRA activity, however, the most intense absorption structures can be found in transmission for the 5 min grown film, and in reflection for the 4:30 min grown film. The effect of absorption peaks

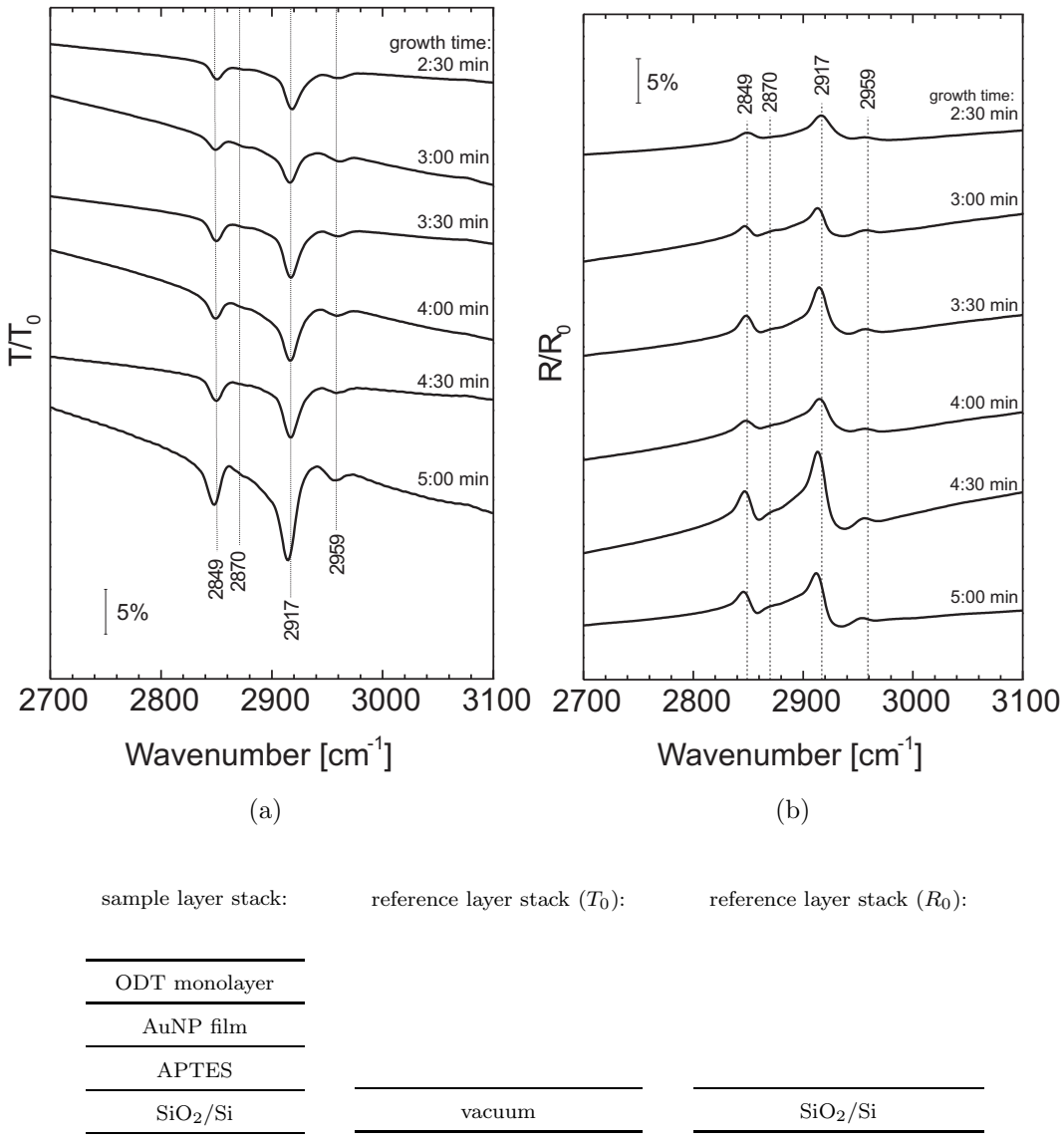

Figure 5.7.: (a) IR transmission (normal incidence) and (b) reflection ($\vartheta_i = 60°$, p-pol.) spectra of an ODT SAM on hydroxylamine grown AuNP films on APTES/SiO_2/Si. Both measurements were performed with the same set of samples. As reference, the transmission of vacuum (a) and the reflection of SiO_2/Si wafer (b) were measured. The spectra are normalized and vertically shifted.

in IRRAS spectra showing to the direction of higher relative reflection is known [122] and has been observed before [28, 40]. More on this will follow in chap. 5.2.1.2.

It must be noted, that the samples of the spectra in Fig. 5.7 do not only show the absorption features originating from the ODT monolayer, but also from the AuNP film, the APTES layer, and the SiO_2/Si wafer; this is, because the reference was measured with vacuum (transmission) and a SiO_2/Si wafer (IRRAS), respectively. Because Si wafers show no absorption structures in the respective range (see Fig. B.1), and also no plasmon polariton related signal of the AuNP film is expected in that range (see chap. 2.6), these layers should only influence the baseline of the spectra, but not be associated with absorption signals. However, the APTES molecules also consist of CH_2 and CH_3 groups (see Fig. 2.13 on page 30), therefore APTES gives a contribution to the absorption peaks of the spectra shown in Fig. 5.7. The ratio between APTES and ODT concerning the number of CH_2 groups is 6:17. Because of the different mechanisms contributing to SEIRA—the electromagnetic effect and the chemical effect—it is not possible to derive out of that the same ratio between APTES and ODT concerning the total peak strength of the CH_2-stretch vibrations at 2849 cm^{-1} and 2917 cm^{-1}. Measurements [123], where d-ODT/AuNP/APTES/SiO_2/Si and ODT/AuNP/APTES/SiO_2/Si were both measured vs. SiO_2/Si suggest, that the contribution of the APTES to the total CH_2-stretch signal is less than 7%.

To escape from this problem, in chap. 5.2.2 deuterated ODT with its characteristic CD-stretching vibrational bands in the 2050 cm^{-1} −2250 cm^{-1} range was used as adsorbate.

SEIRA enhancement factor

An estimation of the SEIRA enhancement factor was done by comparing the height of the CH_2-antisymmetric-stretch peak of the spectra shown in Fig. 5.7 to the height of the corresponding peak of a ODT spectrum on a smooth SEIRA inactive film, depicted in Fig. 2.15b on page 34. For this estimation, the 5 min grown AuNP film measured in transmission geometry (Fig. 5.7a) is considered. Using eq. (5.5) and taking into account

$$n_{\mathrm{substr}} = 3.4\,;\ \vartheta_{\mathrm{i}} = 83^{\circ}\,;\ \frac{\Delta R}{R_0} = 0.34\%\ ,$$

one would expect to see an absorption peak in transmission of the height $\frac{\Delta T}{T_0} = 0.0048\%$. In fact, the height of the absorption peak in transmission is $\frac{\Delta T}{T_0} \approx 10\%$; if the strength of the absorption peak in Fig. 5.7a is assumed to consist of a 7% contribution of the APTES layer as discussed before, a SEIRA factor of about 2000 follows as a very rough estimation. Compared to the SEIRA factor of 26 of the non-grown AuNP, the growth has—as expected—led to a morphology, that is much more SEIRA active.

In this estimation of the SEIRA factor, the area with adsorbates that contribute to the signal in the spectra was assumed to be equal. As suggested by SFM (see Tabs. 4.1 and 5.2 on page 54 and 79), the surface of the Au islands is larger compared to the flat area by a factor of roughly 1.3. Knowing, that only the adsorbate on the sidewalls significantly contribute to the signal in the SEIRA spectra, one can assume, that the area with adsorbate contributing to the signal is smaller for SEIRA active film, than for flat films. This would mean, that the real SEIRA factors are higher than the estimated ones.

SEM analysis

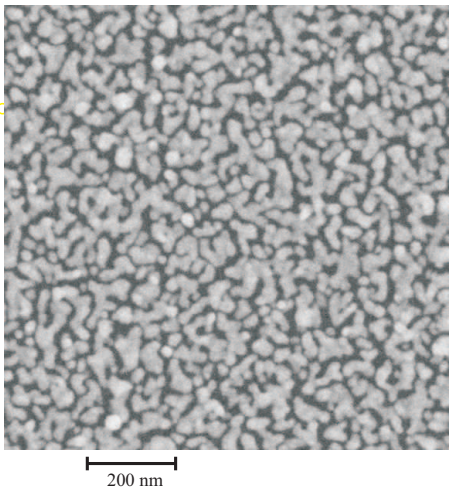

(a) 2:30 min

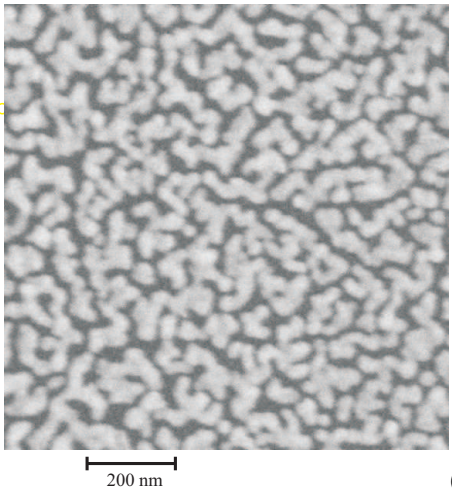

(b) 3:00 min

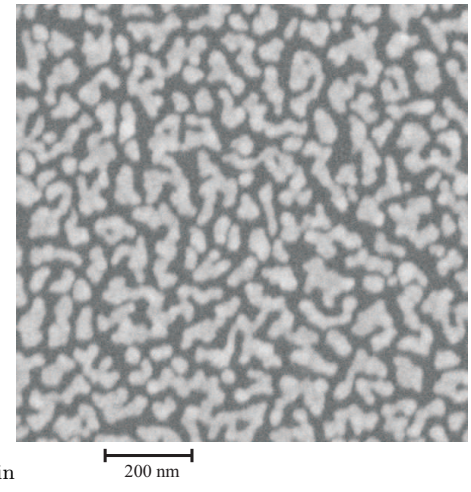

(c) 3:30 min

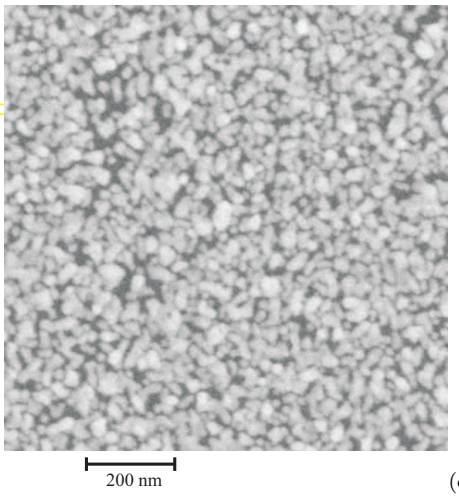

(d) 4:00 min

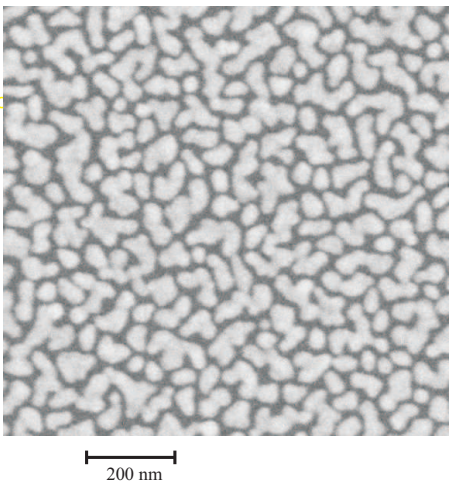

(e) 4:30 min

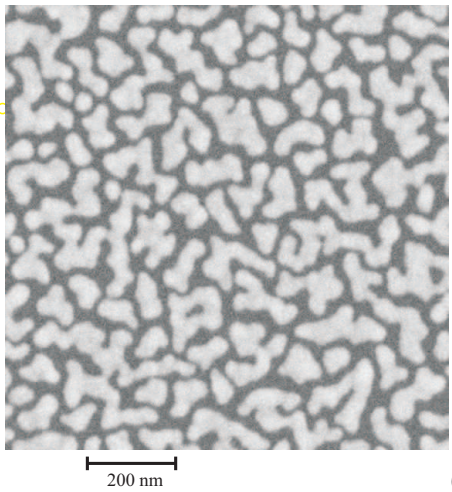

(f) 5:00 min

Figure 5.8.: (on page 72) Ex-situ SEM images ($1\,\mu m \times 1\,\mu m$) of hydroxylamine grown AuNP/APTES/SiO_2/Si. The bright structures mark the Au, while the dark background is the substrate. The deposition time of AuNP on the APTES treated SiO_2/Si samples was 3 h. The time of the hydroxylamine growth procedure was different for each sample and is given at the bottom of each image.

After measuring the IR spectra shown in Fig. 5.7, the morphology of the hydroxylamine grown AuNP films was investigated with SEM. The resulting images are shown in Fig. 5.8. The images show a material contrast, where the bright structures are Au and the dark background is the substrate. The 2D surface coverage $\frac{A_{cov}}{A_0}$ of the substrate by Au was calculated with the software "ImageJ":

film	(a)	(b)	(c)	(d)	(e)	(f)
$\frac{A_{cov}}{A_0}$	0.67	0.64	0.51	0.71	0.62	0.55

An error of ± 0.03 is estimated. Qualitatively, film (a) consists of partially very small islands; some of them still have a circular outline indicating, that these islands might still have their original spherical shape. Other islands have a large and rather branched structure. The surface coverage by Au is relatively high. Film (b) hardly shows any more circular shaped objects, the branched islands are broader than the ones in film (a). Film (c) has a significant lower surface coverage than the other films; it consists of islands that are mainly not as broadly branched as the ones in film (b). Film (d) has a very atypical morphology compared to all the others. It consists of very small particles, that are very densely packed resulting in the highest surface coverage of all films. It must be assumed that the morphology of this film was influenced by irregularities during the preparation process. Finally, films (e) and (f) both consist of rather compact and clearly separated islands, some of them widely branched. The 2D surface coverage of film (e) is significantly higher than the one of film (f), as the average distance between the islands is smaller. While film (e) is the one with the most intense absorption structures in reflection, film (f) is the one with the highest SEIRA activity in transmission.

Concerning the 2D surface coverage by Au, there is no clear trend observable for the films shown in Fig. 5.8. This suggests that in this regime of growth, vertical growth is preferred to lateral growth, therefore the islands become higher, but do not tend to grow laterally and percolate. However, this behavior may certainly change with increasing time of growth.

It should be emphasized, that in spite of the very high SEIRA activity, that is in the same magnitude of order for all measured films, the reproducibility of the growth process (single step hydroxylamine growth) does not seem to be of a high enough grade yet. In fact, it was experienced before and it is known from literature [79], that this process is highly sensitive to any kind of perturbation, and due to perturbation nucleation of Au in solution can occur[1], resulting in a termination of the growth process. Another problem is caused by the stirring of the solution during the growth process. This was done automatically with a teflon coated magnetic stir bar, leading to turbulent flow in the beaker. The samples were exposed to the solution manually with an inert tweezer, making it impossible to ensure the exact same flow conditions for each sample. Better results might be obtained for an automated chemical preparation process.

In the experiments of chap. 5.2.2 the multi step method of hydroxylamine growth was used, where stirring is not necessary and therefore a higher reproducibility is expected.

5.2.1.2. Variation of the angle of incidence

SEIRA of an ODT SAM on an hydroxylamine grown AuNP film on Si substrate was investigated with IR reflection spectroscopy at different angles of incidence ϑ_i. For this measurement, the sample of the previous experiment with a hydroxylamine growth time of 5 min was used. As reference, the reflection of Si had been measured at the respective angle of incidence. In addition to the measurement of the spectra, the ADC intensity measured by the detector was recorded.

Fig. 5.9a shows the spectra of different angles of incidence in the region of the CH-stretching vibration. As the angle of incidence is varied, the baseline of the spectra changes and the height of the absorption peaks changes as well. Starting at $\vartheta_\mathrm{i} = 15°$ and going to larger ϑ_i, the baseline rises and reaches a maximum near $\vartheta_\mathrm{i} = 70°$. Going to even larger angles of incidence ($\vartheta_\mathrm{i} > 70°$) leads to a strong decrease of the baseline. Near $\vartheta_\mathrm{i} = 77°$ the baseline height becomes lower than 1, and the orientation of the spectra is inverted. The behavior of the baseline in this spectral range corresponds to the behavior of the relative intensity $I_\mathrm{sample}/I_\mathrm{reference}$ measured from the detector, that is depicted in Fig. 5.9c. In the same figure the ϑ_i-dependence of the relative

[1] nucleation of Au in solution can be detected by a characteristic color change from yellow ($AuCl_4$ ions) to purple (AuNP in solution).

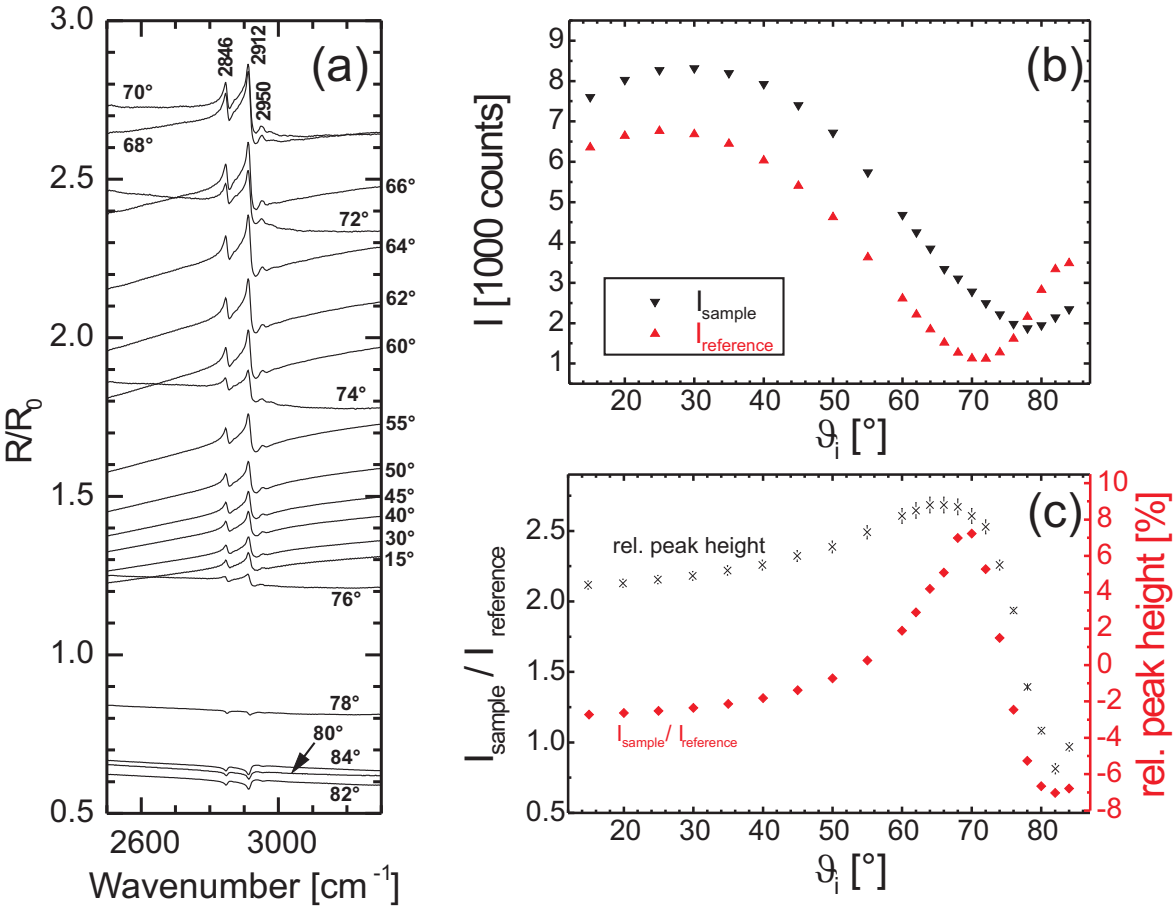

Figure 5.9.: (a) IR reflection spectra (p-pol.) of an ODT SAM on hydroxylamine grown AuNP film on APTES/SiO_2/Si. As reference, the reflection of a SiO_2/Si wafer was measured for different ϑ_i. (b) Total intensity (p-pol.) measured from the detector vs. angle of incidence. This measurement was done (i) with the sample and (ii) with the reference in the reflection unit. (c) Quotient $I_{\text{sample}}/I_{\text{reference}}$ and relative peak height at 2912 cm^{-1} vs. angle of incidence. For more information, see text.

height[2] of the largest absorption peak at 2912 cm^{-1} is shown. Similar to the baseline behavior, the relative peak height rises until it reaches a maximum near $\vartheta_i = 65^\circ$ after which it strongly decreases. As mentioned before, near $\vartheta_i = 77^\circ$ the orientation of the peak is inverted. This behavior can be better understood if the total intensities of the sample reflection and the reference reflection are considered separately as shown in Fig. 5.9b: The total intensity of the reference reflection has a minimum at the Brewster angle ϑ_B near 71°; at this angle a total intensity of $\approx$ 1100 ADC counts is measured. According to eq. (2.19), a Brewster angle of $\vartheta_B = 74^\circ$ is expected for a vacuum/Si interface. However, the natural oxide layer on the Si wafer lowers the refractive index of medium and therefore lowers ϑ_B. Compared to the case of reference reflection, the total intensity of the sample reflection is shifted towards higher values of intensity, and the minimum intensity—i. e. the Brewster angle—is shifted to $\vartheta_B \approx 78^\circ$. Both effects are mainly due to the presence of the AuNP film, which enhances the reflectivity of the sample compared to the bare substrate (in accordance to the calculated spectra shown in Fig. 4.4d on page 53), and which forms an effective medium of Au and vacuum on the SiO_2/Si surface and therefore enlarges the Brewster angle ϑ_B.

This measurement shows, that the angle of incidence $\vartheta_i \approx 65^\circ$ leads to the highest absorption structures, when measuring the relative reflection of an adsorbate layer on hydroxylamine grown AuNP films of this kind. This is a difference compared to IRRAS spectroscopy on thick metal layers, where usually grazing incidence is preferred.

5.2.2. SEIRA of d-ODT on Au nanoparticle films

SEIRA of a d-ODT monolayer on hydroxylamine grown AuNP films on SiO_2/Si substrate was investigated ex-situ with IR transmission spectroscopy (normal incidence). For this experiment, d-ODT was used instead of ODT, because the CD-stretching peaks in the spectra can be considered as a clear fingerprint of the adsorbate. The SEIRA enhancement was estimated by comparing the measured absorption structures with those of a d-ODT monolayer on a smooth Au film.

Variation of Au nanoparticle growth time

The AuNP films had been prepared the following way: (i) deposition of AuNP onto APTES treated SiO_2/Si surface (deposition time: 1 h). (ii) Hydroxylamine growth of the deposited AuNP using the multi step method described in chap. 2.8.3. The number

[2] Because the exact position of the baseline is not known, the peak height was approximated as the difference between the reflection at the maximum R_{max} at 2912 cm^{-1} and at the minimum R_{min} at 2136 cm^{-1}.

of growth cycles of the AuNP was varied from 3 to 7, each cycle lasting for 2 min. After the growth process, the samples were exposed over night to 1 μM solution of d-ODT in ethanol, while the reference samples were exposed to 1 μM solution of ODT for the same period, as shown in the following scheme:

sample layer stack:	reference layer stack:
d-ODT monolayer	ODT monolayer
hydrox. grown AuNP	hydrox. grown AuNP
APTES	APTES
SiO_2/Si	SiO_2/Si

Fig. 5.10 shows the measured spectra in the range of the CD-stretching vibrations. The absorption peaks can be assigned to the CD-stretching vibrations of the CD_2 and CD_3 groups of the d-ODT molecule as follows (see Tab. 2.1 on page 33):

2068 cm^{-1} to 2070 cm^{-1}	sym. CD_3
2084 cm^{-1} to 2089 cm^{-1}	sym. CD_2
2189 cm^{-1} to 2194 cm^{-1}	antisym. CD_2
2215 cm^{-1} to 2219 cm^{-1}	antisym. CD_3

While the 6 min grown AuNP film is least SEIRA active, the 8 min to 12 min grown films show about the same enhancement. However, the significantly highest SEIRA active film is the one grown for 14 min.

SEIRA enhancement factor

An estimation of the SEIRA enhancement factor was done by comparing the height of the CD_2-stretching peaks shown in Fig. 5.10 to the height of the corresponding peak in the non-enhanced d-ODT spectrum shown in Fig. 2.15a on page 34. For this estimation, the 14 min grown AuNP film is considered. With eq. (5.5) and taking into account

$$n_{\mathrm{substr}} = 3.4\,;\ \vartheta_{\mathrm{i}} = 83^\circ\,;\ \frac{\Delta R}{R_0} = 0.13\%\ ,$$

the expected height of the absorption peak in relative transmission would be $\frac{\Delta T}{T_0} = 0.0018\%$. However, the height of the measured absorption peak in transmission is $\frac{\Delta T}{T_0} \approx 0.9\%$; from that follows a SEIRA factor of about 490. In comparison with the

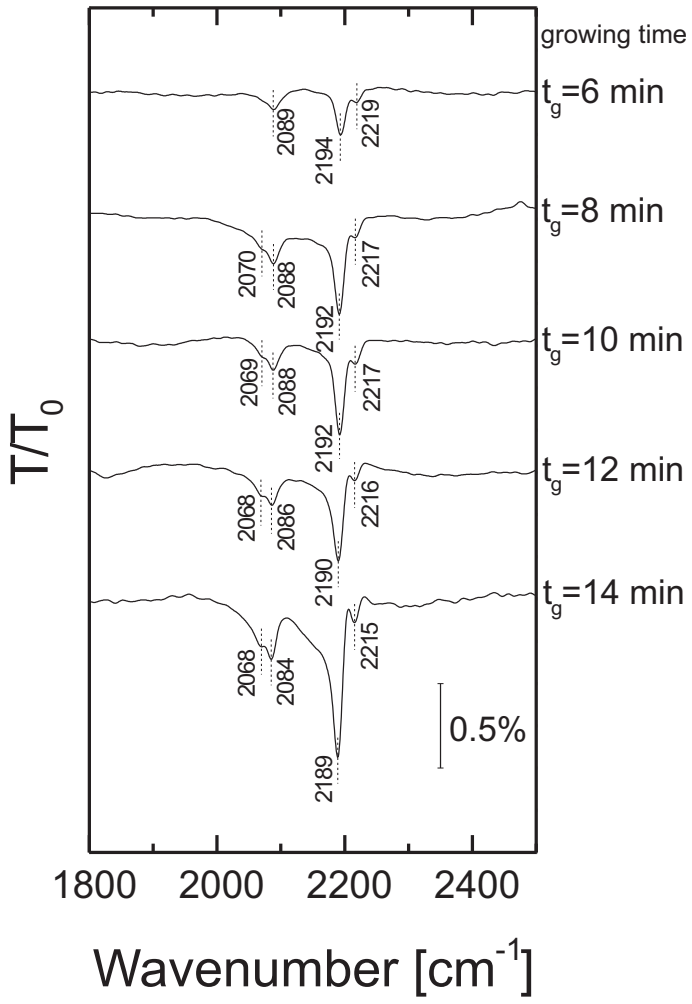

Figure 5.10.: IR transmission spectra (normal incidence) of a d-ODT SAM on hydroxylamine grown AuNP on APTES/SiO_2/Si. The reference was the transmission of an ODT SAM on hydroxylamine grown AuNP on APTES/SiO_2/Si. The growing times refer to the sample and the reference. The spectra are vertically shifted.

SEIRA activity of the AuNP films grown with the single step method, this is about 25%.

Like in chap. 5.2.1 this estimation was done assuming, that the area covered with adsorbates contributing to the signal is equal for the SEIRA film and the flat film, whereas in reality it is smaller for the SEIRA active film, and therefore the SEIRA factor is higher than assumed. Because the exact extend of this error is not known, the conclusion should be, that for both preparation methods, the SEIRA activity is of the same order of magnitude.

SFM analysis

The samples corresponding to the spectra shown in Fig. 5.10 were investigated with SFM; the images are shown in Fig. 5.11. One must keep in mind, that for these images, the same error considerations must be made as discussed in chap. 4.2. Qualitatively, a trend from a high amount of small discrete particles to a smaller amount of larger particles, that are partially connected, is observable when considering films (b) to film (e). Film (b) shows a very interesting state, where small particles are agglomerating to form larger particles. Film (a) consists of particles, that seem to be larger on the lateral scale, than those of film (b), however, on the height scale the particles of film (a) are significantly smaller. This might be an artefact from the tip. Tab. 5.2 shows data extracted from the pictures shown in Fig. 5.11 as described in detail on page 54. Again this was done only for the films consisting of larger nanoparticles as these are less affected by tip convolution; still the data in the table are affected by tip convolution and must be considered as rough estimations.

film	$\frac{A_{\mathrm{cov}}}{A_0}$	$\frac{A_{\mathrm{surf}}}{A_0}$	$\frac{A_{\mathrm{Au}}}{A_0}$	$\frac{V_{\mathrm{Au}}}{V_0}$	d_{nom}[nm]
(c)	0.71	1.56	1.27	0.30	19
(d)	0.88	1.25	1.13	0.38	21
(e)	0.79	1.39	1.18	0.37	22

Table 5.2.: SFM analysis of the AuNP films shown in Fig. 5.11. The given quantities are A_{cov} : area covered by Au, A_0: scanned area, A_{surf}: total 3D surface area, A_{Au}: 3D surface area of the Au, V_{Au}: total volume of the Au, V_0: scanned area × maximum height of AuNP film, d_{nom}: nominal thickness of Au film. For more information, see text.

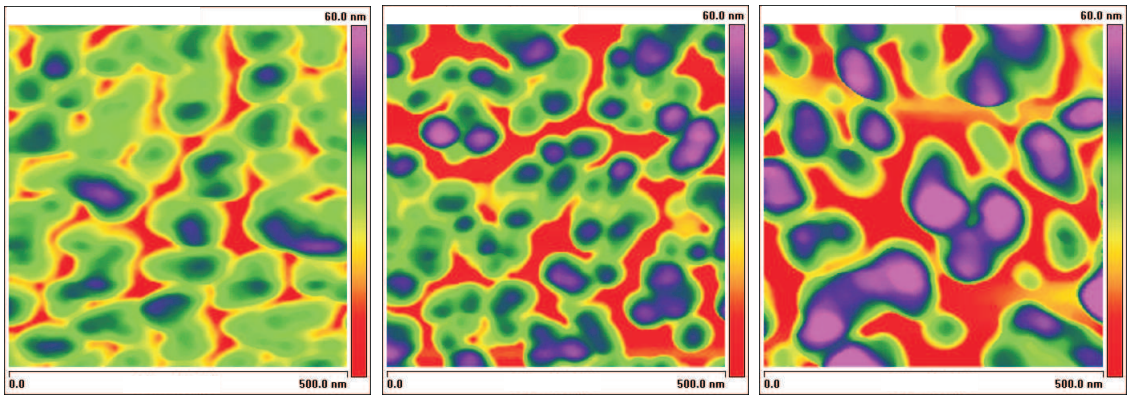

(a) 6 min. (b) 8 min. (c) 10 min.

(d) 12 min. (e) 14 min.

Figure 5.11.: SFM images (500 nm ×500 nm) of hydroxylamine grown AuNP on APTES/SiO_2/Si. The time of hydroxylamine growth was varied in steps of 2 min ranging from 6 min (a) to 14 min (e).

5.2.3. In-situ SEIRA of d-ODT on Au nanoparticle films

SEIRA of d-ODT monolayers on hydroxylamine grown AuNP films were investigated during the adsorption process with in-situ ATR-IR spectroscopy ($\vartheta_i = 30°$, p-pol.). Deuterated ODT was chosen instead of plain ODT in order to separate the IR absorption peaks of the adsorbate monolayer from the ones of the solvent. The AuNP film had been prepared on the APTES treated SiO_2/Si (surface of the ATR crystal) by (i) one hour deposition of AuNP on the surface and (ii) hydroxylamine growth of the deposited AuNP using the multi-step method of Brown et al. [87], applying three to five growth cycles of 2 min each (see chap. 2.8.3). After taking reference spectra with ethanol being in the flow cell, ethanol was replaced by 2 μM solution of d-ODT in ethanol, while relative spectra were taken. The spectral changes in the CD-stretch vibration range are shown in Figs. 5.12a-5.14a. Qualitatively, the series of spectra look very similar for all three experiments; as the d-ODT molecules adsorb on the AuNP film, absorption structures appear, that can be assigned to CD_2 and CD_3 stretching vibrations of the adsorbate, according to the following scheme (see Tab. 2.1 on page 33):

2070 cm^{-1} to 2073 cm^{-1}	sym. CD_3
2090 cm^{-1} to 2091 cm^{-1}	sym. CD_2
2193 cm^{-1} to 2195 cm^{-1}	antisym. CD_2
2214 cm^{-1}	antisym. CD_3

However, a quantitative comparison of the spectra in Figs. 5.12a-5.14a (please notice the different scale) shows, that the area of the absorption peaks is significantly different in the three experiments, as shown in the next paragraph.

Absorption kinetics of d-ODT on AuNP film

For each of the three adsorption experiments the area of the CD-stretching absorption structures was calculated using "OPUS". This was done by integration of the spectra between 2000 cm^{-1} and 2250 cm^{-1} and linearly interpolating the baseline in this range. The result of the calculations is shown in Figs. 5.12b-5.14b. The non-equidistance of the experimental points on the time axis is a result of the changing time resolution during the measurement; so is the different size of the error bars, as the signal-to-noise ratio depends on the acquisition time.

The experimental points in Figs. 5.12b-5.14b were fitted with a first-order Langmuir model (chap. 2.10). Based on eq. (2.68) the time dependence of the peak area was fitted with

$$A(t) = b\left(1 - e^{-ck_L t^a}\right) + d \ , \tag{5.6}$$

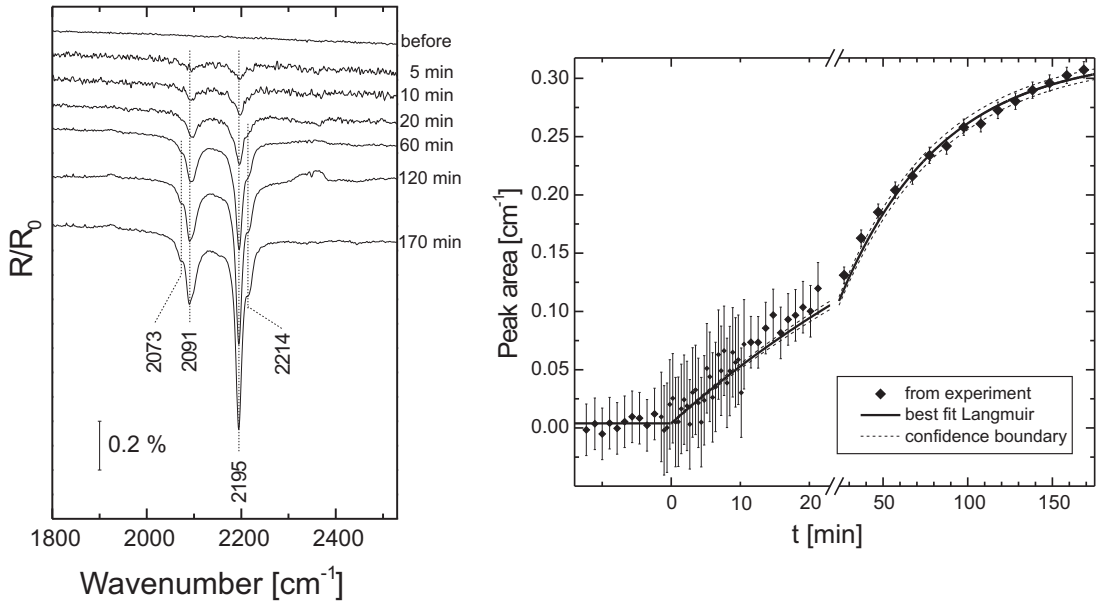

(a) (b)

Figure 5.12.: (a) In-situ ATR-IR spectra ($\vartheta_i = 30°$, p-pol.) of a d-ODT SAM during the adsorption on 3×2 min grown AuNP film/APTES/SiO_2/Si (spectra are vertically shifted, the times next to the spectra refer to the d-ODT injection). The AuNP film has been prepared ex situ one day before the measurement. The reference spectrum was taken with ethanol in the flow cell.
(b) Calculated area and first-order Langmuir fit of the absorption peaks between 2000 cm^{-1} and 2250 cm^{-1} vs. time, where $t = 0$ marks the starting point of d-ODT exposure. The dashed lines are the confidence boundaries according to the standard deviations of the best fit parameters. The kink in the curve is caused by the change of the time scale. For more information, see text.

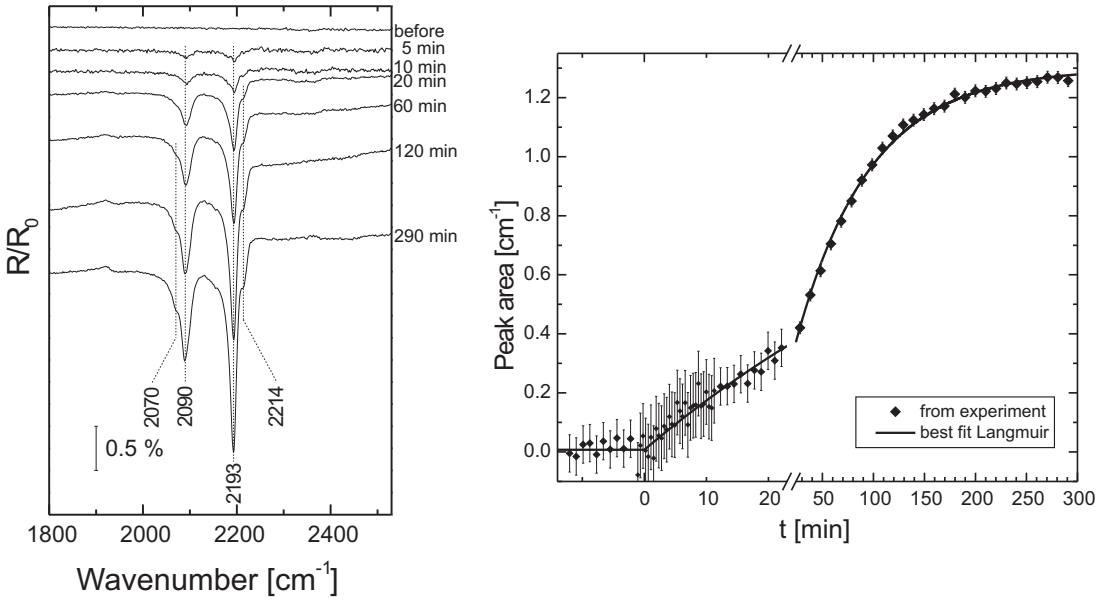

(a) (b)

Figure 5.13.: (a) In-situ ATR-IR spectra ($\vartheta_i = 30°$, p-pol.) of a d-ODT SAM during the adsorption on 4×2 min grown AuNP film/APTES/SiO_2/Si (spectra are vertically shifted, the times next to the spectra refer to the d-ODT injection). The AuNP film has been prepared ex situ one day before the measurement. The reference spectrum was taken with ethanol in the flow cell.
(b) Calculated area and first-order Langmuir fit of the absorption peaks between 2000 cm^{-1} and 2250 cm^{-1} vs. time, where $t = 0$ marks the starting point of d-ODT exposure. The kink in the curve is caused by the change of the time scale. For more information, see text.

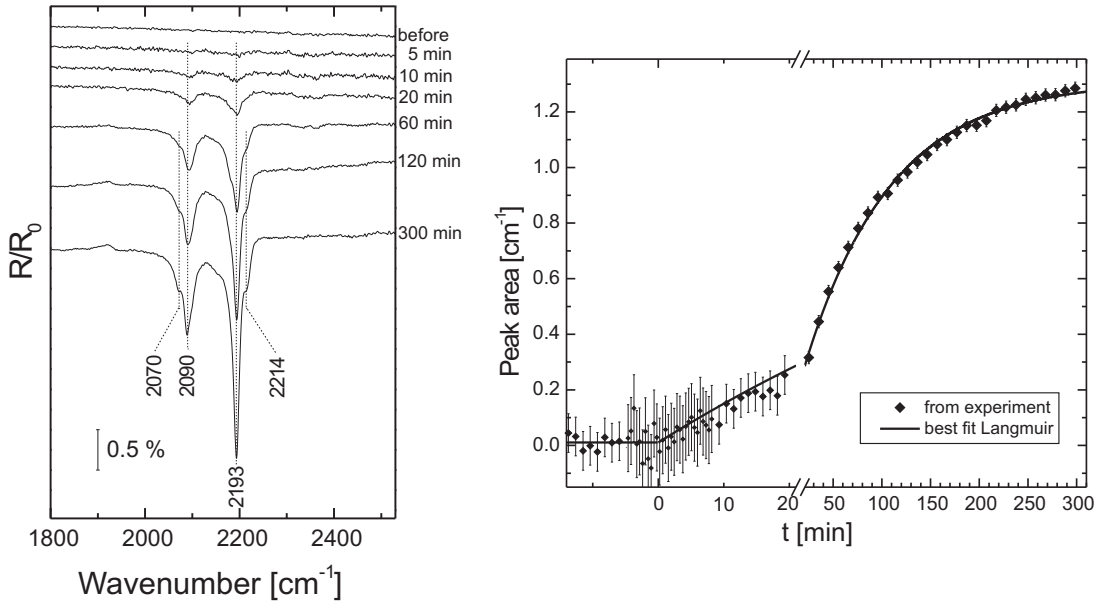

(a) (b)

Figure 5.14.: (a) In-situ ATR-IR spectra ($\vartheta_i = 30°$, p-pol.) of a d-ODT SAM during the adsorption on 5×2 min grown AuNP film/APTES/SiO_2/Si (spectra are vertically shifted, the times next to the spectra refer to the d-ODT injection). The AuNP film has been prepared ex situ one day before the measurement. The reference spectrum was taken with ethanol in the flow cell.
(b) Calculated area and first order Langmuir fit of the absorption peaks between 2000 cm^{-1} and 2250 cm^{-1} vs. time, where $t = 0$ marks the starting point of d-ODT exposure. The kink in the curve is caused by the change of the time scale. For more information, see text.

growth time	Fig.	ck_L $[\frac{l}{mol\,s}]$	$\sigma(ck_L)$ $[\frac{l}{mol\,s}]$	b [cm^{-1}]	$\sigma(b)$ [cm^{-1}]	d [cm^{-1}]	$\sigma(d)$ [cm^{-1}]
3×2 min (i)	5.12b	1.680×10^{-2}	0.040×10^{-2}	0.3163	0.0028	-3.99×10^{-3}	0.71×10^{-3}
4×2 min (ii)	5.13b	1.382×10^{-2}	0.012×10^{-2}	1.2919	0.0034	-7.21×10^{-3}	0.20×10^{-3}
5×2 min (iii)	5.14b	1.138×10^{-2}	0.013×10^{-2}	1.3004	0.0051	-1.06×10^{-2}	0.29×10^{-2}

Table 5.3.: Best fit parameters for the first-order Langmuir model as shown in Figs. 5.12b-5.14b, where $c = 2 \times 10^{-6}\,\mathrm{mol\,l^{-1}}$.

with $a = 1$, which is known as an adequate parameter for n-alkanethiols [93]. The fit parameters were b, ck_L, and d accounting for baseline shifts including those due to possible instabilities during the measurement. In addition to the best fit curve (solid line) in Fig. 5.12b the confidence boundaries are shown as dashed lines, which are based on the standard deviations of the best fit parameters. For the other experiments these confidence boundaries were covered by the best fit curve, and therefore are not shown. All calculated best fit parameters are resumed in Tab. 5.3. In the following, the 3×2 min grown film is regarded as film (i), the 4×2 min grown as film (ii), and the 5×2 min grown as film (iii).

The fit parameter b can be considered as the area of the absorption structures after saturation, since d is negligibly small compared to b. Therefore b is proportional to the SEIRA activity of the film. The SEIRA activities of film (ii) and (iii) are equal within their standard deviation. Film (i) is significantly less SEIRA active than (ii) and (iii).

The rate constant k_L depends on the diffusion process, i. e. the adsorbate molecules, the solvent, and the temperature. Therefore the fit parameter ck_L it is expected to be equal for these three experiments, since all experiments were performed the same way, and the concentration of the molecules was highly reproducible. An explanation for the different values might be differences of the d-ODT injection into the flow cell. It was mentioned before, that the adsorption model described by eq. (2.68) is suited for a diffusion limited adsorption process, meaning that the adsorbate movement is governed only by Brownian motion of the adsorbate molecules. However, the adsorbate molecules are injected into the system by exchanging pure ethanol by adsorbate molecules solved in ethanol; therefore in the beginning of the adsorption process, the movement of the molecules is mainly influenced by the flow of the solvent instead of by Brownian motion, and the assumptions of the Langmuir model are not fulfilled. Also, the fluids were exchanged manually with a syringe, giving rise to errors due to a lack of reproducibility. On the other hand, since this error affects only the very beginning of a long adsorption process, the model for the fit still seems to be appropriate, as shown by the well fitting curves in Figs. 5.12b-5.14b.

As a conclusion of this experiment one can say, that the AuNP films grown for 4×2 min

and for 5×2 min show significantly higher SEIRA activity in ATR spectroscopy than the AuNP film grown for 3×2 min. Therefore, the next experiment—in-situ monitoring of a DNA adsorption process with ATR-IR spectroscopy—was performed with a 5×2 min grown AuNP film.

5.2.4. In-situ SEIRA of 4 base DNA on Au nanoparticle films

The adsorption process of thiolated DNA molecules was monitored in-situ by ATR-IR spectroscopy. The SEIRA active AuNP film was prepared by one hour deposition of AuNP on the APTES treated SiO_2/Si surface (ATR crystal) and by applying the multi-step method of hydroxylamine growth (5 growth cycles of 2 min each, see chap. 2.8.3). The reference was measured with water in the flow cell. Fig. 5.15 shows the changes of the relative reflection, after the water in the flow cell was replaced with 2 μM aqueous solution of 5'-ATCG-3'-C_3H_6-SH (purchased at Eurogentec GmbH, Belgium). As can be seen, several structures occur in the measured range. A comparison with the spectra of adenine, guanine, cytosine, and thymine in Fig. 2.19 on page 39 does not allow a reliable peak assignment, since these spectra were taken from separated nucleic acids and not from DNA strands.

For a comparison, IRRAS spectra ($\vartheta_i = 83°$, p-pol.) of a dry monolayer (and a multilayer, respectively) of 5'-ATCG-3'-C_3H_6-SH on 40 nm Au/Si were measured in vacuum. The DNA multilayer film was prepared by putting 50 μl of 200 μM DNA stock solution on the Au film and letting it dry off. This results in an inhomogeneous film of 10 nmol DNA on about $5 \times 5\,mm^2$ of the Au surface. The reference was the reflection of 40 nm Au/Si. The two IRRAS spectra and the saturated ATR spectrum of Fig. 5.15 are shown in Fig. 5.16. Very strong absorption structures can be seen in the IRRAS spectrum of the DNA multilayer (c). However, because the absorption structures in spectra (a) and (b) are relatively weak, most of them cannot clearly be assigned to structures of spectrum (c). In addition, the structure of the DNA molecules may be different for a dry monolayer, a dry multilayer and a monolayer in water, which can also be a reason for changes in the IR spectra. The dashed box in Fig. 5.16 marks an absorption structure of the ATR-IR spectrum (b), that presumably corresponds with an absorption structure of the IRRAS spectrum (c). Therefore, this structure was used to investigate the time dependence of the adsorption process.

Adsorption kinetics of the DNA molecules

For monitoring the adsorption kinetics, the area of the absorption structure at $1560\,cm^{-1} - 1735\,cm^{-1}$ (dashed box in Fig. 5.15) was calculated for each spectrum. The

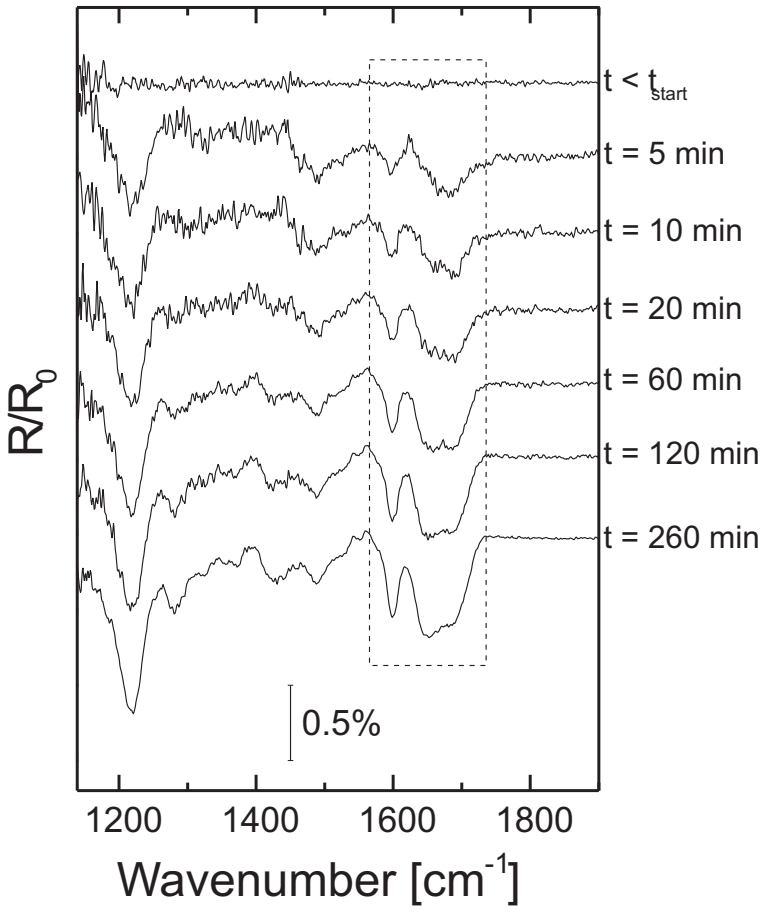

Figure 5.15.: In-situ ATR-IR spectra ($\vartheta_i = 30°$, p-pol.) of 5'-ATCG-3'-C_3H_6-SH during the adsorption on hydroxylamine grown AuNP/APTES/SiO_2/Si. The film preparation is described in the text. Times given with the spectra refer to the point of injection of the DNA solution. The dashed box marks an absorption structure, that is used for monitoring the coverage of the surface by DNA molecules (see on the preceding page). The spectra are vertically shifted.

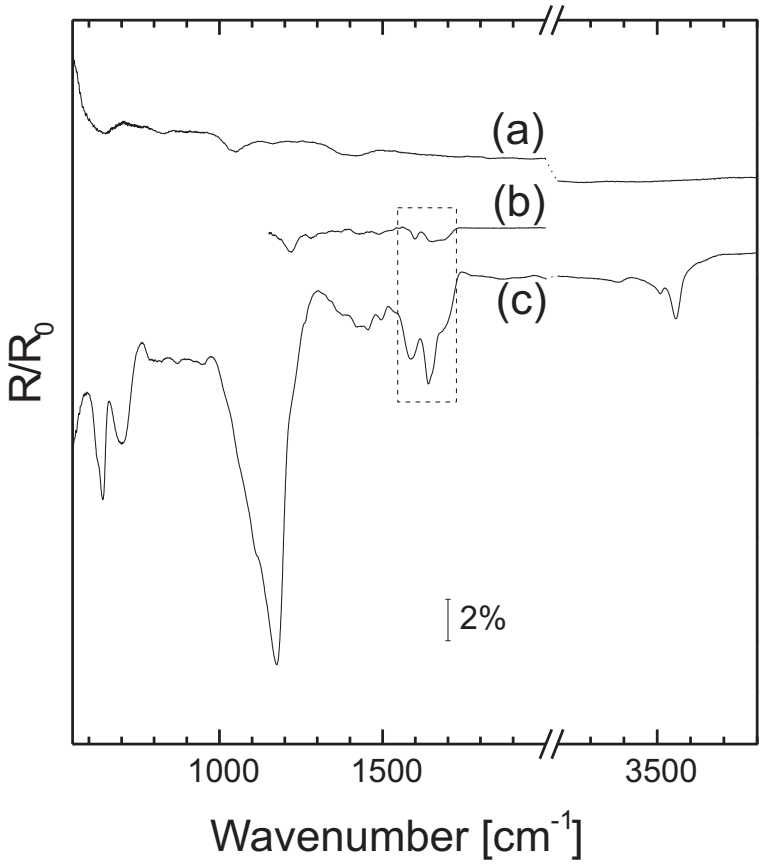

Figure 5.16.: (a) ex-situ IRRAS spectrum (ϑ_i = 83°, p-pol.) of a monolayer 5'-ATCG-3'-C_3H_6-SH on 40 nm Au/1 nm Cr/SiO_2/Si in vacuum, reference: 40 nm Au/1 nm Cr/SiO_2/Si in vacuum,
(b) in-situ IR ATR spectrum (ϑ_i = 30°, p-pol.) of a monolayer 5'-ATCG-3'-C_3H_6-SH on AuNP/APTES/SiO_2/Si in water, reference: AuNP film/APTES/SiO_2/Si in water,
(c) ex-situ IRRAS spectrum (ϑ_i = 83°, p-pol.) of a multilayer 5'-ATCG-3'-C_3H_6-SH on 40 nm Au/1 nm Cr/SiO_2/Si in vacuum, reference: 40 nm Au/1 nm Cr/SiO_2/Si in vacuum.
The dashed box marks an absorption structure, that is used for monitoring the coverage of the surface by DNA molecules. The spectra are vertically shifted.

calculation of the peak area was done with "OPUS" [111] linearly interpolating the baseline between 1560 cm^{-1} and 1735 cm^{-1}. The experimental points were fitted with a first-order Langmuir model. According to previous considerations and eq. (2.68) the time dependence of the peak area was fitted with

$$A(t) = b\left(1 - e^{-ck_{\mathrm{L}}t^{a}}\right) + d \ , \tag{5.7}$$

with $a = 0.5$ and b, ck_{L}, and d being best fit parameters:

	best fit	σ
b	0.829	0.014
ck_{L}	$0.0994\,s^{-1}$	$0.0034\,s^{-1}$
d	0.0277	0.0029

The concentration of DNA in solution was $c = 2 \times 10^{-6}\,mol\,l^{-1}$. As can be seen in Fig. 5.17, where the peak area vs. time is plotted, the selected peak area and therefore presumably the Au surface coverage by DNA molecules fits to the first-order Langmuir model with $a = 0.5$. In the beginning of the adsorption process there is a deviation, as the majority of the points lies beneath the best fit curve. However, most points are—within the error—on the fit curve. The applicability of this model therefore suggests a diffusion limited adsorption processes, where every molecule having contact with the surface is bound.

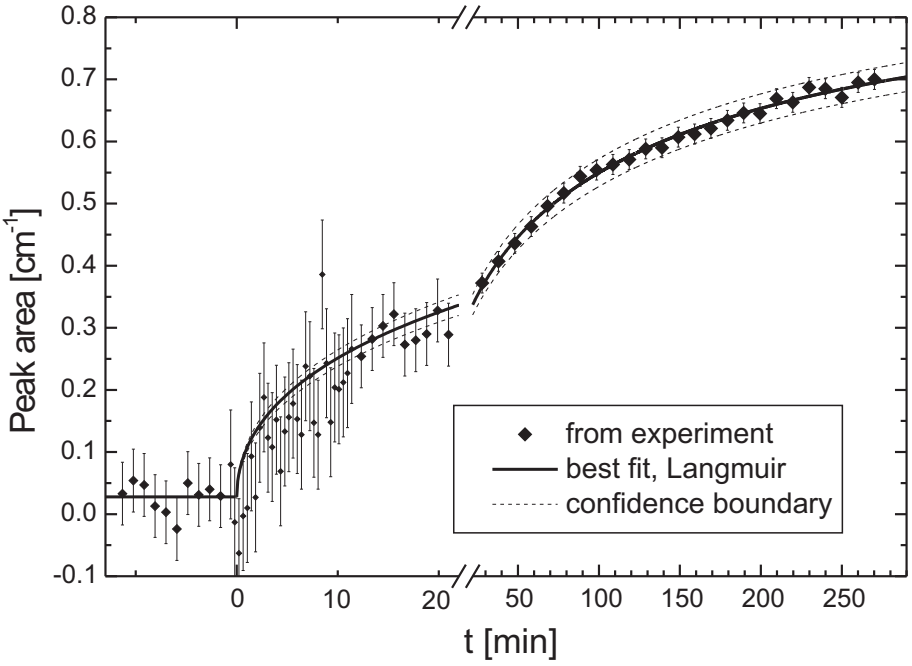

Figure 5.17.: Calculated area of the absorption structure at $1560\,\mathrm{cm^{-1}} - 1735\,\mathrm{cm^{-1}}$ (dashed box in Fig. 5.15) and first-order Langmuir fit of the peak area vs. time. The dashed lines are the confidence boundaries according to the standard deviations of the best fit parameters. The point $t = 0$ marks the time when DNA was injected into the system; the kink in the curve is caused by the change of the time scale at $t = 22\,\mathrm{min}$. During the acquisition of the spectra the time resolution was adapted, causing a non-equidistance of the measured points on the time axis and a change of the size of the error bars due to the different signal-to-noise ratio.

6. Summary and conclusion

In this thesis, the SEIRA activity of wet chemically prepared Au nanoparticle films was investigated focusing on a better applicability in optical biosensing. The films were prepared by deposition of AuNP onto the substrate and a wet chemical enlargement of the nanoparticles, to get the typical SEIRA active morphology of densely packed but yet separate islands. The resulting morphology was characterized by VIS spectroscopy, scanning force microscopy, scanning electron microscopy and IR spectroscopy of adsorbates. By comparing SEIRA enhanced spectra of adsorbates with non-enhanced spectra of the same adsorbate, a factor of the enhancement could be estimated. These estimations show, that films of non-grown Au nanoparticle submonolayers were able to enhance the absorption signals of antibodies by a factor of roughly 26, while in case of grown Au nanoparticle films a SEIRA enhancement by three orders of magnitude was observed with octadecanethiol as adsorbate. Even if these values are affected by several uncertainties—e. g. the exact effective surface increase for the adsorbate is unknown and the reproducibility for film preparation is yet to optimize—the obtained information is very important for a deeper understanding of SEIRA and its routinely application in biology and medicine.

VIS spectroscopy of Au nanoparticles

VIS spectroscopy has shown to be a suitable characterization method for Au nanoparticle films close to the percolation threshold. Measurements and comparing calculations showed, that the spectral behavior of Au nanoparticle films near the percolation threshold is dominated by a surface plasmon polariton resonance, then becomes broader with increasing filling fraction, finally leading to a non-transmitting film in consistence with theory. The transmission and reflection spectra can be described with a 3D Bruggeman effective medium model using the bulk dielectric function of Au. While interband transitions of d-electrons have to be taken into account, the neglect of intrinsic size effects, i. e. size dependence of the dielectric function for particles smaller than $R \leq 25\,\mathrm{nm}$, does not lead to great discrepancies between experimentally obtained and calculated spectra.

SFM and SEM of Au nanoparticle films

Scanning probe microscopy like SFM and SEM have showed to be a very helpful tool for the analysis of film morphology. When being aware of the advantages, disadvantages and errors of both methods, they can be partially complementary methods of analysis. SEM has the advantage of a much higher resolution compared to SFM, in addition it is a much faster method. As a result, it is easy to look onto large areas of the sample in a reasonable time, compared to SFM, were a change of scanning area is rather time consuming, since usually the tip has to be lifted and contacted again. Because of the good resolution (typically up to 2 nm) the coverage of the substrate by Au is imaged very accurately. This is not the case for SFM, if the sample consists of structures in the same size regime as the tip radius. On the other hand, SFM images contain a height profile of the morphology, and therefore also provide very important information.

The SFM images of hydroxylamine grown AuNP films (multi step method after one hour of AuNP deposition) show, that with increasing growth time more Au is placed on the substrate; this is strongly suggested from the height of the particles and their lateral dimensions. With increasing growth time, the nanoparticles have a tendency to coagulate, engaging the smaller particles. This leads to rather widely branched structures, similar to physically evaporated films near the percolation threshold.

The SEM images of hydroxylamine grown AuNP films (single step method after three hours of AuNP deposition) show roughly similar behavior: while for short growth time, there are still single nanoparticles and rather narrow branched islands, the small islands cannot be found for longer growth times, as they are engaged by larger widely branched Au islands. All of the SEM investigated films still consist of discrete particles with the bare substrate in between.

IR spectroscopy of adsorbates on Au nanoparticle films

In order to get information about the SEIRA activity of the chemically prepared AuNP film, IR spectra of adsorbates on the respective Au film were measured. This was done in transmission geometry, reflection geometry, and ATR geometry.

In-situ monitoring of Au nanoparticles adsorption on SiO_2/Si The adsorption process of AuNP on the APTES treated SiO_2/Si was monitored with in-situ ATR-IR spectroscopy. During the adsorption process, a SEIRA active Au nanoparticle submonolayer was formed, as indicated by an enhancement of the OH-stretching and OH-bending absorption band from the surrounding water. This enhancement is only affected by the enhancement of the electromagnetic field between the particles; the

chemical first-layer effect cannot enhance the water's vibrational bands, since the first layer of the AuNP is still occupied by the negatively charged citrate layer.

Since the height of the relative absorption band was proportionally to the nanoparticle coverage of the surface, the relative peak height vs. time plot depicted the time dependence of the coverage. It could be shown, that the main part of the nanoparticle deposition process takes place within the first 20 minutes, and saturation is reached after approximately two hours. In the literature, some recipes suggest exposition times of the surface to the AuNP dispersion of several hours; as a consequence of this experiment a deposition time of one hour was determined to be sufficient. It could be shown, that the adsorption process can be described with a first-order Langmuir model.

By exposition of the immobilized AuNP to AET, it was possible to replace their citrate coverage with an AET layer. The repellent forces between the amino groups of the AET and the amino groups of the APTES layer are presumably responsible for a desorption of the AuNP from the surface. The desorption process could be detected in the ATR-IR spectra, as the SEIRA increased absorption bands of the surrounding water decreased again, i. e. in the relative spectra an absorption signal appeared, showing to higher relative reflection. Thus it could be shown, that the deposition process of AuNP onto APTES treated SiO_2/Si substrate is reversible.

For Au nanoparticle submonolayers prepared by deposition onto a substrate for a certain time, one can say, that even if the SEIRA activity is not at its optimum because of the large average distance between the particles, these films are reproducible in preparation; however care must be taken, since the adsorbate may cause this film to be removed from the substrate.

Antibody-antigen coupling on Au nanoparticles Au nanoparticle submonolayers were used as basis of an optical biosensor sensitive to a specific antigen. For comparison, a smooth Au film on SiO_2/Si substrate, that was known to be SEIRA inactive, was prepared the exact same way as the SEIRA active sensor. In case of specific antibody-antigen coupling the characteristic vibrational absorption structures of proteins could be identified in the IR spectra – these could not be seen for biosensors exposed to unspecific antigens, demonstrating, that this coupling does not take place in a significant quantity. In comparison to a non-SEIRA active biosensor, the AuNP film was enhanced by a factor of about 26.

SEIRA of alkanethiols on AuNP Hydroxylamine growth of AuNP was used to create films with a morphology near the percolation threshold to increase the SEIRA activity. For the growth process two methods were used – referred to as the single

step method and the multi step method. The SEIRA activity was investigated by comparison of adsorbate experiments with SEIRA active films and non-SEIRA active films, as adsorbate the well investigated octadecanethiol was used (d-octadecanethiol, respectively). The SEIRA enhancement of the films was by three orders of magnitude. It was remarkable, that for each series, the SEIRA factor was within the same order of magnitude, even if SFM or SEM images indicated significant differences of the morphology. On the other hand, in spite of these differences, all films consisted of relatively densely packed metal islands that were still separated, and therefore were in the range of percolation – a known condition for high SEIRA activity.

In addition to ex-situ experiments in transmission and reflection geometry, in-situ ATR-IR measurements were carried out, with d-octadecanethiol being the adsorbate. This experiment was done with several hydroxylamine grown AuNP films, where the time of growth was varied. The absorption structures of the d-octadecanethiol monolayer in the spectra were large enough not only to clearly identify the molecule by its spectral fingerprint (CD-stretch vibration), but also to monitor the adsorption process. In accordance to literature, the time dependent coverage of the surface was in agreement with a first-order Langmuir model.

SEIRA of DNA on AuNP After SEIRA activity of hydroxylamine grown AuNP films was investigated in ATR geometry, a film with high SEIRA activity was used for the investigation of the adsorption process of a thiolated DNA molecule (5'-ATCG-3'-C_3H_6-SH). As expected from a rather complex biomolecule many absorption structures appeared in the relative reflection spectra during the adsorption process; it was possible to monitor the adsorption process of the DNA molecule by considering the time dependence of the area of absorption structures. Like in case of the octadecanethiol, the adsorption process was found to yield a first-order Langmuir model, leading to the conclusion, that the adsorption process of the DNA molecules is diffusion controlled, and that every DNA molecule that makes contact to the Au surface adsorbs.

SEIRA in biospectroscopy

The experiments presented in this thesis clearly show the advantages, that wet chemically prepared SEIRA active AuNP films offer to biospectroscopy. With the experimental setup and the wet chemical preparation of Au films, it is possible to detect monolayers of biomolecules and monitor the adsorption process in-situ by taking advantage of the SEIRA effect.

In comparison to physically evaporated films, the preparation of wet chemical AuNP films is much less time consuming, since no ultra high vacuum treatment is required,

and therefore no time consuming activities like bakeouts or leak detection have to be done. There is also no need for an adhesive metal layer such as Cr or Ti. In addition to this, a positive side effect is the strongly decreased financial effort that is needed for this preparation method, which does not significantly exceed the cost for the chemicals and for glass ware. The enhancement factors obtained by this preparation method were remarkably high by three orders of magnitude.

On the other hand, although it was possible to reproducibly prepare SEIRA active films, more control on the film growth i. e. on the morphology would be desirable. It seems, that in the process of wet chemical preparation, there are still uncertainties, that foreclose the exact reproducibility, meaning that performing the exact same preparation twice would lead to the same morphology in the SFM or SEM image, and therefore to the exact same SEIRA enhancement. Here, the critical point is certainly the growing process of the AuNP, that takes place in a short time with relatively low reproducibility. This was especially the case for the AuNP films grown with the hydroxylamine single step method, as could be detected with SEM. The main reason for this is presumably the required stirring, that leads to a turbulent flow inside the beaker during the growth process. Therefore, considering the reproducibility of film preparation, the multi step method is certainly more promising.

A. Abbreviations

AB	antibody
ADC	analog-digital converter
AFM	atomic force microscopy (=scanning force microscopy)
APTES	(aminopropyl)triethoxysilane
ATR	attenuated total reflection
DNA	deoxyribonucleic acid
d-ODT	deuterated octadecanethiol
Ig	immunoglobulin (antibody)
IR	infrared
IRRAS	infrared reflection absorption spectroscopy
LN_2	liquid nitrogen
MCT	mercury cadmium telluride
PP	polypropylene
PVC	polyvinyl chloride
RNA	ribonucleic acid
SAM	self assembling monolayer
SEIRA	surface enhanced infrared absorption
SEM	scanning electron microscopy
SERS	surface enhanced Raman scattering
SFM	scanning force microscopy (=atomic force microscopy)
UV	ultraviolet
VIS	visual

B. Various IR spectra

B.1. Silicon

Fig. B.1 shows IR transmission spectra of a double sided polished and a single sided polished Si wafer. Both wafers had a naturally grown oxide layer, resulting in absorption at 1109 cm^{-1}. The other absorption structures result from dopants like B or N. Above 1500 cm^{-1} no absorption structures can be seen in the spectra, and the relative transmission is $T/T_0 \approx 65\%$ in case of the double sided polished wafer (because of reflection losses on the interfaces). In case of the single sided polished wafer, the transmission becomes lower with increasing wavenumber because of scattering.

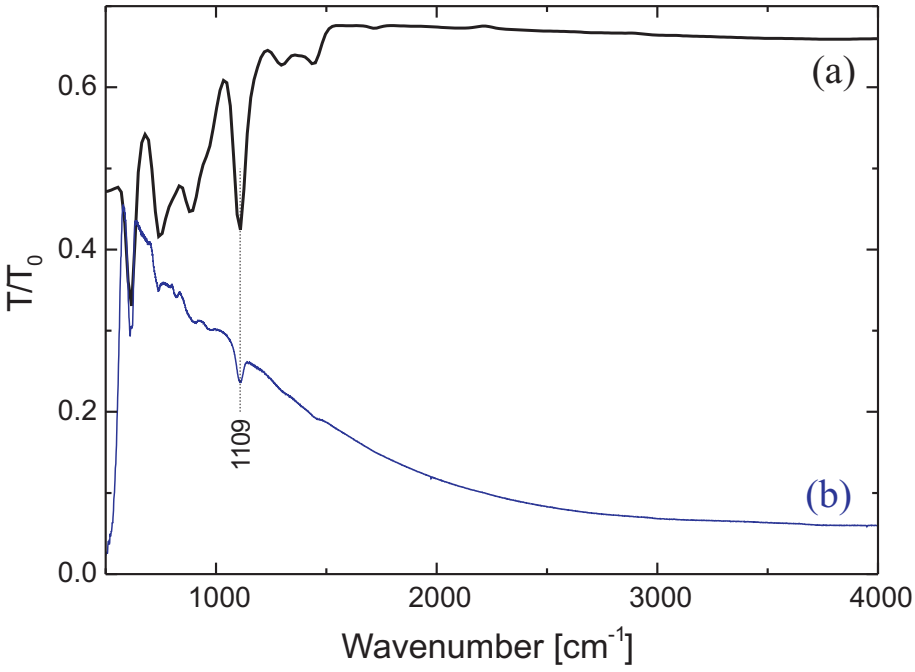

Figure B.1.: IR transmission spectra (normal incidence) of Si wafers. (a) 1.6 mm thick double sided polished wafer, (b) 0.5 mm thick single sided polished wafer. The reference was the transmission of vacuum.

B.2. Water

Fig. B.2 shows an ATR-IR spectrum (45°) of water. In the measured range two strong absorption signals can be seen; the peak at 1640 cm^{-1} can be assigned to the OH in-plane bending mode, while the very strong structure in the range 2800 cm^{-1} −3600 cm^{-1} originates from OH stretching vibrations [124, 125].

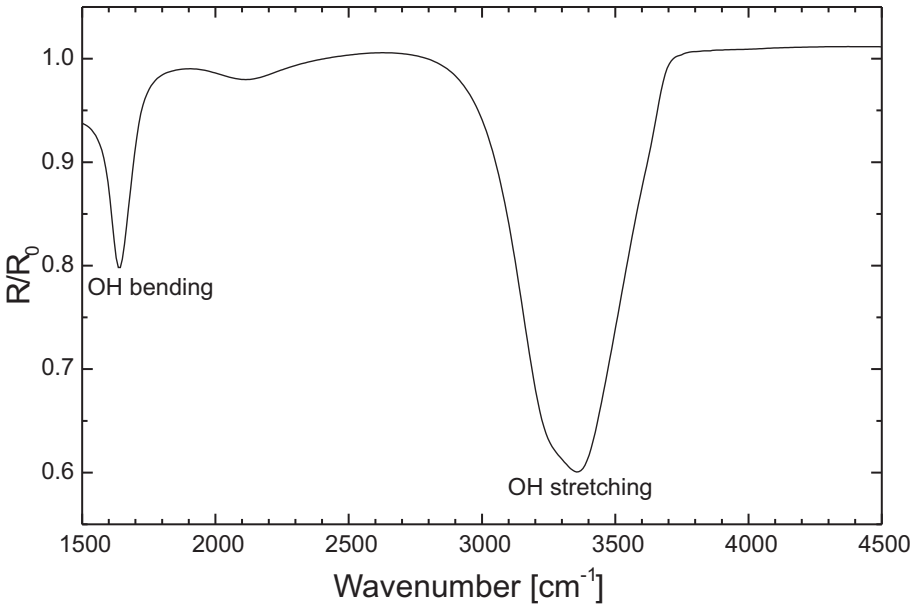

Figure B.2.: ATR-IR spectrum ($\vartheta_i = 45°$) of water. The reference spectrum was taken with air contacting the ATR crystal.

Bibliography

[1] A. Hartstein, J. R. Kirtley, and J. C. Tsang. Enhancement of the infrared absorption from molecular monolayers with thin metal overlayers. *Phys. Rev. Lett.*, 45:201–204, 1980.

[2] A. Otto, I. Mrozek, H. Grabhorn, and W. Akemann. Surface-enhanced Raman scattering. *J. Phys. Condens. Matter*, 4:1143–1212, 1992.

[3] A. Pucci. IR spectroscopy of adsorbates on ultrathin metal films. *phys. stat. sol. (b)*, 2005. (in press, DOI 10.1002/pssb.200541131).

[4] H. D. Wanzenböck, N. Weissenbacher, and R. Kellner. Surface enhanced infrared absorption (SEIRA) observed on different metal surface structures. *AIP*, 430:598–601, 1998.

[5] T. R. Jensen, R. P. van Duyne, S. A. Johnson, and V. A. Maroni. Surface-enhanced infrared spectroscopy: A comparison of metal island films with discrete and nondiscrete surface plasmons. *Appl. Spectrosc.*, 54:371–377, 2000.

[6] M. Osawa. Dynamic processes in electrochemical reactions studied by surface-enhanced infrared absorption spectroscopy (SEIRAS). *Bull. Chem. Soc. Jpn.*, 70:2861–2880, 1997.

[7] Y. Nishikawa, T. Nagasawa, K. Fujiwara, and M. Osawa. Silver island films for surface-enhanced infrared absorption spectroscopy: Effect of island morphology on the absorption enhancement. *Vib. Spectrosc.*, 6:43–53, 1993.

[8] A. Priebe, M. Sinther, G. Fahsold, and A. Pucci. The correlation between film thickness and adsorbate line shape in surface enhanced infrared absorption. *J. Chem. Phys.*, 119:4887–4890, 2003.

[9] M. Osawa, K. Kuramitsu, A. Hatta, W. Suëtaka, and H. Seki. Electromagnetic effect in enhanced infrared absorption of adsorbed molecules on thin metal films. *Surf. Sci.*, 175:L787–L793, 1986.

[10] M. Osawa and K. Ataka. Electromagnetic mechanism of enhanced infrared absorption of molecules adsorbed on metal island films. *Surf. Sci.*, 262:L118–L122, 1992.

[11] Y. Nakao and H. Yamada. Enhanced infrared ATR spectra of surface layers using metal films. *J. Electron Spectrosc. Relat. Phenom.*, 45:189–196, 1987.

[12] T. Watayama, T. Sakurai, S. Ichikawa, and W. Suëtaka. Charge-transfer enhancement in infrared absorption of thiocyanate ions adsorbed on a gold electrode in the Kretschmann ATR configuration. *Surf. Sci.*, 198:L359–L364, 1988.

[13] S. Badilescu, P. V. Ashrit, V.-V. Truong, and I. I. Badilescu. Enhanced infrared ATR spectra of o-, m-, and p-nitrobenzoic acid with Ag films. *Appl. Spectrosc.*, 43:549–552, 1989.

[14] V. M. Shalaev, R. Botet, J. Mercer, and E. B. Stechel. Optical properties of self-affine thin films. *Phys. Rev. B*, 54:8235–8242, 1996.

[15] M. Osawa, K. Ataka, K. Yoshii, and N. Nishikawa. Surface-enhanced infrared spectroscopy: The origin of the absorption enhancement and band selection rule in the infrared spectra of molecules adsorbed on fine metal particles. *Appl. Spectrosc.*, 47:1497–1502, 1993.

[16] P. Kambhampati and A. Campion. Surface enhanced Raman scattering as a probe of adsorbate-substrate charge-transfer excitations. *Surf. Sci*, 427-428:115–125, 1999.

[17] D. C. Langreth. Energy transfer at surfaces: Asymmetric line shapes and the electron-hole-pair mechanism. *Phys. Rev. Lett.*, 54:126–129, 1985.

[18] Z. Y. Zhang and D. C. Langreth. Electronic damping of adsorbate fundamental and overtone vibrations at metal surfaces. *Phys. Rev. B*, 39:10028–10046, 1989.

[19] W. Suëtaka. *Surface Infrared and Raman Spectroscopy: Methods and Applications*. Plenum Press, New York, USA, 1995.

[20] S. Pronkin and Th. Wandlowski. ATR-SEIRAS—an approach to probe the reactivity of Pd-modified quasi-single crystal gold film electrodes. *Surf. Sci*, 573:109–127, 2004.

[21] Y. Nishikawa, K. Fujiwara, K. Ataka, and M. Osawa. Surface-enhanced infrared external reflection spectroscopy at low reflective surfaces and its application to surface analysis of semiconductors, glasses, and polymers. *Anal. Chem.*, 65, 1993.

[22] Y. Nishikawa, K. Fujiwara, and T. Shima. A study on the qualitative and quantitative analysis of nanogram samples by transmission infrared spectroscopy with the use of silver island films. *Appl. Spectrosc.*, 45:747–751, 1991.

[23] S. Sato and T. Suzuki. Study of surface-enhanced IR absorption spectroscopy over evaporated Au films in an ultrahigh vacuum system. *Appl. Spectrosc.*, 51:1170–1175, 1997.

[24] C. W. Brown, Y. Li, J. A. Seelenbinder, P. Pivarnik, A. G. Rand, S. V. Letcher, O. J. Gregory, and M. J. Platek. Immunoassays based on surface-enhanced infrared spectroscopy. *Anal. Chem.*, 70:2991–2996, 1998.

[25] G. I. Dovbeshko, V. I. Chegel, N. Y. Gridina, O. P. Repnytska, Y. M. Shirshov, and V. P. Tryndiak. Surface enhanced IR absorption of nucleic acids from tumor cells: FTIR reflectance study. *Biopolymers*, 67:470–486, 2002.

[26] K. Ataka and J. Heberle. Electrochemically induced surface-enhanced infrared difference absorption (SEIDA) spectroscopy of a protein monolayer. *J. Am. Chem. Soc*, 125:4986–4987, 2003.

[27] K. Ataka and J. Heberle. Functional vibrational spectroscopy of a cytochrome c monolayer: SEIDAS probes the interaction with different surface-modified electrodes. *J. Am. Chem. Soc.*, 126:9445–9457, 2004.

[28] A. Priebe, G. Fahsold, W. Geyer, and A. Pucci. Enhanced infrared absorption of CO on smooth iron ultrathin films in correlation to their crystalline quality. *Surf. Sci.*, 502-503:388, 2002.

[29] L.-J. Wan, M. Terashima, H. Noda, and M. Osawa. Molecular orientation and ordered structure of benzenethiol adsorbed on gold(111). *J. Phys. Chem. B*, 104:3563–3569, 2000.

[30] M. Futamata. Coadsorbed state of uracil, water and sulfate species on the gold electrode surface. *Chem. Phys. Lett.*, 317:304–309, 2000.

[31] M. Futamata. Unique adsorbed state of 4,4'-BiPy and $BiPyH_2^{2+}$ on Au(111) electrode. *Chem. Phys. Lett.*, 332:421–427, 2000.

[32] M. Futamata. Adsorbed state of 4,4'-BiPy and $BiPyH_2^{2+}$ on Au(111) electrode. *J. Phys. Chem. B*, 105:6933–6942, 2001.

[33] A. Priebe, G. Fahsold, and A. Pucci. Surface enhanced infrared absorption of CO on smooth iron ultrathin films. *Surf. Sci.*, 90:482–485, 2001.

[34] O. Krauth, G. Fahsold, and A. Pucci-Lehmann. IR-spectroscopy of CO on iron ultrathin metal films. *J. Mol. Struct.*, 482-483:237–240, 1999.

[35] A. Priebe, F. Meng, and A. Pucci. IR spectra of adsorbates on rough metal films. *Asian J. Phys.* (in press).

[36] N. Goutev and M. Futamata. Attenuated total reflection surface-enhanced infrared absorption spectroscopy of carboxyl terminated self-assembled monolayers on gold. *Appl. Spectrosc.*, 57:506–513, 2003.

[37] A. A. Kamnev, L. A. Dykman, P. A. Tarantilis, and M. G. Polissiou. Spectroimmunochemistry using colloidal gold bioconjugates. *Bioscience Reports*, 22:541–547, 2002.

[38] J. A. Seelenbinder, C. W. Brown, P. Pivarnik, and A. G. Rand. Colloidal gold filtrates as metal substrates for surface-enhanced infraread absorption spectroscopy. *Anal. Chem.*, 71:1963–1966, 1999.

[39] H. Miyake, S. Ye, and M. Osawa. Electroless deposition of gold thin films on silicon for surface-enhanced infrared spectroelectrochemistry. *Electrochem. Commun.*, 4:973–977, 2002.

[40] D. Enders. Oberflächenverstärkte Infrarotabsorption von Molekülen in flüssiger Umgebung. Diploma Thesis, University of Heidelberg, 2002.

[41] H. Günzler and H.-U. Gremlich. *IR-Spektroskopie*. Wiley-VCH, Weinheim, 4^{th} edition, 2003.

[42] O. Stenzel. *Das Dünnschichtspektrum*. Akademie Verlag, Berlin, Germany, 1996.

[43] Scout – software package for optical spectroscopy, including dielectic function database, supplied by M. Theis Hard- and Software, Aachen.

[44] O. Krauth. Untersuchung der oberflächenverstärkten Infrarotabsorption am System Kohlenmonoxid auf dünnen Eisenfilmen. Thesis, University of Heidelberg, 1999.

[45] A. Lehmann. *phys. stat. sol. (b)*, 148:401, 1988.

[46] R. G. Greenler. Infrared study of adsorbed molecules on metal surfaces by reflection techniques. *J. Chem. Phys.*, 44:310–315, 1966.

[47] Y. J. Chabal. Surface infrared spectroscopy. *Surf. Sci. Rep.*, 8:211, 1988.

[48] D. Berreman. Infrared absorption at longitudinal optic frequency in cubic crystal films. *Phys. Rev.*, 130:2193–2198, 1963.

[49] N. J. Harrick. Surface chemistry from spectral analysis of totally internally reflected radiation. *J. Phys. Chem.*, 64:1110–1114, 1960.

[50] J. Fahrenfort. Attenuated total reflection: A new principle for the production of useful infra-red reflection spectra of organic compounds. *Spectrochim. Acta*, 17:698–709, 1961.

[51] N. J. Harrick. *Internal Reflection Spectroscopy*. Harrick Scientific Corporation, New York, 1979.

[52] J. D. Jackson. *Classical Electrodynamics*. John Wiley and Sons, New York, 1999.

[53] N. J. Harrick. Electric field strengths at totally reflecting interfaces. *J. Opt. Soc. Am.*, 55:851, 1965.

[54] U. Kreibig and M. Vollmer. *Optical Properties of Metal Clusters*. Springer, Berlin, 1995.

[55] F. Abelès. Optical properties of metals. In F. Abelès, editor, *Optical Properties of Solids*, pages 93–162. North-Holland Publishing Company, Amsterdam, Netherlands, 1972.

[56] N. E. Christensen. Relativistic band calculation and the optical properties of gold. *Phys. Rev. B*, 4:3321–3344, 1971.

[57] P. Grosse. *Freie Elektronen in Festkörpern*. Springer-Verlag, Berlin, Germany, 1979.

[58] P. B. Johnson and R. W. Christy. Optical constants of the noble metals. *Phys. Rev. B*, 6:4370–4379, 1972.

[59] D. W. Lynch and W. R. Hunter. In E. D. Palik, editor, *Handbook of Optical Constants of Solids*, volume 1. Academic Press, 1985.

[60] M. Faraday. *Phil. Trans. R. Soc. London, Ser. A*, 147:145, 1857.

[61] G. Mie. Beiträge zur Optik trüber Medien, speziell kolloidaler Metallösungen. *Ann. Phys.*, 25:377, 1908.

[62] Luis M. Liz-Marzán. Nanometals: formation and color. *Materials Today*, pages 26–31, Feb. 2004.

[63] P. Mulvaney. Surface plasmon spectroscopy of nanosized metal particles. *Langmuir*, 12:788–800, 1996.

[64] A. Pinchuk, U. Kreibig, and A. Hilger. Optical properties of metallic nanoparticles: influence of interface effects and interband transitions. *Surf. Sci*, 557:269–280, 2004.

[65] B. N. J. Persson. Polarizability of small spherical metal particles: influence of the matrix environment. *Surf. Sci.*, 281:153–162, 1993.

[66] E. Zaremba and B. N. J. Persson. Dynamic polarizability of small metal particles. *Phys. Rev. B*, 35:596–606, 1987.

[67] N. G. Khlebtsov, V. A. Bogatyrev, L. A. Dykman, and A. G. Melnikov. Spectral extinction of colloidal gold and its biospecific conjugates. *J. Colloid Interface Sci.*, 180:436–445, 1996.

[68] J. C. Maxwell-Garnett. Colours in metal glasses and in metallic films. *Philos. Trans. R. Soc. London*, (203):385, 1904.

[69] V. P. Tolstoy, I. V. Chernyshova, and V. A. Skryshevsky. *Handbook of infrared spectroscopy of ultrathin films*. John Wiley and Sons, Inc., New Jersey, USA, 2003.

[70] H. Fröhlich. *Theory of Dielectrics*. Clarendon Press, Oxford, 2^{nd} edition, 1958.

[71] V. P. Tolstoy, I. V. Chernyshova, and V. A. Skryshevsk. *Handbook of infrared spectroscopy of ultrathin film*, pages 60–64. John Wiley and Sons, Inc, New Jersey, USA.

[72] R. Ruppin. Evaluation of extended Maxwell-Garnett theories. *Opt. Comm.*, 182:273–279, 2000.

[73] D. A. G. Bruggeman. Berechnung verschiedener physikalischer Konstanten von heterogenen Substanzen. *Ann. Phys. Lpz.*, 24:636–679, 1934.

[74] P. Starzetz. Vorausberechnung des IR-Transmissionsvermögens ultradünner Eisenfilme auf MgO(001). Diploma Thesis, University of Heidelberg, 2000.

[75] S. Yoshida and T. Yamaguchi A. Kinbara. Optical properties of aggregated silver films. *J. Opt. Soc. Am.*, 61:62–69, 1971.

[76] A. Vial, A.-S. Grimault, D. Macías, D. Barchiesi, and M. L. de la Chapelle. Improved analytical fit of gold dispersion: Application to the modeling of extinction spectra with a finite-difference time-domain method. *Phys. Rev. B*, 71:085416, 2005.

[77] H. Xu, E. J. Bjerneld, M. Käll, and L. Börjesson. Spectroscopy of single hemoglobin molecules by surface enhanced raman scattering. *Phys. Rev. Lett.*, 83:4357–4360, 1999.

[78] O. Krauth, G. Fahsold, and A. Pucci. Asymmetric line shapes and surface enhanced infrared absorption of CO adsorbed on thin iron films on MgO(001). *J. Chem. Phys.*, 110:3113–3117, 1999.

[79] M.-C. Daniel and D. Astruc. Gold nanoparticles: Assembly, supramolecular chemistry, quantum-size-related properties, and applications toward biology, catalysis, and nanotechnology. *Chem. Rev.*, 104:293–346, 2004.

[80] Günter Schmid, editor. *Nanoparticles, From Theory to Application.* Wiley-VCH, Weinheim, Germany, 2004.

[81] J. Turkevitch, P. C. Stevenson, and J. Hillier. Nucleation and growth process in the synthesis of colloidal gold. *Discuss. Faraday Soc.*, 11:55–75, 1951.

[82] G. Frens. Controlled nucleation for the regulation of the particle size in monodisperse gold suspensions. *Nat. Phys. Sci*, 241:20–22, 1973.

[83] K. C. Grabar, R. Griffith Freeman, M. B. Hommer, and M. J. Natan. Preparation and characterization of Au colloid monolayers. *Anal. Chem.*, 67:735–743, 1995.

[84] E. S. Kooij, H. Wormeester, E. A. Brouwer, E. van Vroonhoven, A. van Silfhout, and B. Poelsema. Optical charaterization of thin colloidal gold films by spectroscopic ellipsometry. *Langmuir*, 18:4401–4413, 2002.

[85] T. Sato, D. Brown, and F. G. Johnson. Nucleation and growth of nano-gold colloidal lattices. *Chem. Commun.*, pages 1007–1008, March 1997.

[86] K. R. Brown and M. J. Natan. Hydroxylamine seeding of colloidal Au nanoparticles in solution and on surfaces. *Langmuir*, 14:726–728, 1998.

[87] K. R. Brown, D. G. Walter, and M. J. Natan. Seeding of colloidal Au nanoparticle solutions. 2. Improved control of particle size and shape. *Chem. Mater.*, 12:306–313, 2000.

[88] K. R. Brown, L. A. Lyon, A. P. Fox, B. D. Reiss, and M. J. Natan. Hydroxylamine seeding of colloidal Au nanoparticles. 3. Controlled formation of conductive Au films. *Chem. Mater.*, 12:314–323, 2000.

[89] S. Meltzer, R. Resch, B. E. Koel, M. E. Thompson, A. M. Madhukar, A. A. G. Requicha, and P. Will. Fabrication of nanostructures by hydroxylamine seeding of gold nanoparticles templates. *Langmuir*, 17:1713–1718, 2001.

[90] R. A. MacPhail, H. L. Strauss, and R. G. Snyder. C-H stretching modes and the structure of *n*-alkyl chains. 2. long, all-trans chains. *J. Phys. Chem.*, 88:334–341, 1984.

[91] F. Schreiber. Structure and growth of self-assembling monolayers. *Progress in Surf. Sci.*, 65:151–257, 2000.

[92] A. Ulman. Formation and structure of self-assembled monolayers. *Chem. Rev.*, 96:1533–1554, 1996.

[93] O. Dannenberger, M. Buck, and M. Grunze. Self assembly of *n*-alkanethiols: A kinetic study by second harmonic generation. *J. Phys. Chem.*, 103:2202–2213, 1999.

[94] D. Lin-Vien, N. B. Colthup, W. G. Fateley, and J. G. Grasselli. *The Handbook of Infrared and Raman Frequencies of Organic Molecules.* Academic Press, Inc., San Diego, USA, 1991.

[95] C. S.-C. Yang, L. J. Richter, J. C. Stephenson, and K. A. Briggman. In situ, vibrationally resonant sum frequency spectroscopy study of the self-assembly of dioctadecyl disulfide on gold. *Langmuir*, 18:7549–7556, 2002.

[96] M. Clark. Antibody engineering IgG effector mechanisms. *Chem. Immun.*, 65:88–110, 1997.

[97] S. Rupp. Hochempfindliche Oberflächenwellen-Sensoren für die Medizinische Diagnostik. Thesis, University of Heidelberg, 2004.

[98] J. M. Berg, J. L. Tymoczko, and L. Stryer. *Biochemistry.* Freeman, New York, 5^{th} edition, 2002.

[99] J. Twardowski and P. Anzenbacher. *Raman and IR Spectroscopy in Biology and Biochemistry.* Polish Scientific Publishers PWN Ltd, Warshaw, Poland, 1994.

[100] S. Dong, G. Luo, J. Feng, Q. Li, and H. Gao. Immunoassay of staphylococcal enterotoxin C1 by FTIR spectroscopy and electrochemical gold electrode. *Electroanalysis*, 13:30–33, 2001.

[101] http://www2.biology.ualberta.ca/courses.hp/bio107.hp/harrington/dna.jpg. Department of Biological Science, University of Alberta, Canada.

[102] http://www.aist.go.jp/RIODB/SDBS. Spectral database for organic compounds of the National Institute of Advanced Industrial Science and Technology (AIST), Japan.

[103] H. H. Mantsch and D. Chapman, editors. *Infrared Spectroscopy of Biomolecules*. Wiley-Liss, Inc., New York, USA, 1996.

[104] H.-U. Gremlich and B. Yan, editors. *Infrared and Raman Spectroscopy of Biological Materials*. Marcel Dekker, Inc., New York, USA, 2001.

[105] M. Banyay, M. Sarkar, and A. Gräslund. A library of IR bands of nucleic acids in solution. *Biophys. Chem.*, 104:477–488, 2003.

[106] I. Langmuir. The adsorption of gases on plane surfaces of glass, mica and platinum. *J. Am. Chem. Soc*, 40:1361–1403, 1918.

[107] K. A. Peterlinz and R. Georgiadis. In situ kinetics of self-assembly by surface plasmon resonance spectroscopy. *Langmuir*, 12:4731–4740, 1996.

[108] J. R. Rahn and R. B. Hallock. Antibody binding to antigen-coated substrates studied with surface plasmon oscillations. *Langmuir*, 11:650–654, 1995.

[109] S. Brunauer, P. H. Emmett, and E. Teller. Adsorption of gases in multimolecular layers. *Am. Chem. Soc.*, 60:309–319, 1938.

[110] W. G. McMillan and E. Teller. The assumptions of the B. E. T. theory. *J. Phys. Colloid Chem.*, 55:17–20, 1951.

[111] Opus 3.1. Software for spectroscopy, Bruker Analytische Messtechnik GmbH.

[112] A. Priebe. Untersuchung der oberflächenverstärkten Infrarotabsorption am System Kohlenmonoxid auf dünnen Eisenfilmen in Reflektions- und Transmissionsgeometrie. Diploma thesis, University of Heidelberg, 2000.

[113] Omnic 6.0a. Software for spectroscopy, Thermo Nicolet Corporation.

[114] Ocean Optics Inc., Dunedin, Florida, USA. *USB 2000 Fiber Optic Spectrometer Operating Instructions*.

[115] D. Sarid. *Scanning Force Microscopy*. Oxford University Press, New York, USA, 1991.

[116] R. Wiesendanger and H.-J. Güntherodt, editors. *Scanning Tunneling Microscopy II*. Springer-Verlag, Berlin, Germany, 1992.

[117] S. L. Flegler, J. W. Heckmann Jr., and K. L. Klomparens. *Scanning and Transmission Electron Microscopy, An Introduction*. W. H. Freeman and Company, New York, USA, 1993.

[118] Nanoscope 6.10b17. SPM software, Digital Instruments/Veeco.

[119] D. Enders, T. Nagao, A. Pucci, and T. Nakayama. Reversible adsorption of Au nanoparticles on SiO_2/Si - An in-situ ATR-IR study. (Submitted to Surf. Sci. Lett.).

[120] T. Hasegawa, J. Nishijo, and T. Imae. Structural study of boundary water molecules at a solid/water interface by a chemometric technique. *Anal. Sci.*, 17:i479–i482, 2001.

[121] K. G. R. Pacheler, F. Matlok, and H.-U. Gremlich. *Merck FT-IR Atlas, Eine Sammlung von FT-IR Spektren / A Collection of FT-IR Spectra*. VCH Verlagsgesellschaft mbH, Weinheim, Germany, 1988.

[122] K. Hinrichs. Reflection absorption IR spectroscopy (RAIRS). In H. Bubert and H. Jenett, editors, *Surface and Thin Film Analysis*. Wiley-VCH, Weinheim, Germany, 2002.

[123] D. Enders. Unpublished results.

[124] P. A. Brooksby and W. R. Fawcett. Infrared (ATR) study of hydrogen bonding in solutions containing water and ethylene carbonate. *J. Phys. Chem. A*, 104:8307–8314, 2000.

[125] Y. Shen and P. Wu. Two-dimensional ATR-FTIR spectroscopic investigation on water diffusion in polypropylene film: Water bending vibration. *J. Phys. Chem. B*, 107:4224–4226, 2003.

List of Figures

Index

Acknowledgment

I would like to thank everyone who contributed to the succeeding of this thesis.

Special thanks go to

Prof. Dr. Annemarie Pucci for the possibility to work in this interesting field and for being a great supervisor of my work,

Prof. Dr. Reinhard Neumann for his willingness to be the second referee,

Dr. Tomonobu Nakayama for kindly welcoming me in his work group at NIMS, Tsukuba and for interesting discussions,

Dr. Tadaaki Nagao for the fruitful collaboration, many interesting discussions, and for helping me get along in Tsukuba's everyday life,

Prof. Dr. Michael Grunze for the use of the SEM,

all current and former members of the work group Pucci for being great colleagues inside and outside the institute,

all members of the Electro-Nanocharacterization group at NIMS for being great colleagues and kindly helping me with all the little things in Tsukuba's everyday life,

Dr. Swen Rupp for helping me with the antibody immobilization,

Alex Küller for introducing me to the use of the SEM.

Finally, I would like to thank my parents for supporting me in various ways during my thesis and during my complete studies of Physics.

Special thanks go to Daniela.